universität wien

DISSERTATION

Titel der Dissertation

Photoacoustic Inversion Based on In-depth Wave Models

Verfasser

Thomas Glatz

angestrebter akademischer Grad

Doktor der Naturwissenschaften (Dr. rer. nat.)

Wien, Jänner 2016

Studienkennzahl lt. Studienblatt:	A 796 605 405
Dissertationsgebiet lt. Studienblatt:	Mathematik, IK: Computational Sciences
Betreuer:	Univ.-Prof. Dr. Otmar Scherzer

Abstract

Photoacoustic tomography (PAT) is an emerging coupled physics imaging modality. Its potential applications embrace clinical and pre-clinical diagnosis, as well as non-destructive testing in industrial processes. In PAT, a laser-light induced ultrasonic wave that encodes parameters of physiological interest, is measured outside the object. The photoacoustic problem consists of reconstructing these parameters from the measurements. This thesis is concerned with photoacoustic reconstruction in situations where the standard analytical methods either don't apply at all, or their discretization step needs careful attention.

In cases of one or even two varying acoustic parameters, the standard reconstruction procedure is time reversal. It consists in solving a time-reversed wave equation on a bounded domain, usually assuming vanishing final values, which leads to an approximation error. The measurements serve as Dirichlet boundary data. In contrast, in this work the photoacoustic problem is formulated as an operator equation. A Landweber iteration allows to stably reconstruct a regularized solution. Different to time reversal, this gives convergence to such a regularized solution also in cases where photoacoustic inversion is ill-posed, like in the presence of noise or when the underlying speed of sound is *trapping*. The back-propagation, that can in some sense be found in all treated reconstruction techniques, is now encoded in the adjoint operator. Its application requires to solve a transmission problem in the whole space backwards in time. In this sense, the Landweber approach shares remarkable similarities with time reversal.

A second aim is to enhance the quality of the reconstructed image by a non-equidistant arrangement of the detection sensors. On a planar domain and for constant speed of sound, there exists an exact frequency domain reconstruction formula. The key to a feasible realization of this formula lies in the efficient evaluation of the data's Fourier transform at non-equispaced points in temporal frequency domain. The non-uniform fast Fourier transform is well-suited for this problem from a theoretical point of view, since it is able to cope with non-equispaced detectors as well as with non-equispaced evaluation points. In practice, it outperforms the commonly used polynomial interpolation with respect to image quality and computational cost in experimental and synthetic data experiments.

A concluding example treats Photoacoustics as imaging modality in elastographic imaging. A sequence of photoacoustic images displays the mechanical deformation of the features of interest in a simulated elastographic experiment. In a first step, elastographic imaging consists in computation of the resulting displacement vector field. Photoacoustic imaging is considered to be not ideally suited for elastography, since its high-contrast images often contain large homogeneous areas, lacking speckle patterns which naturally occur in ultrasound imaging. In contrast to the standard approach, we consider the use of band-limited data, which we prove to encode certain additional texture. We show that this band-limitation serves as regularization within the reconstruction procedure. We also show experimentally that for the hereby obtained speckle-prone images, the deformation can be more reliably estimated.

Preface

This cumulative thesis collects the topic-related articles the author worked on within his PhD studies at the Faculty of Mathematics, University of Vienna. They have been written within the last two years.

The first part gives an introduction to the field of Photoacoustic imaging, including a short summary of some mathematical methods that come to application in this work. Moreover, it aims to give an overview about the main contributions included in the thesis.

The second part is divided into four Chapters, each of which contains an original (but layout-adapted) manuscript either published in or submitted to peer reviewed journals. Important meta-information such as the publication status of each article can be found at the end of the introduction.

In the appendix, a German version of the thesis' abstract can be found, as well as a CV including the author's most important publications and conference talks.

At this point, I want to thank my advisor Otmar Scherzer for introducing me to the field and for his support in good as in hard times. Thanks go as well to our co-worker and friend Zakaria Belhachmi, who gave me a warm welcome in Mulhouse and was always open to questions. Thanks to all reviewers, referees, and editors who took the time to read my work and provided valuable hints and remarks on the included manuscripts. A big thank you to Min Hadler, our secretary, who is the emotional foundation of the Computational Science Center. I want to thank my colleagues for making the CSC the warm and welcoming place it is. Thanks to the University of Vienna and the Faculty of Mathematics that provided a comfortable working environment throughout the years. Moreover, I want to thank my parents Sylvia and Dietmar, for the unconditional support for more than 30 years. Thanks to my brother Markus, and also to my dear partner in life Simone, who always believed in me when I didn't. I want to thank all of my friends and family that I could not mention in person here. Last but not least, I want to thank our La Pavoni espresso machine, that is in fact responsible for most of the valuable output I created in the last years.

Funding:
The work presented here was supported by the Austrian Science Fund (FWF) through the National Research Network 'Photoacoustic Imaging in Biology and Medicine' (NFN S107).

Contents

Part I

Preamble

1

Preliminaries

This chapter provides background information to the treated topics, with the aim to first contextualize and then give an outlook to the scientific contributions presented in the subsequent chapters.

1.1 Photoacoustic Tomography - The Photoacoustic Wave Equation

Photoacoustic tomography (PAT), also referred to as photoacoustic imaging (PAI), optoacoustic tomography (OAT) or thermoacoustic tomography (TAT), is a developing technique for tomographical imaging with potential applications in clinical or pre-clinical diagnosis. The main mechanism behind PAI lies in employing the photoacoustic effect. An object of interest is irradiated by a short pulse of electromagnetic energy (e.g. laser light of near infrared wavelength). Depending on the material properties, some of this energy is absorbed and converted into heat. This causes a thermoelastic expansion, leading to a pressure rise that spreads as ultrasonic signal. The intial acoustic pressure is assumed to be proportional to the absorbed electromagnetic energy. The prior serves as imaging parameter of Photoacoustics, providing anatomical and functional information of high resolution and high contrast. A schematic description of a photoacoustic experiment is given in Figure 1.1.

The mathematical model describing the propagation of the ultrasonic pressure y considered in this thesis is

$$\begin{aligned} \kappa(x)y''(x,t) - \nabla \cdot \Big(\rho(x)^{-1}\nabla y(x,t)\Big) &= 0 \text{ in } \mathbb{R}^n \times (0,\infty) \\ y(x,0) &= f(x) \text{ in } \mathbb{R}^n \\ y'(x,0) &= 0 \text{ in } \mathbb{R}^n. \end{aligned} \tag{1.1.1}$$

Note that here and below, y' and y'' denote the first, resp. second derivative w.r.t. t. Note that κ denotes the material compressibility, while ρ labels the density. The initial pressure $f(x)$ is related to the underlying physical properties and the amount of illumination by

$$f(x) = \frac{\beta(x)I(x)\mu(x)}{C_p(x)}, \tag{1.1.2}$$

where $\beta(x)$ is the thermal expansion coefficient, the parameters $C_p(x)$, resp. $\mu(x)$, are the specific heat capacity, resp. the absorption coefficient, and $I(x)$ is the absorbed electromagnetic energy.

This means that f is a suitable imaging parameter that encodes the material properties of physiological interest in PAI. To derive Equation (1.1.1), the Euler and continuity equations from fluid dynamics are linearized around an equilibrium state. Moreover, the

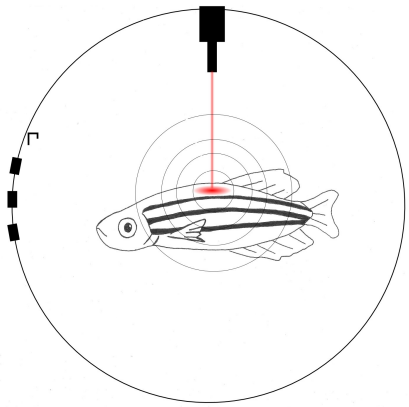

FIGURE 1.1: Schematic image of a photoacoustic experiment.

linearized volume expansion equation from thermodynamics is employed, which describes the relation between the rate of change of volume to the change of pressure and deposited energy over time. By assuming that the electromagnetic excitation is infinitesimally short, the photoacoustic wave equation can be written as the initial value problem (1.1.1) [CK92; Sch+09].

The quantity $c(x) = \frac{1}{\sqrt{\kappa(x)\rho(x)}}$ is called speed of sound. In the case when ρ is spatially slowly varying, the approximation

$$\nabla \cdot \rho^{-1} \nabla y \approx \rho^{-1} \Delta y$$

is reasonable. The photoacoustic wave equation turns into

$$\begin{aligned} y''(x,t) - c^2(x)\Delta y(x,t) &= 0 \text{ in } \mathbb{R}^n \times (0,\infty) \\ y(x,0) &= f(x) \text{ in } \mathbb{R}^n \\ y'(x,0) &= 0 \text{ in } \mathbb{R}^n, \end{aligned} \tag{1.1.3}$$

which also describes acoustic wave propagation in the case of variable sound speed.

1.2 Reconstruction in Photoacoustic Tomography

The Photoacoustic measurements are taken on a surface Γ over a finite time interval $(0,T)$, i.e. on $\Sigma = \Gamma \times (0,T)$. The problem therefore consists in solving the equation

$$Lf = m, \tag{1.2.1}$$

where L is a linear operator (the *photoacoustic operator* mapping the initial data f to (possibly deteriorated) measurements m of $y|_\Sigma$. For instance, the measured data could be band-limited, i.e. $m = \varphi_\varepsilon *_t y(t)|_\Sigma$, with $\varphi_\varepsilon : \mathbb{R} \to \mathbb{R}$ denoting the impulse-response of the used detector. The binary operation $*_t$ is the convolution w.r.t. the time variable. Photoacoustic reconstruction from band-limited data is treated in Chapter 6. In the present section we assume, as usual in literature, *ideal* measurements $m = y|_\Sigma$.

1.2.1 Constant Speed of Sound

Assuming constant speed of sound, ideal measurements and special shapes of measurement surfaces, analytical reconstruction formulas for Photoacoustics have been developed [XXW02; XW02; XFW02; XXW03; XW05; FPR04; FHR07; Kun07; KK11; Kuc14]. Basically, one can distinguish between formulas of filtered backprojection (FBP) type and formulas that employ eigenfunction expansions (with the type of basis functions depending on the shape of the measurement geometry). For a review on the most common reconstruction techniques, we refer to [KK08]. The aim of this subsection is to summarize the formulas and approaches used within the subsequent chapters of the present thesis.

Assume for simplicity that f is smooth and compactly supported, even though, depending on n, less smoothness requirements are required for the existence of a classical solution, resp. the reconstruction formulas to hold. Assume also infinite measurement time $T = \infty$.

The solution to the Wave Equation in Terms of Spherical Means

For constant κ and ρ (without loss of generality, assume $\kappa\rho = 1$), (1.1.1) reduces to

$$\begin{aligned} y'' - \Delta y &= 0 \quad \text{in } \mathbb{R}^n \times (0,\infty), \\ y(x,0) &= f(x) \quad \text{in } \mathbb{R}^n, \\ y'(x,0) &= 0 \quad \text{in } \mathbb{R}^n . \end{aligned} \tag{1.2.2}$$

There exist well-known explicit solutions for (1.2.2) in terms of spherical integrals (see [Eva10] for a detailed introduction).

Let's introduce the spherical mean operator in n dimensions, namely

$$\mathcal{M}_n[f](x,r) = \frac{1}{|S^{n-1}|} \int_{S^{n-1}} f(x + r\theta) ds(\theta) , \tag{1.2.3}$$

where $|S^{n-1}|$ denotes the area of the unit sphere in $\mathbb{R}^n$ and $ds(\theta)$ denotes the surface measure.

In the case $n = 2$, the solution to (1.2.2) is

$$y(x,t) = \frac{1}{2\pi} \partial_t \left(\int_0^t \frac{\tau}{\sqrt{t^2 - \tau^2}} \mathcal{M}_2[f](x,\tau) d\tau \right) . \tag{1.2.4}$$

The solution for $n = 3$ is given by

$$y(x,t) = \partial_t (t \mathcal{M}_3[f])(x,t) . \tag{1.2.5}$$

Note that for $n = 3$ (or any odd spatial dimensions), since f is compactly supported, y is zero after some finite time. This is not the case in two (even) dimensions.

A Frequency Domain Reconstruction for Measurements on a Planar Surface

Perhaps the most simply obtainable reconstruction formula is the one for measurements along a (hyper-)plane, as it just requires elementary knowledge of Fourier transforms and

ordinary differential equations. It goes back to Norton and Linzer [NL81], who derived an equivalent formula for ultrasound tomography with backscattering measurements.

Let $(\tilde{k}, k_n) \in \mathbb{R}^{n-1} \times \mathbb{R}^+$ (where we use the abbreviation $\tilde{k} := (k_1, \ldots, k_{n-1})$). Assume without loss of generality (by choice of a proper basis) that Γ is the hyperplane described by $x_n = 0$. Then the reconstruction formula is given by the identity

$$\mathcal{F}[f](k) = \frac{2k_n}{\kappa(k)} \mathcal{F}[Lf]\left(\tilde{k}, \kappa(k)\right). \tag{1.2.6}$$

Here, $\mathcal{F}$ denotes the n-dimensional Fourier transform,

$$\mathcal{F}[f](k) := \frac{1}{(2\pi)^{n/2}} \int_{\mathbf{R}^n} \mathrm{e}^{\mathrm{i}k\cdot x} f(x) dx\,,$$

and

$$\kappa(k) = \operatorname{sign}(k_n)\,|k|\,.$$

For applications in Photoacoustics see, e.g., [Kös+01; XFW02], where the formula is derived for the case of three spatial dimensions. We give a derivation for arbitrary $n \geq 2$ in Appendix A.

A Filtered Backprojection Reconstruction for Measurements on a Spherical Surface

Backprojection formulas have the advantage of giving an exact closed form expression for photoacoustic reconstruction. The name backprojection is also used for the inversion of the Radon transform [Nat86] and goes back to the original inversion formula of Radon [Rad17]. There, the backprojection consists of taking the means of the values corresponding to the straight lines intersecting in the same point. An exact reconstruction can be obtained by applying a so-called filtering prior to the backprojection step.

An analogous idea works for photoacoustic inversion, but in terms of the spherical mean transform and the according backprojection operation. Norton and Linzer [NL81] found an approximate inversion procedure for ultrasound tomography employing spherical backprojection in 3D. The exact formulas for Photoacoustics and spherical measurement geometry have been found in [FPR04] for odd n and [FHR07] for n even.

Assume throughout this paragraph that $\Gamma = \partial B_R(0)$, i.e. that the measurements are taken on a sphere with center point 0 and radius R. The spherical mean backprojection operator is defined as

$$\mathcal{B}_n[g](x) := \frac{1}{|S^{n-1}|} \int_{\partial B_R(0)} \frac{g(z, |z-x|)}{|z-x|^{n-1}} ds(z) \quad \text{for } x \in B_R(0)\,. \tag{1.2.7}$$

We further define

$$\mathcal{A}[g](t) := \frac{2t}{\sqrt{\pi}} \int_t^\infty \frac{g(\tau)}{\sqrt{\tau^2 - t^2}} d\tau \quad \text{for } t \in (0, \infty)\,. \tag{1.2.8}$$

In Figure 1.2, the measurement circle Γ, a point x in the domain and two circles intersecting in x with center point z_i on Γ are depicted. Each circle corresponds to a value $g(z_i, r_i)$, where $r_i = |z_i - x|$. Roughly speaking, the backprojection operator $\mathcal{B}_n$ maps to the weighted integral over all $g(z_i, r_i)$.

For any sufficiently smooth f with support within $B_R(0)$ the following identities provide exact reconstruction formulas for photoacoustic tomography [FPR04; FHR07; Hal11]:

$$f(x) = \begin{cases} \dfrac{\sqrt{\pi}}{R}\mathcal{B}_2\mathcal{A}[t\partial_t Lf](x) & \text{for } n = 2\,, \\ \dfrac{1}{R}\mathcal{B}_3[t\partial_t Lf](x) & \text{for } n = 3\,, \end{cases} \tag{1.2.9}$$

for all $x \in \mathbb{R}^n$. Note that the *filtering* step ahead of the backprojection is local in time for $n = 3$, but global for $n = 2$ (demanding for infinite measurement times). In practice, a decay criterion for (1.2.8) as $t \to \infty$ leads to an approximate solution for finite T.

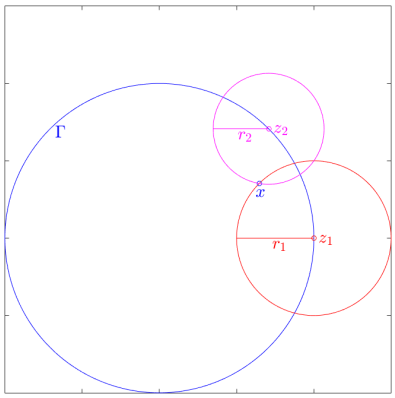

FIGURE 1.2: Backprojection of the data in y_1, y_2 to circles with center on Γ going through x.

1.2.2 Variable Speed of Sound

In the case of variable speed of sound, that is, varying κ and/or ρ in (1.1.1), the analytical methods from Subsection 1.2.1 do not apply anymore. A popular approach for numerical reconstruction in such a case is *time reversal*. Ideally, if one knew $y(\cdot, T)$, $y'(\cdot, T)$ in a domain $\Omega \subseteq \mathbb{R}^n$ that contains $\operatorname{supp} f$, with known Dirichlet trace $y|_\Sigma$ (where $\Sigma = \partial\Omega \times (0, T)$), the time reversal property of the wave equation would allow to solve the Dirichlet problem

$$\begin{aligned} \kappa(x)z''(x,t) - \nabla \cdot \rho^{-1}\nabla z(x,t) &= 0\,, \quad \text{in } \Omega \times (0,T) \\ z(x,T) = y(x,T),\ z'(x,T) &= y'(x,T)\,, \quad \text{in } \Omega \\ z(x,t) &= y(x,t) \quad \text{on } \Sigma\,. \end{aligned} \tag{1.2.10}$$

backwards in time, with $z(x,t) = y(x,t)$ in $\Omega \times (0,T)$. The problem is that $y(x,T)$ and $y'(x,T)$ are usually unknown in Ω. At first glance, substituting $z(x,T) = z'(x,T) = 0$ seems to be reasonable for large measurement times T, as the pressure wave seems to

spread over time, with the pressure energy decreasing within Ω. From formula (1.2.5) one can directly deduce that for T large enough, this assumption is fulfilled for constant speed and $n=3$, whereas for $n=2$ it is not. To obtain an approximate reconstruction of f by time reversal when the speed of sound is not constant, the latter has to fulfill a so called *non-trapping condition*. Roughly speaking, the non-trapping condition is fulfilled whenever all geodesics in the metric $\kappa\rho dx$ eventually leave Ω.

If $c(x)=(\kappa(x)\rho(x))^{-1/2}$ is *non-trapping*, then the pressure energy of y decays fast enough as $T\to\infty$ (with polynomial decay for n even, with exponential decay for n odd) to obtain an approximation for $y(\cdot,0)$.

Stefanov and Uhlmann [SU09] define a modified time reversal for (1.1.1): Rather than assuming $z(T)\equiv 0$, they use the harmonic extension of the data term $m(s,T)$, for $s\in\partial\Omega$, as initial datum at T. That is, for

$$-\nabla\cdot(\rho^{-1}\nabla\phi)=0 \text{ in } \Omega, \text{ with } \phi(\cdot)=m(\cdot,T) \text{ on } \partial\Omega,$$

the modified time reversal operator

$$\overline{L}[m]=z(\cdot,0) \tag{1.2.11}$$

is defined by the solution of equation

$$\begin{aligned} \kappa z''-\nabla\cdot(\rho^{-1}z)&=0 \text{ in } \Omega\times(0,T),\\ z(T)=\phi,\quad z'(T)&=0 \text{ in } \Omega,\\ z&=m \text{ on } \partial\Omega\times(0,T). \end{aligned} \tag{1.2.12}$$

In a quite general setting including the here presented wave models, they showed stability of their modified time reversal reconstruction under non-trapping conditions and for sufficiently large measurement time. In fact, assume that $c=(\kappa\rho)^{-1/2}$ is non-trapping. Then there is a time $T_1<\infty$ when all singularities have left $\overline{\Omega}$. We assume $T>T_1$. Moreover, assume κ,ρ are smooth in $\mathbb{R}^n$ and constant outside of Ω.

Under these assumptions and for measurements taken on all of $\partial\Omega\times(0,T)$, the reconstruction error (from unperturbed measurements) $K=I-\overline{L}L$ is shown to be a compact contraction.

From this, one can immediately deduce the convergence of the Neumann series

$$f=\sum_{j=0}^{\infty}K^j[m], \tag{1.2.13}$$

which provides the iterative reconstruction algorithm

$$f_k=f_{k-1}-\overline{L}[L[f_{k-1}]-m], \tag{1.2.14}$$

where

$$f_k=\sum_{j=0}^{k}K^j[m].$$

In the case of partial data [SU09] provide an injectivity result and an H^1 stability estimate, that also can be found in Chapter 4.

Note however, that the approach provides no theoretical tool in the presence of noise, trapping speed or insufficient measurement time. We discuss this in Chapter 2.

1.3 Hilbert Space Regularization of Ill-posed Inverse Problems

A convenient setting to formulate inverse problems is that of operator equations, formulated for operators between function spaces. Since convergence of Cauchy sequences is a desired property, these spaces are usually chosen to be Banach spaces. In this thesis, we focus on bounded linear operators between Hilbert spaces, which simplifies the theory and analysis. A comprehensive introduction to linear ill-posed problems in Hilbert spaces is given, e.g., in [EHN96].

Let

$$A : \mathcal{X} \to \mathcal{Y}$$

be a bounded linear operator. We are interested in the equation

$$Af = g\,, \tag{1.3.1}$$

where $f \in \mathcal{X}$ and $g \in \mathcal{Y}$. Here, we can distinguish between two different problems. The evaluation of Af is considered as forward or direct problem, while solving the equation for f with given data g is referred to as the inverse problem.

In order to categorize the latter problem, we first introduce Hadamard's definition for well-posedness, which, applied to (1.3.1), consists of three criteria:

1. (Existence): There exists a function x such that $Ax = g$; i.e. $g \in \operatorname{ran}(A)$.
2. (Uniqueness): A is injective, i.e. $\ker(A) = \{0\}$.
3. (Continuity): The inverse operator A^{-1} is bounded.

Here $\operatorname{ran}(A)$ denotes the range of A, while $\ker(A)$ denotes its null space. Direct problems are often stated the way that they are well-posed in the sense of Hadamard. The corresponding inverse problem however can still be ill-posed. In fact, for a wide class of operators (including compact operators with infinite-dimensional range), the inverse problem is generically ill-posed. To cope with the existence, a possible approach is to search for the *least-squares solution*

$$\arg\min_{\varphi \in \mathcal{X}} \|A\varphi - g\|_{\mathcal{Y}}^2$$

instead of searching for an exact solution to (1.3.1). It can be shown that such a minimizer exists whenever $g \in \operatorname{ran}(A) \oplus \operatorname{ran}(A)^{\perp}$. The classical way to enforce uniqueness is to search for the minimum norm solution

$$f^{\dagger} = \arg\min_{\varphi \in \mathcal{X}} \{\|\varphi\|_{\mathcal{X}} \,|\, \varphi \text{ is least-squares solution of } Af = g\}\,.$$

The *Moore-Penrose* generalized inverse $A^\dagger$, defined on $\mathcal{D}(A^\dagger) = \operatorname{ran}(A) \oplus \operatorname{ran}(A)^\perp$, assigns $g \mapsto f^\dagger$ for every $g \in \mathcal{D}(A^\dagger)$. Therefore, by searching for a regularized solution in this sense and restricting the admissible data to $\mathcal{D}(A^\dagger)$, the problem of existence and uniqueness of a solution to (1.3.1) can be addressed. However, if $\operatorname{ran}(A)$ is not closed, then $\mathcal{D}(A^\dagger) \subsetneq \mathcal{Y}$. Moreover, the Moore-Penrose inverse $A^\dagger$ is unbounded in this case. This is problematic whenever only error-prone data g^δ, with $\left\|g^\delta - g\right\|_{\mathcal{Y}} \leq \delta$ are given.

A remedy to this problem is provided by so-called regularization methods, that are briefly described in Subsection 1.3.1.

1.3.1 Regularization Methods

The aim is to describe a reconstruction technique that finds approximate solutions for $g \in \mathcal{A}^\dagger$ in a stable way. Roughly speaking, a family of continuous mappings $\{R_\alpha\}$, for $\alpha \in (0, \infty]$, is called regularization of $A^\dagger$ if for all $g \in A^\dagger$ a parameter choice rule of $\alpha(\delta, g^\delta)$ in dependence of the error can be found such that $\limsup_{\delta \to 0}\{\alpha(\delta, g^\delta)\} = 0$ and

$$\limsup_{\delta \to 0} \left\| R_{\alpha(\delta, g^\delta)} g^\delta - A^\dagger g \right\|_{\mathcal{X}} = 0 \,.$$

Note that the reconstruction error consists of an approximation error and a data error, i.e.

$$\left\| R_\alpha g^\delta - A^\dagger g \right\|_{\mathcal{X}} \leq \left\| R_\alpha g - A^\dagger g \right\|_{\mathcal{X}} + \left\| R_\alpha (g - g^\delta) \right\|_{\mathcal{X}} \,.$$

In the (typical) case where $\operatorname{ran}(A)$ is not closed (and therefore $A^\dagger$ is unbounded), there is no uniform bound for $\|R_\alpha\|$ for all $\alpha > 0$. Therefore, the parameter has to be chosen in a way that keeps the approximation error and the data error small.

Two standard Regularization methods, which will be employed in Chapter 3, Chapter 4 and Chapter 6, are described in the following paragraphs.

Tikhonov Regularization

Tikhonov regularization consists in searching for a solution to the equation

$$A^* A f_\alpha^\delta + \alpha f_\alpha^\delta = A^* g^\delta \,,$$

where A^* is the adjoint operator to A, that is

$$\langle Af, g \rangle = \langle f, A^* g \rangle \quad \forall f \in \mathcal{X},\, g \in \mathcal{Y} \,.$$

An equivalent formulation is given in terms of a variational characterization, by searching for a minimizer

$$f_\alpha^\delta = \operatorname*{arg\,min}_{f \in \mathcal{X}} \left\| Af - g^\delta \right\|_{\mathcal{X}}^2 + \alpha \|f\|_{\mathcal{Y}}^2 \,. \tag{1.3.2}$$

The first term on the r.h.s. is called data term, the second term is called penalty or regularization term. Its influence is controlled via the regularization parameter α. For a suitable parameter choice rule, the solution to (1.3.2) converges to the minimum norm solution $A^\dagger g$ as $\delta \to 0$.

Landweber Regularization

Let A be as above, satisfying $\omega \|A\|^2 \leq 1$ for some $\omega > 0$.

The Landweber iteration [EHN96] is defined as follows:

$$f_0 := 0 \quad \text{and} \quad f_k^\delta = f_{k-1}^\delta - \omega A^*[A[f_{k-1}^\delta] - g^\delta], \quad k = 1, 2, \dots . \tag{1.3.3}$$

Whenever $\delta = 0$, means if $g^\delta = g$, then we write $f_k = f_k^\delta$.

Let $\tau > 1$ be some fixed constant. The Landweber iteration with stopping criterion is only repeated as long as

$$\left\| g^\delta - A[f_k^\delta] \right\|_{\mathcal{Y}} > \tau\delta \, . \tag{1.3.4}$$

The index where (1.3.4) is violated for the first time is denoted by $k_*(\delta, g^\delta)$. In regularization theory, this stopping rule is called discrepancy principle. Indeed, the stopping criterion serves as regularization. Employing the stopping criterion, Landweber iteration converges to the best-approximating solution $f^\dagger$ in the following sense: Let $g \in \operatorname{ran}(A)$.

- Let $\delta = 0$, then the Landweber iterates (f_k) converge to $f^\dagger$, i.e., $\left\| f_k - f^\dagger \right\|_{\mathcal{X}} \to 0$. In addition, we have the series expansion

$$f^\dagger = \sum_{j=0}^{\infty} (I - \omega A^* A)^j [A^*[g]] \, .$$

- For $\delta > 0$ and g^δ satisfying $\left\| g - g^\delta \right\|_{\mathcal{Y}} \leq \delta$ let $k_*^\delta = k_*(\delta, g^\delta) - 1$. Then

$$f_{k_*^\delta}^\delta \to_{\mathcal{X}} f^\dagger \, .$$

Note that if $g^\delta \notin \mathcal{D}(A^\dagger)$, then $\left\| f_k^\delta \right\|_{\mathcal{X}} \to \infty$ as $k \to \infty$. This means that the stopping criterion is necessary in general, if $\operatorname{ran}(A)$ is not closed and therefore $\mathcal{D}(A^\dagger) \subsetneq \mathcal{Y}$.

2

Contributions of the Thesis

This thesis is organized in a cumulative way, containing manuscripts and publications written in the last two years. The aim of this chapter is to introduce the most important ideas, concepts, and contributions of the thesis. The unifying quality of all approaches is the extension, in some sense, of commonly used photoacoustic models. An important part in most of the manuscripts is the use of regularization techniques for photoacoustic, resp. elastographic reconstruction. Although widely used for inverse problems, regularization methods have been living a niche existence (but with some considerable contributions worth mentioning, as e.g. [HLR09; Hal11; DGK14] for regularization of the spherical mean oparator, valuable in the case of constant sound speed), due to the well-posed nature of the original problem. However, in the case of error-prone data or short measurement times, the photoacoustic problem turns out to be ill-posed. In this cases, regularization techniques provide a remedy to ensure stable reconstruction. The regularizing approach presented in Chapter 3 handles inhomogeneous speed of sound, Chapter 4 treats the more general case of two varying acoustic parameters, noisy measurements and partially available data.

In contrast to PAT, regularization techniques are unavoidable and therefore omnipresent in computer vision, more specifically in the computation of the optical flow of an image, as it is used in elastographic imaging. In addition to the instability of the inverse problem, an obvious challenge in optical flow computations is its non-uniqueness. It is unclear why the minimum-norm solution, enforcing uniqueness in reconstruction, should be more suitable than any other choice. The approach chosen in Chapter 6 is to alter the data term by a convolution in space, and to leave the original (Tikhonov) regularization term of Horn and Schunck [HS81] unchanged. The resulting modeling error is shown to act as regularization method as well. The chosen convolution kernel appears in reconstruction with band-limited measurements, is highly oscillating and therefore adding texture, particularly in the problematic homogeneous areas of the image.

2.1 Landweber Regularization as Alternative to Time Reversal

In Chapter 3 and Chapter 4 we analyze the linear *wave operator* L mapping the initial pressure f onto the solution y of (1.1.1) restricted to Σ. That is

$$L : H_0^1(\Omega) \to L^2(\Sigma), \quad f \mapsto y|_\Sigma . \tag{2.1.1}$$

We show that L is bounded, with $\|L\|$ only depending on the measurement geometry Γ and the measurement time T. Moreover, we explain in Chapter 4 why L is in fact compact, which makes its inversion ill-posed.

For reconstruction, we choose Landweber iteration due to its similarities to the well-known time reversal algorithms. Especially the iterative approach introduced in [SU09] is of surprisingly similar structure.

The adjoint operator L^* is characterized by a time-reversed transmission problem for the wave equation in the whole domain. In fact,

$$L^*[h] = i^* \circ L_D^*[h],$$

where i^* is a lifting operator depending on the choice of the underlying norm, and

$$L_D^*[h] = \kappa z'(0)\big|_\Omega,$$

with $z := z(h)$ the weak solution of

$$\begin{aligned} \kappa z'' - \nabla \cdot (\rho^{-1} \nabla z) &= 0 \text{ in } \mathbb{R}^n \backslash \partial\Omega \times (0,T), \\ z(T) = z'(T) &= 0 \text{ in } \mathbb{R}^n, \\ [z] = 0, \quad \left[\frac{\partial z}{\partial n}\right] &= h \text{ on } \Sigma, \\ [z] = 0, \quad \left[\frac{\partial z}{\partial n}\right] &= 0 \text{ on } \partial\Omega \setminus \Sigma \times (0,T). \end{aligned} \tag{2.1.2}$$

Note that

$$[z] := z^+|_\Sigma - z^-|_\Sigma \text{ and } \left[\frac{\partial z}{\partial n}\right] := \left.\frac{\partial z^+}{\partial n}\right|_\Sigma - \left.\frac{\partial z^-}{\partial n}\right|_\Sigma.$$

The functions z^+ and z^- denote the traces of z in the exterior, resp. the interior domain on $\partial\Omega \times (0,T)$.

The Landweber iteration (1.3.3), applied to Photoacoustics, provides a stable reconstruction scheme that converges, whenever L is injective, in norm to the true solution f. The sufficient measurement time to obtain injectivity depends on the measurement surface Γ and the metric induced by $\kappa\rho$.

Note Table 2.1 (that can also be found in Chapter 4) for the differences in the obtained results between time reversal methods and the Landweber regularizing approach.

	Time Reversal	**Neumann**	**Landweber**
Convergence:			best approx. sol.
measurement time	$T \to \infty$	$T > T_1$	$T > 0$
sound speed	non-trapping	non-trapping	arbitrary
data	full	full	partial
Stability:			regularized sol.
measurement time	$T > T_1$	$T > T_1/2$	$T > 0$
sound speed	non-trapping	non-trapping	arbitrary
data	full	partial	partial
L^2**-Noise:**	no	no	yes

TABLE 2.1: Overview on the different photoacoustic imaging methods.

2.2 Influence of a Modeling Error in Case of Two Varying Parameters

As the gradient of ρ^{-1} gets large, so does the error in the approximation

$$\nabla \cdot (\rho^{-1} \nabla y) \approx \rho^{-1} \Delta y \,.$$

The aim of using the model (1.1.1) instead of (1.1.3) is to draw attention to the artifacts that potentially occur in photoacoustic reconstruction caused by this modeling error, for instance in presence of bone or air inclusions within otherwise relatively sound-homogeneous soft tissue. Table 2.2 provides an overview on common materials and their acoustic properties (that can be found, e.g., in [HBH04; SCC07]).

	Density (kg/m^3)	**Compress.** (Pa^{-1})	**Sound speed** (m/s)
Water	1000	$4.44 \cdot 10^{-10}$	1500
Air	1.2	$7.08 \cdot 10^{-6}$	343
Fat tissue	900	$5.28 \cdot 10^{-10}$	1450
Muscle tissue	1060	$3.78 \cdot 10^{-10}$	1580
Blood	1060	$3.82 \cdot 10^{-10}$	1570
Bone	1750	$3.43 \cdot 10^{-11}$	4080

TABLE 2.2: Overview on approximate values of density, compressibility and speed of sound of some materials involved in medical imaging.

One example in Chapter 4 treats the case of a density map that contains a high-gradient region. The used phantom is inspired by the air-filled swim bladder of a fish.

2.3 Non-equispaced Detector Placement to Enhance Image Quality

In practical pre-clinical experiments, a specific measurement setup, where an interrogation laser scans a thin polymer layer for acoustic detection, has proven to provide excellent data with respect to the achievable resolution through its high *impulse response*, small *measurement element size* and *detector sensitivity* [Jat+15]. The scanned polymer is hereby best approximated by a plane, the detection points can in principle be chosen arbitrarily on the surface, by moving the interrogation laser to the desired position.

The current setups allow data acquisition at just one single sensor point for each laser pulse excitation. Since the used excitation laser is operating at 50 Hz, data recording of a typical sample requires several minutes, depending on the desired resolution.

In the aim of employing formula (1.2.6) we therefore face the following challenges:

1. Find an appropriate and fast way for computation of the involved Fourier transforms at non-equispaced points (this challenge arises directly from formula (1.2.6)).

2. Discretize with as little detection points as possible, allowing non-equispaced positioning.

3. Find a suitable implementation for the non-equispaced detector placement.

In order to treat these challenges, we use the NEDNER-NUFFT, which is new to photoacoustic imaging, within the numerical implementation of (1.2.6). Standard FFT algorithms compute Fourier modes on equispaced grid points from equispaced data. The NEDNER-NUFFT uses Fourier interpolation techniques to be able to efficiently (with complexity of the same order as the FFT) evaluate Fourier transforms on non-equispaced points, from non-equispaced data. It is therefore well-suited for dealing with non-equispaced sensor positioning, as error analyses for the NED- and the NER-NUFFT indicate [Fou03]. The underlying mathematics is elementary, but with a lot of notational snares. An introduction is given in Chapter 5, Section 5.3. The gained flexibility in the positioning of the detection points is used to enhance the image quality with a fixed number of detection points.

A specific problem that we are facing when trying to optimize the detection grid is the limited view problem. Assume that the measurements are taken within a detection region as depicted in Figure 2.1. According to [Xu+04], the detection region is the area which is enclosed by the normal lines from the edges of the sensor. The reconstruction is locally stable if the straight line through the normal to the object boundary passes through the detector surface [LQ00]. Therefore certain edges are invisible to the detector. In our approach, we try to overcome this problem by finding the optimal balance between detection width and resolution, by keeping the number of detection points fixed.

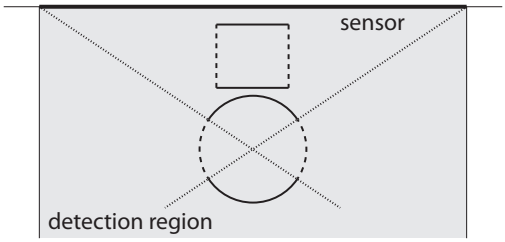

FIGURE 2.1: Depiction of the limited view problem.

2.3.1 Equi-angular and Equi-steradian Projections

Our choice for the detector placement shall be dense in the neighborhood of the center of interest and become sparser the further away the sampling points are located. This is realized by an equi-angular (2D), resp. equi-steradian (3D) sensor arrangement, where for a given point of interest each unit angle or steradian gets assigned one sensor point.

These are in detail explained in Section 5.6. To give a rough idea, Figure 2.2 shows a particular choice of equi-staradian and equidistant detector placements.

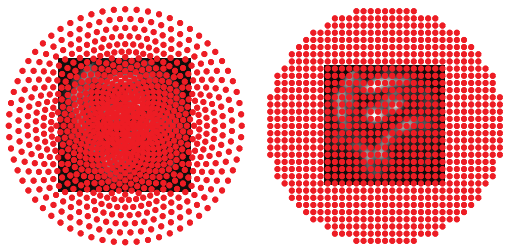

FIGURE 2.2: Equi-steradian (left) vs. equidistant (right) detector placement. The number of detectors is approximately 900 in each setup.

2.4 Application of Photoacoustics with Band-limited Data for Elastographic Imaging

Elastography is an imaging modality that aims to visualize elastic material properties. The parameters of interest encode valuable clinical information. Among its current applications are early detection of skin, breast and prostate cancer, detection of liver cirrhosis, and characterization of artherosclerotic plaque in vascular imaging (see for instance [Doy12; PDR11; Wej+10; Aig+11; Wan+09; Woo+06; Bis+10]).

Elastography, as *on top imaging method*, relies on an underlying imaging technique. Usual methods providing images for elastography include ultrasound imaging (see for instance [Ler+88; Oph+91]), magnetic resonance imaging (see for instance [Mut+95; Man+01]), or optical coherence tomography (see for instance [SSY11; Nah+13]). Using such an underlying technique, a series of images visualizing the image movements, is computed. From this *video*, the mechanical displacements can be calculated. They form the basis of clinical examinations and provide a basis for reconstruction of the underlying material properties.

Opposed to ultrasound imaging, photoacoustic imaging is considered to reveal little speckle patterns [LW06]. This is usually praised as a big advantage of Photoacoustics, since it has the potential to provide sharp high-contrast images. In elastography, however, the characteristic speckle patterns serve as valuable information in the aim to find the displacement vector field (called speckle tracking). These paradigms might be one reason why active coupling of Photoacoustics and elastography has not been reported so far.

In Chapter 6, we provide a mathematically founded way of introducing speckle in photoacoustic imaging data by filtering the photoacoustic signal. A common assumption in Photoacoustics is that the pressure signal is very broadband, due to the (relative to the wave speed) instantaneous pressure rise. Mathematically a Fourier transform w.r.t. time of a solution of the wave equation shows that the so-received function fulfills the Helmholtz equation for all frequencies. Common ultrasound imaging, on the contrary, is operating with a fixed single frequency mode. This superficial comparison motivates us to investigate, using [Hal11; HSZ09b], how much effect band-limited measurements have on the imaging process. We show mathematically that frequency-filtered, band-limited data are in the range of the photoacoustic operator. That is, there exists an (under the usual assumptions unique) initial pressure function that solves the photoacoustic equation for the altered data. We can therefore apply the usual reconstruction formula to obtain an image containing speckle-like patterns. These images, serving as elastographic data, can

be used to support tracking and optical flow techniques for displacement estimations. For detection of the displacement vector field from photoacoustic images, we use *optical flow* methods. The main underlying assumption for optical flow computations is the conservation of intensities in the images along the trajectories $x(t)$, that is,

$$f(x(t),t) = C$$

for a real constant C, which is reasonable for sufficiently incompressible tissue. By linearization with respect to time, one obtains

$$\nabla f \cdot u + f_t = 0, \tag{2.4.1}$$

where $u = \dot{x}(t)$ is the displacment vector field. Equation (2.4.1) is often referred to as *optical flow constraint*. Note that opposed to (1.1.1), the term $f(x,t)$ now stands for a (continuous) sequence of photoacoustic images. For quasi-static elastography with normalized time stepping, it reduces to

$$\nabla f_0 \cdot u + f_1 - f_0 = 0, \tag{2.4.2}$$

Here, the functions f_1 and f_0 are photoacoustic reconstructions from two different data sets, obtained from two subsequent experiments. It can be easily seen that the problem of finding u from given f is underdetermined. A very famous approach of Horn and Schunck [HS81] for enforcing uniqueness consists in searching for the minimum norm solution with respect to the H^1 (semi)norm

$$|u|^2_{H^1(\Omega)} = \int_\Omega |\nabla u(x)|^2 dx\,. \tag{2.4.3}$$

In fact, the approach consists in finding a minimizer

$$u^\dagger = \operatorname*{arg\,min}_{u \in H^1(\Omega)} \|\nabla f_0 \cdot u + f_1 - f_0\|^2_{L^2(\Omega)} + \alpha |u|^2_{H^1(\Omega)}\,, \tag{2.4.4}$$

where α is a regularization parameter. This formulation can, assuming sufficient smoothness and boundary conditions for u that guarantee that $|\cdot|_{H^1}$ is indeed a norm, be regarded as Tikhonov regularization and therefore obtain a unique solution. The smoothness assumptions are however easily violated by high-contrast (BV-like) images. We show in Chapter 6 that the proposed texture generation is a convergent regularization method, introducing a modeling error and therefore influencing the data term. An alternative to the above described signal filtering is to simply smooth the photoacoustic images prior to estimating the displacement vector field, to make them applicable for optical flow computations [BSW05]. In experiments, we compare these approaches with computations of the unaltered reconstructions. We show that compared to other smoothing techniques, like for instance Gaussian filtering, the speckling approach performs better on high-contrast image data.

2.5 Discussion and Outlook

In Chapter 3 and Chapter 4 we present an H^1 regularizing reconstruction technique, that somehow constitutes a change of paradigm in Photoacoustics, at least in the case of variable sound speed coefficients. Rather than working with a reconstruction technique that only gives stability in the case of noise-free, exact data, we introduce a Landweber iterative approach that provides convergence in terms of regularization theory. The obvious next step seems to transfer this idea to, call it more sophisticated, modern or state of the art, different regularization techniques, as TV regularization (as it has been done for the spherical mean operator in, e.g., [Sch+09; DGK14]). This would, however, need a careful (and currently not existing) analysis of the wave equation with BV initial data. Photoacoustic imaging that takes into account attenuation could be another potential application for reconstruction techniques, since in this case the photoacoustic reconstruction becomes severely ill-posed (see, e.g., [KSB11]).

In the present approach, the implementation of the wave equation is done in the interior domain by finite element discretization in space, finite differences are used for time discretization. This is coupled with a boundary element formulation of the wave equation in the exterior domain, where the parameters are constant (see Section 3.3). Using conforming finite elements for the wave equation, even if they are of higher order (quadratic elements in our case) leads to artifacts arising from high gradient regions of the initial value function. It seems that in the current implementation, this can only be avoided by choosing a fine discretization in space (demanding a very fine discretization in time, when an explicit scheme is used). Here, a more careful choice of discretization, as provided by discontinuous Galerkin methods, could be a remedy.

2.6 Outline

Chapter 3 contains the manuscript *A Direct Method for Photoacoustic Tomography with Inhomogeneous Sound Speed*, introducing an iterative, regularizing reconstruction technique for photoacoustic tomography in the case of varying speed of sound. The approach is compared to time reversal.

- **Authors & Contributions**: The authors are Z. Belhachmi (Université de Haute Alsace, Mulhouse), TG and O. Scherzer (University of Vienna, RICAM Linz). The development of this article was a gradual, cooperative process. Each of the authors made significant contributions to every part of the paper.

- **Publication status**: The paper has been accepted for publication in *Inverse Problems*, Article reference: IP-100671.R1. A preprint is available on Arxiv [BGS15a].

Chapter 4 contains the manuscript *Photoacoustic Tomography With Spatially Varying Compressibility and Density*. It applies both time reversal and Landweber reconstruction to the acoustic wave equation with inhomogeneous compressibility κ and density ρ. It covers the cases of noisy and partial measurement data. Moreover, the possible consequences of the modeling error introduced by reconstruction within the usual wave model are depicted numerically.

- **Authors & Contributions**: The authors are Z. Belhachmi (Université de Haute Alsace, Mulhouse), TG and O. Scherzer (University of Vienna, RICAM Linz). The development of this article was a gradual, cooperative process. Each of the authors made significant contributions to every part of the paper.

- **Publication status**: The paper has been submitted to the *Journal of Inverse and Ill-posed Problems*. A preprint is available on Arxiv [BGS15b].

Chapter 5 contains the manuscript *Non-Equispaced Grid Sampling in Photoacoustics with a Non-Uniform FFT*. It treats an accurate discretization of a frequency domain reconstruction formula on planar measurement domains, that moreover gives the option to place the detectors in a non-equispaced way. Numerical reconstructions from experimental and synthetic data show the feasibility of the approach for photoacoustic imaging.

- **Authors & Contributions**: The authors are J. Schmid (University of Vienna, Medical University of Vienna), TG (University of Vienna), B. Zabihian, M. Liu, W. Drexler (all Medical University of Vienna) and O. Scherzer (University of Vienna, RICAM Linz). The development of this article was a gradual, cooperative process. Each of the authors made significant contributions to the paper. The authors affiliated to the University of Vienna contributed to the theoretical and numerical parts of the article. The authors affiliated to the Medical University of Vienna contributed to the experimental parts of the article.

- **Publication status**: The paper has been accepted for publication in the *Journal of Biomedical Optics*. A preprint of the original submission is available on Arxiv [Sch+15].

Finally, Chapter 6 is a layout-adapted version of the article *Texture Generation for Photoacoustic Elastography*. A convolution result for the photoacoustic operator is applied to describe artificial speckle patterns obtained from reconstruction with specific band-limited data. In an elastographic application, this texturing is shown to serve as additional regularization in the data term of the Tikhonov functional. The results are accompanied by synthetic elastographic experiments, which show that the introduced speckle patterns can reduce the angular and distance error in optical flow computations.

- **Authors & Contributions**: The authors are TG, O. Scherzer (University of Vienna, RICAM Linz) and T. Widlak (University of Vienna, now ENS Paris). The development of this article was a gradual, cooperative process. Each of the authors made significant contributions to every part of the paper.

- **Publication status**: Published, reference [GSW15]. A preprinted version is available on Arxiv [GSW14].

Part II

Publications and Manuscripts

3

A Direct Method for Photoacoustic Tomography With Inhomogeneous Sound Speed

Zakaria Belhachmi, Thomas Glatz and Otmar Scherzer

Abstract

The standard approach for photoacoustic imaging with variable speed of sound is *time reversal*, which consists in solving a well-posed final-boundary value problem for the wave equation backwards in time. This paper investigates the iterative Landweber regularization algorithm, where convergence is guaranteed by standard regularization theory, notably also in cases of *trapping* sound speed or for short measurement times. We formulate and solve the direct and inverse problem on the *whole* Euclidean space, what is common in standard photoacoustic imaging, but not for time-reversal algorithms, where the problems are considered on a domain enclosed by the measurement devices. We formulate both the direct and adjoint photoacoustic operator as the solution of an interior and an exterior differential equation which are coupled by transmission conditions. The prior is solved numerically using a Galerkin scheme in space and finite difference discretization in time, while the latter consist in solving a boundary integral equation. We therefore use a BEM-FEM approach for numerical solution of the forward operators. We analyze this method, prove convergence, and provide numerical tests. Moreover, we compare the approach to time reversal.
Keywords: Photoacoustic Imaging, Variable Sound Speed, Regularization

Introduction

Photoacoustic Imaging (PAI) is a novel imaging technique that allows for three dimensional imaging of small biological or medical specimens with high spatial resolution. It utilizes that an object expands and emits ultrasound waves when it is exposed to a short pulse of electromagnetic radiation (see, e.g., [XW06; Wan09]). The emitted ultrasound pressure is assumed to be proportional to the electromagnetic *absorption density* which provides detailed anatomical and functional information. PAI aims for visualization of the absorption density by using measurements of the emitted wave outside of the object.

Opposed to the standard PAI problem [KK08; Wan08; Wan09] we assume a spatially varying speed of sound. The underlying mathematical model of the wave propagation with spatially varying sound speed $c(x)$ is the *acoustic wave equation*

$$\begin{aligned} \frac{1}{c^2(x)} y''(x,t) - \Delta y(x,t) = 0 \text{ in } \mathbb{R}^n \times (0,\infty), \\ y(x,0) = f(x) \text{ in } \mathbb{R}^n, \\ y'(x,0) = 0 \text{ in } \mathbb{R}^n \end{aligned} \tag{3.0.1}$$

where f denotes the absorption density, which is proportional to the absorbed electromagnetic energy.

The *inverse problem* of photoacoustics with variable wave speed consists in determining the function f from measurement data m of y on a surface $\partial\Omega$ over time $(0,T)$. With constant sound speed there exists a variety of analytical reconstruction formulas and numerical inversion techniques. We mention [XFW02; XXW03; XW02; XXW02], see also the surveys [KK08; Wan09; KK11; WA11]. In the case of inhomogeneous sound speed, exact reconstruction formulas have been derived in [AK07]. A numerical method, providing approximations, is *time reversal* [Fin92; Grü+07; Gr07; HKN08], where a space-time boundary value problem for the wave equation is solved backwards in time. Thereby the measurement data serve as Dirichlet boundary data, and the *initial* conditions at final observation time T are assumed to be identically zero. On top of the original algorithm of Fink [Fin92], the approach in [SU09] suggests a harmonic extension of the boundary data at time T as initialization data. The reconstruction obtained by time-reversal, lets say f_T, approximates the true solution f as T increases to infinity. The exact f can be reconstructed if $y(\cdot,T) \equiv 0$, which happens, aside from trivial cases, only in odd dimensions and for homogeneous sound speed. In all other cases the results are error-prone. Moreover, this method produces approximations of f only under *non-trapping* conditions on c (see [HKN08; Hri09]).

Stefanov and Uhlmann [SU09] showed that if $\operatorname{diam}(\Omega) = 2T_0$ (where $\operatorname{diam}(\Omega)$ denotes the diameter of Ω with respect to the Riemannian metric $c^{-2}dx$), then an observation time $T > T_0$ is sufficient for a unique reconstruction of f. However, for stability of the inverse problem one needs longer measurement times and a non-trapping speed of sound condition. In fact, if the measurement time T is larger than a certain threshold, depending on the longest geodesic in the metric induced by c, the algorithm presented in [SU09] provides a theoretically exact reconstruction in terms of a Neumann series that contains multiple, subsequent time reversal and forward propagation of the data term. A computational realization of this approach has been investigated in [Qia+11]. This algorithm serves as a benchmark for our proposed algorithm.

The presented approach for PAI inversion with variable sound speed relies on linear regularization theory [Gro84]. Specifically, we obtain regularized convergence to the *minimum norm solution* even for short measurement times. Moreover, we obtain a new reconstruction method that does not require an artificial cut-off of the measurement data, nor harmonic extension of the data at the final observation time T. The approach can be regarded as natural generalization of backprojection, as it uses the adjoint operator in the backpropagation step of the reconstruction. As in backprojection, the solution of the adjoint problem is computed on an unbounded spatial domain, rather than solving a boundary value problem in time reversal.

For the numerical computations, we decouple the wave equation into an interior part (solved by finite element methods), and an exterior part (with homogeneous sound speed) that is rewritten in terms of a boundary integral formulation. We then solve the coupled BEM-FEM system numerically. Note that by this approach we use exact, non-reflecting boundary conditions [Abb+11; FM14] and therefore avoid the necessity of a *perfectly matched layer* to deal with the cut-off outside the domain of interest.

Since this formulation allows for inhomogeneous transmission conditions, it is also well-suited for the solution of the adjoint problem. The results are compared to conventional

time reversal and the Neumann-series approach.

The paper is organized as follows: In Section 4.2 we formulate the direct photoacoustic operator L in a suitable choice of function spaces, and derive the adjoint. In Subsection 4.3.1 we give a short overview about Landweber iteration and review some regularization results regarding convergence and convergence rates in view of PAI reconstruction. Moreover, we discuss the relation to the Neumann series approach in [SU09]. In Section 3.3, we formulate the transmission problem for the wave equation used for numerical computation of both the direct and the adjoint problem. We state the boundary relations used for taking into account the exterior domain. In addition, we briefly describe the used discretization. Finally, Section 5.9 provides a comparison of our reconstruction algorithm with the state-of-the-art reconstruction by time reversal and the *enhanced* time reversal Neumann series method from [SU09].

All along this paper we use the following notation and abbreviations:

Notation 3.0.1: Let Ω be a non-empty, open, bounded and connected domain in $\mathbb{R}^n$ with C^1-boundary $\partial\Omega$. The vector $\boldsymbol{n}(x)$, with $x \in \partial\Omega$, denotes the outward pointing unit normal vector. We use the following sets

$$\Omega^+ := \mathbb{R}^n \backslash \overline{\Omega},\ \Omega^- := \Omega \text{ and } \Sigma := \partial\Omega \times (0,T)\,.$$

We use the following Hilbert spaces:

- $L^2(\Omega) = \{\rho \in L^2(\mathbb{R}^n) : \rho \equiv 0 \text{ in } \mathbb{R}^n \backslash \Omega\}$, with inner product

$$\langle \rho_1, \rho_2 \rangle_{L^2(\Omega)} = \int_{\mathbf{R}^n} \rho_1(x)\rho_2(x)\,dx\,.$$

- For $\hat{\Omega} = \Omega$ or $\mathbb{R}^n$:
  - Let $H_0^1(\hat{\Omega})$ be the closure of differentiable functions on $\mathbb{R}^n$ with compact support in $\hat{\Omega}$, associated with the inner product

$$\langle \rho_1, \rho_2 \rangle_{H_0^1(\hat{\Omega})} = \int_{\mathbf{R}^n} \nabla\rho_1(x) \cdot \nabla\rho_2(x)\,dx\,.$$

  - $H^1(\hat{\Omega})$ denotes the standard Sobolev space with inner product

$$\langle \rho_1, \rho_2 \rangle_{H^1(\hat{\Omega})} = \int_{\hat{\Omega}} \rho_1(x)\rho_2(x) + \nabla\rho_1(x) \cdot \nabla\rho_2(x)\,dx\,.$$

- $L^2(\partial\Omega)$ denotes the standard Hilbert space of square integrable functions on $\partial\Omega$ with inner product

$$\langle \phi_1, \phi_2 \rangle_{L^2(\partial\Omega)} = \int_{\partial\Omega} \phi_1(x)\phi_2(x)\,dS(x)\,.$$

  $L^2(\Sigma)$ denotes the standard Hilbert space of square integrable functions on Σ with inner product

$$\langle \phi_1, \phi_2 \rangle_{L^2(\Sigma)} = \int_0^T \int_{\partial\Omega} \phi_1(x,t)\phi_2(x,t)\,dS(x)dt\,.$$

- The induced norms are denoted by $\|\cdot\|_{L^2(\Omega)}$, $\|\cdot\|_{L^2(\Sigma)}$, $\|\cdot\|_{H^1(\hat{\Omega})}$ and $\|\cdot\|_{H_0^1(\hat{\Omega})}$, respectively.

  For Ω bounded, on $H_0^1(\Omega)$, the norms $\|\cdot\|_{H_0^1(\Omega)}$ and $\|\cdot\|_{H^1(\Omega)}$ are equivalent (see [Ada75, Theorem 6.28]):

$$C_0 \|\rho\|_{H^1(\Omega)} \leq \|\rho\|_{H_0^1(\Omega)} \leq \|\rho\|_{H^1(\Omega)} \qquad \text{for all } \rho \in H_0^1(\Omega). \tag{3.0.2}$$

- The trace operator $\gamma_\Omega : H^1(\mathbb{R}^n) \to L^2(\partial\Omega)$ restricts functions defined on $\mathbb{R}^n$ onto $\partial\Omega$, respectively. This operator is the decomposition of the standard trace operator

$$\gamma : H^1(\Omega) \to L^2(\partial\Omega)$$

  and the restriction operator

$$R : H^1(\mathbb{R}^n) \to H^1(\Omega),$$

  and thus as a composition of two bounded operators [Ada75, Theorem 5.22] bounded. We abbreviate the norm with

$$\mathcal{C}_\gamma := \|\gamma \circ R\| \,. \tag{3.0.3}$$

Notation 3.0.2: The absorption density f and the sound speed c^2 are supposed to satisfy:

- $c \in C^1(\overline{\Omega})$, satisfies $0 < c_{min} \leq c(x) \leq c_{max}$ and c is non-constant in Ω.
- Without loss of generality we assume that $c \equiv 1$ in Ω^+.
- The absorption density function $f \in H_0^1(\Omega)$ is compactly supported in Ω: $\operatorname{supp}(f) \subseteq \Omega$.
- We denote by $|\Omega| := \int_\Omega 1 dx$ the area of Ω.

For the sake of simplicity of notation we omit space and time arguments of functions whenever this is convenient.

3.1 Direct Problem of Wave-Propagation

We analyze the *wave operator* L mapping the absorption density f onto the solution y of the wave equation (4.1.1) restricted to Σ. That is

$$L : H_0^1(\Omega) \to L^2(\Sigma), \quad f \mapsto y|_\Sigma \,. \tag{3.1.1}$$

In the following we show that L is bounded. Let us write

$$E(t) := \int_{\mathbf{R}^n} \frac{1}{c^2} (y')^2 + |\nabla y|^2 \, dx \,. \tag{3.1.2}$$

Computing the derivative of E with respect to t and taking into account (4.1.1) gives

$$E'(t) = 2 \int_{\mathbf{R}^n} \frac{1}{c^2} y'' y' - \Delta y \, y' \, dx = 0 \,.$$

Consequently

$$E(t) = E(0) = \|f\|^2_{H_0^1(\Omega)}\,, \tag{3.1.3}$$

which implies that

$$\frac{1}{c^2_{\max}}\int_{\mathbf{R}^n}(y')^2\,dx \le \int_{\mathbf{R}^n}\frac{1}{c^2}\,(y')^2\,dx \le E(t) = \|f\|^2_{H_0^1(\Omega)} \tag{3.1.4}$$

and

$$\|y(t)\|_{H_0^1(\mathbf{R}^n)} = \int_{\mathbf{R}^n}|\nabla y|^2 dx \le E(t) \le \|f\|_{H_0^1(\Omega)} \tag{3.1.5}$$

for every $t \in (0,T)$.

Lemma 3.1.1 *Let y be the solution of (4.1.1), then*

$$\|y(t)\|_{H^1(\mathbf{R}^n)} \le \mathcal{C}(T)\,\|f\|_{H_0^1(\Omega)}\,, \qquad \textit{for all } t \in (0,T)\,. \tag{3.1.6}$$

with

$$\mathcal{C}(T) := \sqrt{1 + \frac{2}{C_0^2}\max\{1, c^2_{\max}T^2\}}\,,$$

where C_0 is defined in (3.0.2).

Proof: First, we note that for arbitrary $t \in (0,T)$, it follows from (3.1.4) that:

$$\begin{aligned}
\int_{\mathbf{R}^n}(y(x,t)-y(x,0))^2\,dx &= \int_{\mathbf{R}^n}\left(\int_0^t y'(x,\hat{t})\,d\hat{t}\right)^2 dx \\
&\le t\int_{\mathbf{R}^n}\int_0^t (y'(x,\hat{t}))^2\,d\hat{t}\,dx \\
&= t\int_0^t\int_{\mathbf{R}^n}(y'(x,\hat{t}))^2\,dx\,d\hat{t} \\
&\le c^2_{\max}t^2\,\|f\|^2_{H_0^1(\Omega)} \\
&\le c^2_{\max}T^2\,\|f\|^2_{H_0^1(\Omega)}\,.
\end{aligned}$$

Because $(a-b)^2 \ge \frac{1}{2}a^2 - b^2$ it follows from (3.0.2) that

$$\begin{aligned}
\int_{\mathbf{R}^n}(y(x,t))^2\,dx &\le 2\int_{\mathbf{R}^n}(y(x,t)-y(x,0))^2\,dx + 2\int_{\mathbf{R}^n}(y(x,0))^2\,dx \\
&\le 2c^2_{\max}T^2\,\|f\|^2_{H_0^1(\Omega)} + 2\,\|f\|^2_{L^2(\Omega)} \\
&\le 2\max\left\{1, c^2_{\max}T^2\right\}\|f\|^2_{H^1(\Omega)}\,.
\end{aligned}$$

Because $f \in H_0^1(\Omega)$ it follows that

$$\|y(t)\|^2_{L^2(\mathbf{R}^n)} \le \frac{2}{{C_0}^2}\max\left\{1, c^2_{\max}T^2\right\}\|f\|^2_{H_0^1(\Omega)}\,.$$

This, together with (3.1.5) shows that for all $t \in (0,T)$:

$$\|y(t)\|_{H^1(\mathbf{R}^n)} \leq \sqrt{1+\frac{2}{C_0^2}\max\{1, c_{\max}^2 T^2\}}\,\|f\|_{H_0^1(\Omega)}\,.$$

□

In the following we prove boundedness of L:

Theorem 3.1.2 *The operator $L : H_0^1(\Omega) \to L^2(\Sigma)$ is bounded and*

$$\|L\| \leq \mathcal{C}_\gamma \mathcal{C}(T)\sqrt{T}\,. \tag{3.1.7}$$

Proof: For given f let y be the solution of (4.1.1)). From (4.2.2) it follows that the solution y of (4.2.5) is in $H^1(\mathbb{R}^n)$ for every $t > 0$. Thus from (4.1.6) and (4.2.5) it follows that

$$\|y\|_\Sigma^2 = \int_0^T \int_{\partial\Omega} y^2(t)\,d\sigma dt \leq \mathcal{C}_\gamma^2 \int_0^T \|y(t)\|_{H^1(\mathbf{R}^n)}^2\,dt \leq \mathcal{C}_\gamma^2 \mathcal{C}(T)^2 T\,\|f\|_{H_0^1(\Omega)}^2\,,$$

which gives the assertion.

Remark 3.1.3 (Injectivity of L): In order to obtain injectivity of L, we need T to be sufficiently large. To specify this, we define

$$T_0 := \max_{x\in\Omega}(\operatorname{dist}(x,\partial\Omega))\,, \tag{3.1.8}$$

where $\operatorname{dist}(x,\partial\Omega)$ is the distance of x to the closest point $x' \in \partial\Omega$ with respect to the Riemannian metric $c^{-2}dx$ (see also [Qia+11]). From [SU09, Thm. 2] it follows that if $T > T_0$, than $L[f] = 0$ implies $f = 0$ in $(0,T)\times\mathbb{R}^n$.

□

In the following we characterize the adjoint of $L : H_0^1(\Omega) \to L^2(\Sigma)$ on a dense subset of $L^2(\Sigma)$. Because we know from elementary functional analysis that $L^* : L^2(\Sigma) \to H_0^1(\Omega)$ is bounded, we get a characterization of the whole space by limits of convergent sequences.

Definition 3.1.4 Let i be the embedding operator from $H_0^1(\Omega)$ to $L^2(\Omega)$. Then $i^* : L^2(\Omega) \to H_0^1(\Omega)$ is the operator which maps a function $\psi \in L^2(\Omega)$ onto the solution of the equation

$$-\Delta u = \psi \text{ in } \Omega\,, \qquad u = 0 \text{ on } \partial\Omega\,.$$

That is

$$i^* = -\Delta^{-1}\,, \tag{3.1.9}$$

where Δ is the Laplace-operator with homogeneous Dirichlet boundary conditions.

In the following we derive the adjoint L^* : of the operator L, which is required for the implementation of the Landweber iteration below.

Theorem 3.1.5 *For $h \in C^\infty((0,T)\times\partial\Omega)$ the adjoint of the operator L, defined in (4.2.1), is given by*

$$L^*[h] = i^* \circ L_D^*[h] \tag{3.1.10}$$

where

$$L_D^*[h] = \frac{1}{c^2}\, z'(0)\Big|_\Omega\,, \tag{3.1.11}$$

and $z := z(h)$ *is the weak solution of*

$$\begin{aligned} \frac{1}{c^2}\, z'' - \Delta z = 0 \ \textit{in}\ \mathbb{R}^n \backslash \partial\Omega \times (0,T)\,, \\ z(T) = z'(T) = 0 \ \textit{in}\ \mathbb{R}^n, \\ [z] = 0\,, \quad \left[\frac{\partial z}{\partial \boldsymbol{n}}\right] = h \ \textit{on}\ \partial\Omega \times (0,T)\,. \end{aligned} \tag{3.1.12}$$

Here

$$[z] := z^+|_\Sigma - z^-|_\Sigma \ \textit{and}\ \left[\frac{\partial z}{\partial \boldsymbol{n}}\right] := \frac{\partial z^+}{\partial \boldsymbol{n}}\bigg|_\Sigma - \frac{\partial z^-}{\partial \boldsymbol{n}}\bigg|_\Sigma$$

where $z^+ := z|_{\Omega^+ \times (0,T)}$ *and* $z^- := z|_{\Omega \times (0,T)}$.

Proof: For $h \in C^\infty((0,T) \times \partial\Omega)$ the existence of a weak solution of (3.5.2) is proven in the Appendix. Taking $v = y$ where y denotes the solution of (4.1.1) it follows that

$$\begin{aligned} \int_\Sigma hL[f]\, dS(x)dt &= \int_\Sigma hy\, dS(x)dt \\ &= \int_\Omega \frac{z'(0)}{c^2} f\, dx \\ &= \int_\Omega \Delta\left[\Delta^{-1}\left[\frac{z'(0)}{c^2}\right]\right] f\, dx \\ &= -\int_\Omega \nabla\left(\Delta^{-1}\left[\frac{z'(0)}{c^2}\right]\right) \cdot \nabla f\, dx \\ &= \int_\Omega \nabla i^*\left[\frac{z'(0)}{c^2}\right] \cdot \nabla f\, dx \\ &= \left\langle i^*\left[\frac{z'(0)}{c^2}\right], f\right\rangle_{H_0^1(\Omega)}. \end{aligned} \tag{3.1.13}$$

□

Existence of a weak solution of the equation (4.2.10) follows from the result in the Appendix, which is proven along the lines of [Eva98]. This kind of weak solution, used here, requires in fact differentiable transmission data h. There might exist weaker solution concepts, which directly guarantee existence of a solution if $h \in L^2$, but the currently used result is not applicable in this sense, and therefore we have to use a density argument to give a meaning to the solution of (4.2.10) in the case that the transmission data is only in L^2.

3.2 Landweber Iteration for Solving the Inverse Problem of Photoacoustics

The *photoacoustic imaging problem* rewrites as the solution of the operator equation:

$$L[f] = m\,. \tag{3.2.1}$$

If the null-space of L is non-trivial, then iterative regularization algorithms, in general, when m is an element of the range of L reconstruct the *minimum norm solution*

$$f^\dagger = L^\dagger[m]\,, \tag{3.2.2}$$

where $L^\dagger$ denotes the Moore-Penrose inverse of L (see [Nas76] for a survey on Moore-Penrose inverses).

We propose to use the Landweber's iteration for solving (4.3.1), because it can be compared with time reversal methods, which are the standard references in this field. More efficient regularization algorithms are at hand [Han95], but these are less intuitive to be compared with time reversal. For photoacoustic reconstruction, a conjugate gradient approach incorporating a quadratic approximation of the sound speed was proposed in [MAR10].

In numerical applications and with constant speed of sound, variational methods, like TV (total variation) minimization, have been implemented [ZWZ12; DGK14]. Such an approach can lead to sharper reconstructions of f when it is piecewise constant. However, so far, a profound theoretical analysis exists only for the spherical mean operator [Sch+09, Proposition 3.82] and is yet missing for the photoacoustic operator (4.2.1).

In the following we review properties of the Landweber iteration in an abstract setting (see [Gro84; EHN96]). We use the same notation for the abstract operator and the photoacoustic operator and measurement data m, m^δ, respectively, in order to have direct connection.

3.2.1 Abstract Landweber Regularization

Everything that is formulated below is based on the following assumption:

Assumption 3.2.1: Let $L : H_1 \to H_2$ be an operator between Hilbert spaces H_1 and H_2 satisfying $\omega \|L\|^2 \leq 1$ for some $\omega > 0$. Moreover, we assume that data m^δ of m is available (typically considered as noisy data), which satisfy

$$\left\| m - m^\delta \right\|_{H_2} \leq \delta\,. \tag{3.2.3}$$

Then the Landweber iteration reads as follows:

$$f_0 := 0 \quad \text{and} \quad f_k^\delta = f_{k-1}^\delta - \omega L^*[L[f_{k-1}^\delta] - m^\delta]\,, \quad k = 1, 2, \dots\,. \tag{3.2.4}$$

In case $\delta = 0$, that is, if $m^\delta = m$, then we write f_k instead of f_k^δ.

Let $\tau > 1$ be some fixed constant. The Landweber iteration is only iterated for $k = 1, 2, \dots$ as long as

$$\left\| m^\delta - L[f_k^\delta] \right\|_{H_2} > \tau\delta\,. \tag{3.2.5}$$

The index, where (3.2.5) is violated for the first time is denoted by $k_*(\delta, m^\delta)$.

The following theorem shows that the Landweber iteration converges to the best-approximating solution:

Theorem 3.2.2 *Let $m \in \mathcal{R}(L)$ (note that the range of L equals the domain of $L^\dagger$).*

- *Let $\delta = 0$, then the Landweber iterates (f_k) (cf. (3.2.4)) converge to the $f^\dagger$, i.e., $\left\| f_k - f^\dagger \right\|_{H^1} \to 0$. In addition, we have the series expansion:*

$$f^\dagger = \sum_{j=0}^{\infty} (I - \omega L^* L)^j [L^*[m]] \, .$$

- *For $\delta > 0$ and m^δ satisfying $\left\| m - m^\delta \right\|_{H_2} \leq \delta$ let $k_*^\delta = k_*(\delta, m^\delta) - 1$ as in (3.2.5). Then*

$$f_{k_*^\delta}^\delta \to_{H_1} f^\dagger \, .$$

Moreover, if $m \notin \mathcal{D}(L^\dagger)$, then $\|f_k\|_{H_1} \to \infty$ as $k \to \infty$.

In the following we prove properties of the wave-operator L, such that we can apply the general regularization results.

3.2.2 Convergence of the Landweber Iteration for the Photoacoustic Problem

In the following we apply Theorem 3.2.2, for the photoacoustic imaging problem.

Corollary 3.2.3 *Let $\omega \leq \frac{1}{\mathcal{C}_\gamma^2 \mathcal{C}^2(T) T} = \mathcal{O}(1/T^3)$ and $L : H_0^1(\Omega) \to L^2(\Sigma)$ as in (4.2.1). Moreover, assume that*

$$\left\| m - m^\delta \right\|_{L^2(\Sigma)} \leq \delta \, .$$

Then the Landweber iterates satisfy:

- *If $\delta = 0$, then*

$$f^\dagger = \sum_{k=0}^{\infty} (I - L^* L)^j [L^*[m]] \, .$$

- *For $\delta > 0$, the Landweber iteration is terminated at $k_*(\delta) := k_*(\delta, m^\delta) - 1$ according to (3.2.5). Then*

$$f_{k_*^\delta}^\delta \to f^\dagger \text{ for } \delta \to 0 \, .$$

- *If $T > T_0$, the reconstruction is unique, and $f_{k_*(\delta)}^\delta$ converges to the unique solution.*

Proof: First, we note that from (4.2.6) it follows that $\omega \|L\|^2 \leq 1$. Then, the first two items follow directly from Theorem 3.2.2.

From the injectivity of L for $T > T_0$ (see Remark 3.1.3) it follows that $f^\dagger = f$, which implies unique reconstruction. □

3.2.3 Comparison with Time Reversal

We compare our approach with different variants of *time reversal*. We formally define the time reversal operator:

$$\bar{L}[h] = z(\cdot, 0)\,, \tag{3.2.6}$$

where z is a solution of

$$\begin{aligned} \frac{1}{c^2} z'' - \Delta z &= 0 \text{ in } \Omega \times (0,T), \\ z(T) = z'(T) &= 0 \text{ in } \Omega, \\ z &= h \text{ on } \partial\Omega \times (0,T), \end{aligned} \tag{3.2.7}$$

The fundamental differences between $\bar{L}$ and L^* are that $\bar{L}$ is defined for functions with support in Ω and that therefore L^* requires a transmission condition in its definition.

Stefanov and Uhlmann [SU09] modified the time reversal approach in the following sense: Rather than assuming (in most cases unjustified) the initial data $z(T) \equiv 0$, they used the harmonic extension of the data term $h(s,T)$, for $s \in \partial\Omega$, as initial datum at T. That is, for

$$-\Delta\phi = 0 \text{ in } \Omega\,, \text{ with } \phi(\cdot) = m(\cdot, T) \text{ on } \partial\Omega$$

the modified time-reversal operator

$$\tilde{\bar{L}}[h] = z(\cdot, 0) \tag{3.2.8}$$

is defined by the solution of equation

$$\begin{aligned} \frac{1}{c^2} z'' - \Delta z &= 0 \text{ in } \Omega \times (0,T), \\ z(T) = \phi\,, \quad z'(T) &= 0 \text{ in } \Omega, \\ z &= h \text{ on } \partial\Omega \times (0,T)\,. \end{aligned} \tag{3.2.9}$$

They were able to show that under non-trapping conditions and for sufficiently large measurement time T, there exists a compact operator $K : H_0^1(\Omega) \to H_0^1(\Omega)$ satisfying $\|K\| < 1$, and

$$\tilde{\bar{L}} L = Id - K\,, \tag{3.2.10}$$

Therefore, the initial condition f can be expanded into the Neumann series

$$f = \sum_{j=0}^{\infty} K^j[m]\,. \tag{3.2.11}$$

By induction, it is easy to see that the m-th iterate can be written as

$$f_k = f_{k-1} - \tilde{\bar{L}}[L[f_{k-1}] - m]\,, \tag{3.2.12}$$

where

$$f_k = \sum_{j=0}^{k} K^j[m]\,.$$

At this point, we emphasize on the structural similarity between (4.3.11) and (3.2.4).

Remark 3.2.4: We emphasize that for time-reversal there is no theory on stopping in case of error-prone data, such as we have available for the Landweber iteration. In fact, the boundary data have to be in $H^1(\Sigma)$, which follows from $f \in H_0^1(\Omega)$ under the additional assumption that $\operatorname{supp} f \subset \Omega$ *(see [SU09, Remark 5].*

Remark 3.2.5: Compared to time reversal, the smoothness assumptions to the data term can be relaxed when searching for a regularized solution. Indeed, instead of needing H^1-data in the range of L as in time reversal, the present approach gives regularized convergence for a data-term in L^2. The smoothness assumption on the coefficient c is mainly of technical nature, to be able to apply the standard results of microlocal analysis. A careful but tedious analysis might give similar results with less smoothness requirements. The stability for piecewise smooth coefficients has been analyzed in [SU11].

3.3 Numerical Realization of L and L^*

We solve (4.1.1) and (4.2.10) with the same numerical framework. By changing the variable $t \to T - t$ in (4.2.10), both equations can be rewritten as the transmission problem:

$$\begin{aligned} \frac{1}{c^2} v'' - \Delta v = 0 \qquad & \text{in } \mathbb{R}^n \backslash \partial\Omega \times (0,T)\,, \\ v(0) = v_0\,, \quad v'(0) = 0 \qquad & \text{in } \mathbb{R}^n \backslash \partial\Omega\,, \\ \left[\frac{\partial v}{\partial \boldsymbol{n}}\right] = \rho\,, \quad [v] = 0 \qquad & \text{on } \Sigma\,. \end{aligned} \tag{3.3.1}$$

where for (4.1.1) $\rho \equiv 0$ and $v_0 = f \in H_0^1(\Omega)$ and for (4.2.10) we have $\rho \equiv h \in L^2(\Sigma)$ and $v_0 \equiv 0$.

Let $v_0^- = v_0$ in Ω^-, $v_0^+ = 0$ in Ω^+, then $v^\pm = v|_{\Omega^\pm}$ satisfy, respectively:

$$\begin{aligned} \frac{1}{c^2} v_\pm'' - \Delta v_\pm = 0 \qquad & \text{in } \Omega^\pm \times (0,T)\,, \\ v_\pm(0) = v_0^\pm\,, \quad v_\pm'(0) = 0 \qquad & \text{in } \Omega^\pm\,, \end{aligned} \tag{3.3.2}$$

together with the transmission conditions

$$\left[\frac{\partial v}{\partial \boldsymbol{n}}\right] = \rho \text{ and } [v] = 0 \qquad \text{on } \Sigma\,. \tag{3.3.3}$$

Let G denote the fundamental solution of the standard wave equation with $c^2 \equiv 1$ in $\mathbb{R}^n$. It is defined in $\mathbb{R}^n \times \mathbb{R}$, and its explicit expression

$$G(x,t) = \begin{cases} \frac{H(t-|x|)}{2\pi\sqrt{t^2-|x|^2}}, & n = 2\,, \\ \frac{\delta(t-|x|)}{4\pi|x|}, & n = 3\,, \end{cases}$$

with H denoting the Heaviside step function, and $\delta(\cdot)$ being the 3D Dirac delta distribution (see, e.g., [Fri75]).

The *(retarded) single-* and *double- layer potentials* for $(x,t) \in \Sigma$ are defined by

$$\begin{aligned} \mathcal{V}[\varphi](x,t) &:= \int_0^t \int_{\partial\Omega} G(y-x,t-\tau)\varphi(y,\tau) dS_y d\tau \,, \\ \mathcal{K}[\psi](x,t) &:= \int_0^t \int_{\partial\Omega} \frac{\partial G(y-x,t-\tau)}{\partial \boldsymbol{n}} \psi(y,\tau) dS_y d\tau \,. \end{aligned} \tag{3.3.4}$$

Because we assume that $c = 1$ outside of Ω and because we assume that $\partial\Omega$ is a C^1 boundary, it follows that v^+ satisfies (see [HD03]):

$$\frac{1}{2} v^+(x,t) = -\mathcal{V}\left[\frac{\partial v^+}{\partial \boldsymbol{n}}\right](x,t) - \mathcal{K}\left[v^+\right](x,t) \,, \qquad \text{for all } (x,t) \in \Sigma \,. \tag{3.3.5}$$

The transmission conditions imply that

$$v^+ = v^- \text{ and } \frac{\partial v^+}{\partial \boldsymbol{n}} = \frac{\partial v^-}{\partial \boldsymbol{n}} + \rho \text{ on } \Sigma \,.$$

Therefore the equation for $v = v^-$ on $\Omega = \Omega^-$ can be rewritten as follows:

$$\begin{aligned} \frac{1}{c^2} v'' - \Delta v &= 0 \qquad && \text{in } (\Omega) \times (0,T) \,, \\ v(0) = v_0 \,, \quad v'(0) &= 0 \qquad && \text{in } \Omega \,, \\ \frac{1}{2} v + \mathcal{V}\left[\frac{\partial v}{\partial \boldsymbol{n}} + \rho\right] + \mathcal{K}[v] &= 0 \qquad && \text{on } \Sigma \,. \end{aligned} \tag{3.3.6}$$

The numerical solution is based on a weak formulation of (3.3.6). Integrating over Ω, multiplying by $w \in H^1(\Omega)$ and integration by parts of the first line of (3.3.6) gives

$$\frac{d^2}{dt^2} \left\langle \frac{1}{c^2} v(t), w \right\rangle_{L^2(\Omega)} + \langle \nabla v(t), \nabla w \rangle_{L^2(\Omega)} - \left\langle \frac{\partial v}{\partial \boldsymbol{n}}(t), w \right\rangle_{L^2(\partial\Omega)} = 0 \,.$$

Additionally we introduce the unknown function $\lambda := \frac{\partial v}{\partial \boldsymbol{n}}$ defined on Σ. We are therefore searching for a solution $(v,\lambda) \in H^1(\Omega) \times H^{-1/2}(\partial\Omega)$ that satisfies for almost all $t \in (0,T)$ the system

$$\begin{aligned} \frac{d^2}{dt^2} \left\langle \frac{1}{c^2} v(t), w \right\rangle_{L^2(\Omega)} + \langle \nabla v(t), \nabla w \rangle_{L^2(\Omega)} - \langle \lambda, w \rangle_{L^2(\partial\Omega)} &= 0 \qquad && \text{for all } w \in H^1(\Omega) \,, \\ v(0) = v_0 \,, v'(0) &= 0 \qquad && \text{in } \Omega \,, \\ \frac{1}{2} v(t) + \mathcal{V}[\lambda + \rho](t) + \mathcal{K}[v](t) &= 0 \qquad && \text{on } \Sigma \,. \end{aligned} \tag{3.3.7}$$

For detailed analysis of the discretization of equations of that type (3.3.7) we refer to [FM14], since we closely follow their approach.

Next, we discuss the time discretization of the integrals $\mathcal{V}[\lambda]$ and $\mathcal{K}[v]$. We consider a uniform time discretization of the interval $(0,T)$ into N steps of length $\Delta_t = T/N$,

and defining the discrete time levels $t_n = n\Delta_t$. Following [FMS12], by using Lubich's convolution quadrature formula [Lub88], we approximate $\mathcal{V}[\lambda]$ and $\mathcal{K}[v]$ at the time steps t_n, $n = 0, \dots, N$ by

$$\begin{aligned} \mathcal{V}[\varphi](x,t_n) &\approx \sum_{j=0}^{n} \int_{\partial\Omega} w_{n-j}^{\mathcal{V}}(\Delta_t, |x-y|)\varphi(y,t_j)dS_y\,, \\ \mathcal{K}[\psi](x,t_n) &\approx \sum_{j=0}^{n} \int_{\partial\Omega} w_{n-j}^{\mathcal{K}}(\Delta_t, |x-y|)\psi(y,t_j)dS_y\,. \end{aligned} \tag{3.3.8}$$

where the coefficients $w_n^{\mathcal{V}}$ and $w_n^{\mathcal{K}}$ satisfy

$$\begin{aligned} w_n^{\mathcal{V}}(\Delta_t, |x-y|) &= \frac{\beta}{2\pi L} \sum_{l=0}^{L-1} K^{\mathcal{V}}\left(|x-y|, \frac{\gamma(\rho\exp(\mathrm{i}l2\pi/L))}{\Delta_t}\right) \exp(-\mathrm{i}n2\pi/L)\,, \\ w_n^{\mathcal{K}}(\Delta_t, |x-y|) &= \frac{\beta}{2\pi L} \sum_{l=0}^{L-1} K^{\mathcal{K}}\left(|x-y|, \frac{\gamma(\rho\exp(\mathrm{i}l2\pi/L))}{\Delta_t}\right) \exp(-\mathrm{i}n2\pi/L)\,, \end{aligned} \tag{3.3.9}$$

where

$$K^{\mathcal{V}}(r,s) = K_0(rs)\,, \qquad K^{\mathcal{K}}(r,s) = -sK_1(rs)\frac{\partial r}{\partial \boldsymbol{n}}\,,$$

and $K_0(\cdot), K_1(\cdot)$ are the second kind modified Bessel functions of order 0 and order 1, respectively. The function γ is given by $\gamma(z) = 3/2 - 2z + 1/2z^2$ and is the associated characteristic quotient of the used backward differentiation formula method of order two. For the involved constants we choose $L = 2N$ and $\beta = \epsilon^{1/2N}$, where ϵ is the machine precision (see [Lub88; FMS12] for more details).

In the first equation in (3.3.7), the second time derivative is approximated using the second order central difference expression

$$\frac{d^2}{dt^2}v^n = \frac{1}{\Delta t^2}\left(v^{n+1} - 2v^n + v^{n-1}\right) + \mathcal{O}(\Delta t^2)\,,$$

where $v^n := v(.,t_n)$. The first time derivative occurring in the initial condition is also discretized by central differences, namely

$$\frac{d}{dt}v^0 = \frac{1}{2\Delta t}\left(v^1 - v^{-1}\right) + \mathcal{O}(\Delta t^2)\,.$$

From that we can restate the initial conditions as

$$\begin{aligned} &\left\langle v^0, w\right\rangle = \left\langle v^0, w\right\rangle\,, \\ &\left\langle v^1, w\right\rangle = \left\langle \frac{1}{c^2}v^0, w\right\rangle - \frac{1}{2}\Delta t^2\left(\left\langle \nabla v^0, \nabla w\right\rangle - \left\langle \lambda^0, w\right\rangle\right), \quad \text{for all } w \in H^1(\Omega)\,. \end{aligned} \tag{3.3.10}$$

Using this, the explicit Euler discretization of (3.3.7) is stated as

$$\begin{aligned} \frac{1}{\Delta t^2}\left\langle \frac{1}{c^2}(v^{n+1}-2v^n+v^{n-1}),w\right\rangle + \langle \nabla v^n,\nabla w\rangle - \langle \lambda^n,w\rangle = 0, \qquad &\text{for all } w\in H^1(\Omega),\\ \frac{1}{2}v^{n+1}(t)+\mathcal{V}[\lambda+\rho](t_{n+1})+\mathcal{K}[v](t_{n+1})=0 \qquad &\text{on } \Sigma, \end{aligned} \tag{3.3.11}$$

for all $1\leq n\leq N$. Note that in (3.3.10) and (3.3.11) we write $\langle\cdot,\cdot\rangle$ shorthand for the L^2 inner product over either Ω or $\partial\Omega$.

In space Ω is triangulated, and we use piecewise quadratic basis functions, supplemented by one cubic function for v. The functions Λ and $v|_{\partial\Omega}$ are discretized by the use of piecewise linear functions. With this ansatz a mass-lumped integration scheme can be robustly implemented, which is not the case for purely piecewise quadratic functions. The details and numerical analysis to this scheme can be found in [Coh+01].

Remark 3.3.1 (Advantages and limitations): The proposed numerical technique has the potential to be used for very general types of measurement surfaces and does not need an artificial cut-off at the boundary [FM14]. However, it relies on the assumption that the initial source is in H^1. The method naturally introduces errors in presence of large gradients, as occurring at the edges of piecewise constant images. In such cases, a very fine mesh has to be chosen to avoid oscillations in the solution, at the cost of performance. In these cases, the use of non-conforming methods as discontinuous Galerkin might improve the result [Coc03].

3.4 Numerical Experiments and Results

Here, we present numerical results for the Landweber reconstructions and compare it with standard time-reversal reconstructions and the Neumann-series-approach (4.3.10) - always computed with the same discretization. We concentrate in particular on the cases where classical time reversal techniques have their theoretical and practical drawbacks, that is, so-called *trapping speed geometries* and short measurement times. In these cases, neither time reversal nor the Neumann-series (4.3.10) provide theoretical convergence. As we have shown in Corollary 3.2.3, the Landweber reconstruction converges to the least squares solution, regardless of the chosen measurement time. In what follows, we also show the practical applicability of our method in such cases.

To create the data sets, we use the discretization of the coupled method introduced in Section 3.3. The forward computations are performed in a circle of radius 1. The simulation mesh size is $h=0.013$ for the ghosts phantom and $h=0.009$ for the Shepp-Logan phantom. In the reconstructions we use $h_r=0.025$ for the ghosts and $h_r=0.0095$ for the Shepp-Logan. For both simulation and reconstructions, the chosen finite element space is that of continuous, piecewise quadratic functions in space. For the spatial discretization of the boundary terms, we take piecewise linear basis functions. Note that for convenience and to optimize the computational effort, we assume $\partial\Omega$ to be a circle of Radius R. For the time discretization, wo choose the step size $\Delta t=h/(15c_{\max})$ for the simulation and $\Delta t_r=h_r/(14c_{\max})$. Here $c_{\max}$ is the maximum speed of sound. The time reversal reconstructions are obtained by solving the initial boundary value problem

(4.3.6) with homogeneous initial values. In the images, when we used the harmonic extension time-reversal (4.3.9), the heading is *Neumann*. The Landweber reconstruction is performed by the scheme described in Corollary 3.2.3. The choices of c in both the trapping and non-trapping case have been taken from [Qia+11].

3.4.1 Non-Trapping Sound Speed

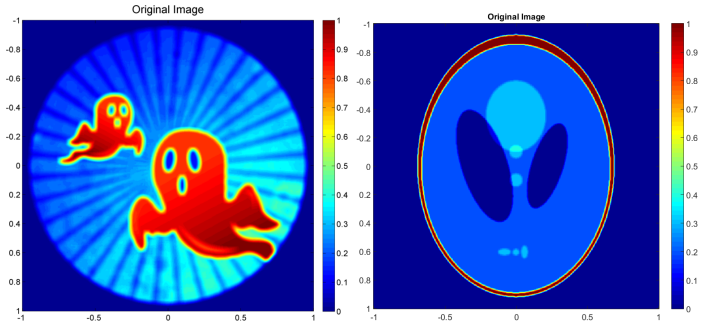

FIGURE 3.1: From left to right: Ghost phantom; Shepp-Logan phantom.

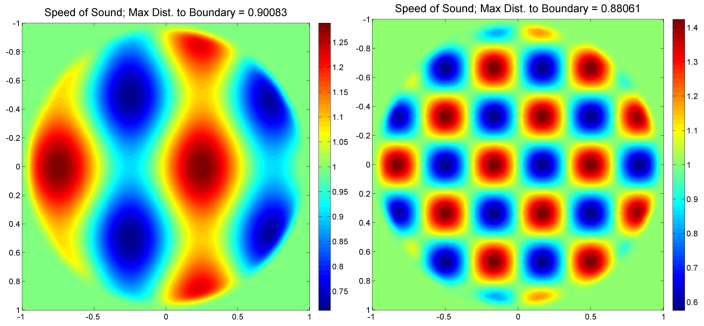

FIGURE 3.2: From left to right: Non-trapping speed; Trapping speed.

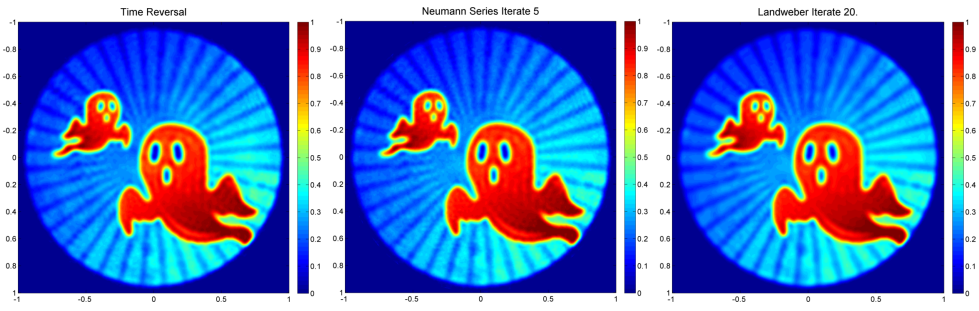

FIGURE 3.3: Data: Non-trapping speed, $T = 4T_0$. From left to right: Time reversal; 5th Neumann sum; Landweber iterate 20.

Let's first consider the case of the non-trapping speed

$$c(x) = \begin{cases} 1 + 0.2\sin(2\pi x_1) + 0.1\cos(2\pi x_2), & x \in B_{R-\varepsilon}\,, \\ 1 \quad \text{outside } B_R\,. \end{cases}$$

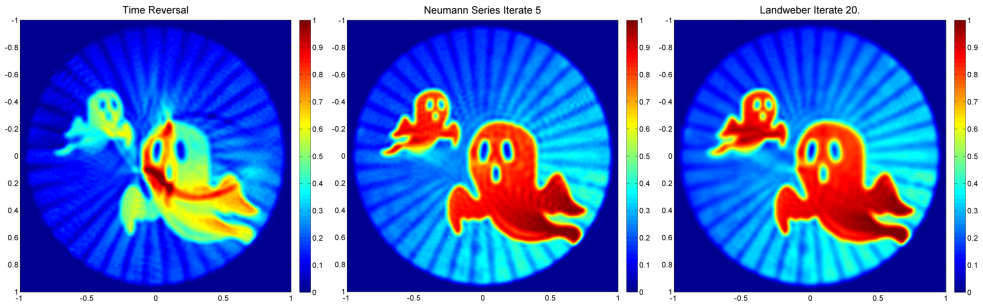

FIGURE 3.4: Data: Non-trapping speed, $T = 1.2T_0$. From left to right: Time reversal; 5th Neumann sum; Landweber iterate 20.

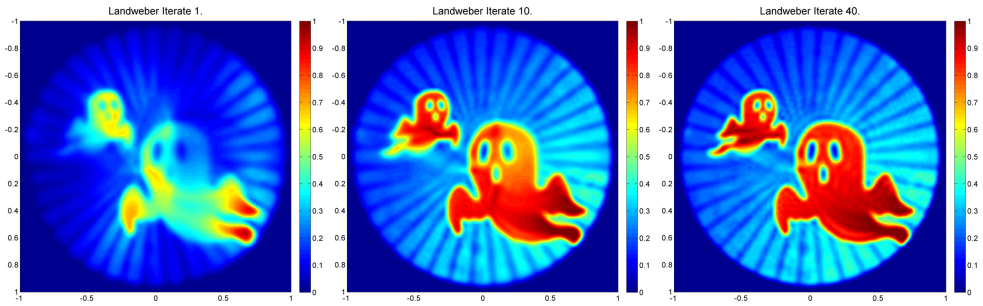

FIGURE 3.5: Landweber reconstruction at different iterations. Data: Non-trapping speed, $T = 1.2T_0$. From left to right: Iterate 1; Iterate 10; Iterate 50.

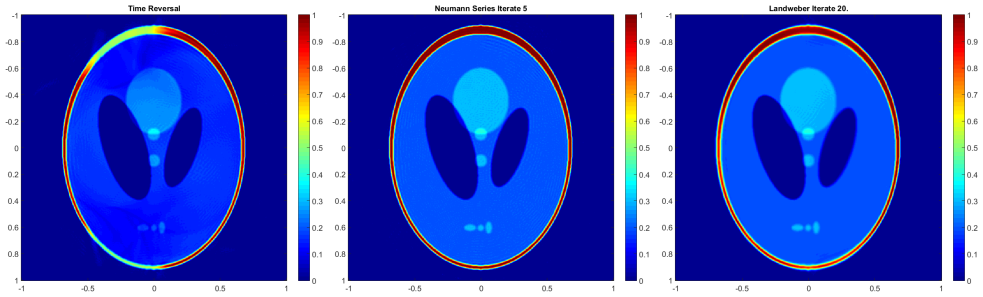

FIGURE 3.6: Data: Non-trapping speed, $T = 2T_0$. From left to right: Time reversal; 5th Neumann sum; Landweber iterate 20.

Note that here and below, the speed of sound is smoothed out near the boundaries to satisfy our smoothness assumptions. The time reversal method already gives reliable reconstructions if the measurement time T is sufficiently large. For the test example, a measurement time of $T = 4T_0$ (see Remark 3.1.3) is enough to provide a quantitatively reasonable reconstruction by time reversal. This is illustrated in Figure 3.3. We therefore are interested in the case where the measurement time is shorter, e.g., with T as near as possible at T_0. In Figure 3.4 we compare the time reversal reconstruction and the Neumann series approach with our method, using $T = 1.2T_0$. The Landweber reconstruction is stopped at a suitable stage of iteration. In practice, the improvement is very large in the first steps, while it needs a lot of iterations to satisfy the discrepancy principle from Theorem 3.2.2.

The main differences are clearly visible to the naked eye: The time reversal reconstruction fails to compute the central point in the image and produces artifacts. These artifacts can be avoided by the use of the harmonic extension as in (4.3.6). We here present iterate $j = 5$ of the Neumann series (4.3.10). Also the Landweber reconstruction avoids to amplify the artifacts in the image center. Moreover, it delivers the correct quantitative values of the initial pressure, whereas time reversal underestimates these values. However, the smoothing step naturally included in every Landweber iteration seems to make this approach more stable than the time reversal Neumann series. In fact, at least with our method of numerical wave propagation, we have to stop the Neumann series after 5-10 iterates before numerical errors are amplified too much.

Remark 3.4.1 (Convergence rates in practice): The main difference between the convergence rates of the Neumann series and the Landweber iteration lies in the division by c^2 after every backpropagation step, indicated by (4.2.9).

In Figure 3.5 we show reconstructions using the non-trapping speed and measurement time $T = 1.2T_0$. The measured error $\left\| y^\delta - Lf_k \right\|_{L^2(\Sigma)}$ keeps decreasing till $k = 50$. However, the major visible improvements seem to occur within the first 20 iterations. We therefore use the picture of iteration number 20 for our practical comparisons with the other methods.

3.4.2 Trapping Sound Speed

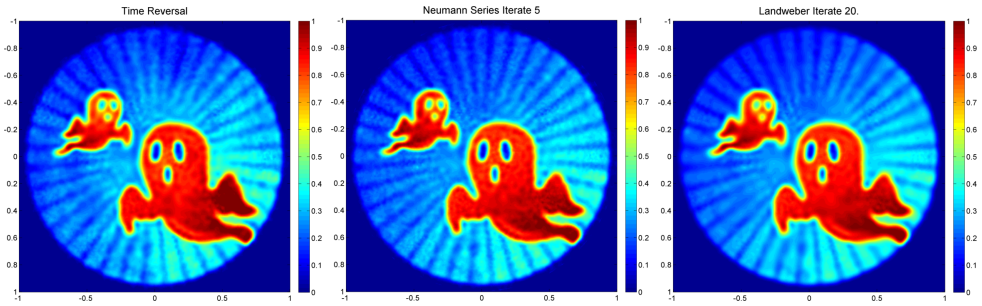

FIGURE 3.7: Data: Trapping speed, $T = 4T_0$. From left to right: Time reversal; 5th Neumann sum; Landweber iterate 20.

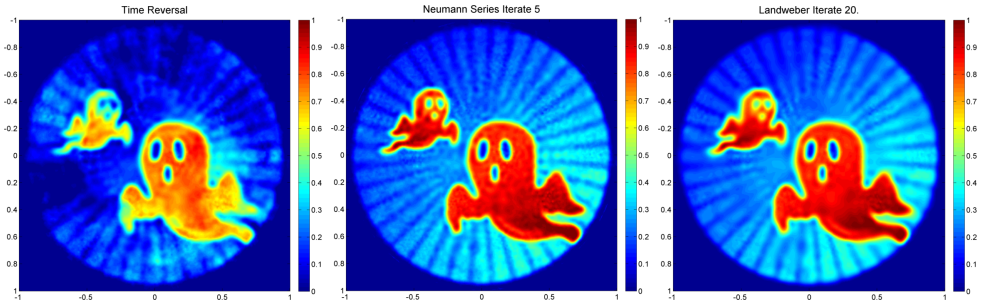

FIGURE 3.8: Data: Trapping speed, $T = 2T_0$. From left to right: Time reversal; 5th Neumann sum; Landweber iterate 20.

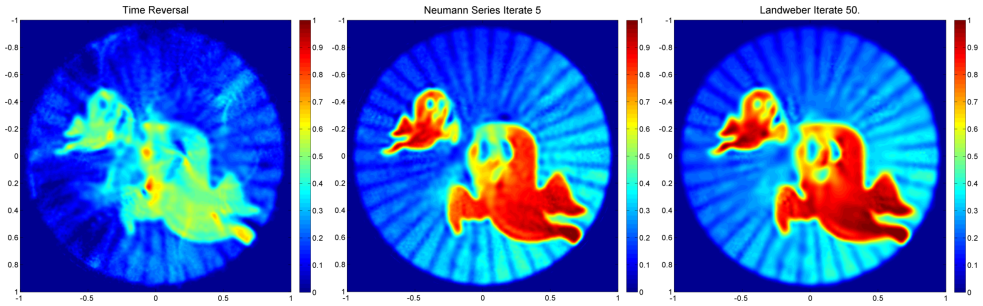

FIGURE 3.9: Data: Trapping speed, $T = 1.2T_0$. From left to right: Time reversal; 5th Neumann sum; Landweber iterate 50.

In the second example, we want to deal with the trapping speed

$$c(x) = \begin{cases} 1 + 0.5\sin(-3\pi x_1)\cos(3\pi x), & x \in B_{R-\varepsilon}\,, \\ 1 \quad \text{outside } B_R\,. \end{cases}$$

In this case, there are geodesics present that do not propagate singularities to the measurement surface within finite time. The Landweber approach is the only one that gives a theoretical convergence result in this case. In practice, we see that conventional time reversal, at least for $T = 1.2T_0$, fails to give a detailed reconstruction. The Neumann series approach and the Landweber iteration behave similarly, again with the advantage of the Neumann series giving faster convergence, whereas the Landweber gives a regularized solution that seems to be more robust against numerical errors and noise (Figure 3.7, Figure 3.8 and Figure 3.9).

3.5 Conclusions

In this paper, an infinite dimensional Hilbert space regularization framework is established for solving the photoacoustic inverse problem with variable speed of sound. The introduced Landweber approach iteratively solves the least squares problem, a standard stopping criterion serves as regularization parameter. By regularization theory, convergence of the method is guaranteed. The reconstruction method is compared to the common state-of-the-art reconstruction techniques in the field, which are based on solving a time reversed wave equation. It thereby proves to be a flexible and feasible alternative for computational photoacoustic tomography with variable speed.

Acknowledgement

The work of TG and OS is supported by the Austrian Science Fund (FWF), Project P26687-N25 Interdisciplinary Coupled Physics Imaging. The authors are grateful to the Erwin Schrödinger institute for warm hosting. Thanks go to the referees for the helpful comments and to Roland Herzog for remarks on the initial version. Special thanks go to Silvia Falletta for providing valuable hints concerning details to discretization and implementation of the coupled system.

Well-Posedness of the Transmission Problem

Notation 3.5.1:

- The space

$$V := \left\{ u \in H_0^1(\mathbb{R}^n) : u|_\Omega \in H^1(\Omega) \right\} \tag{3.5.1}$$

is a Hilbert space with respect to the inner product

$$\langle \phi_1, \phi_2 \rangle_V = \int_\Omega \phi_1(x)\phi_2(x)\,dx + \int_{\mathbb{R}^n} \nabla\phi_1 \cdot \nabla\phi_2\,dx\,.$$

The completeness follows directly from the properties of the Sobolev spaces $H_0^1(\mathbb{R}^n)$ and $H^1(\Omega)$.

The dual space is denoted by V'.

- Let $\mathcal{S} \subseteq \mathbb{R}^n$, then $C_0^\infty(0,T;\mathcal{S})$ denotes the space of functions $v \in C^\infty((0,T)\times\mathcal{S})$ with compact support in $(0,T)$ with respect to t.

Definition 3.5.2 For $h \in C^\infty((0,T)\times\partial\Omega)$. A weak solution z of (4.2.10) satisfies:

- $$z \in L^2(0,T;V)\,, z' \in L^2(0,T;L^2(\mathbb{R}^n))\,, z'' \in L^2(0,T;V'),$$

where V is defined in (3.5.1), together with

- $z(T) = z'(T) = 0$. Note that $V \subseteq L^2(\mathbb{R}^n) \subseteq V'$ and thus $z \in H^1(0,T;L^2(\mathbb{R}^n))$ and $z' \in H^1(0,T;V')$, such that the traces make sense. In fact $z(T) \in L^2(\mathbb{R}^n)$ and $z'(T) \in V'$.

- $$\begin{aligned} &\int_0^T \int_{\mathbb{R}^n} \frac{1}{c^2} z'' v\,dx\,dt + \int_0^T \int_{\mathbb{R}^n} \nabla z(t) \cdot \nabla v(t)\,dx\,dt \\ &= -\int_0^T \int_{\partial\Omega} h(t)v(t)\,dS(x)\,dt\,, \qquad \text{for all } v \in L^2(0,T;V). \end{aligned} \tag{3.5.2}$$

Note, that the definition of a weak solution is not used consistently in the literature. Evans [Eva98], for instance, uses the test functions v time independently, and formulates a weak form of (4.2.10) for almost all $t \in (0,T)$.

Theorem 3.5.3 *For $h \in C^\infty((0,T)\times\partial\Omega)$ there exists a weak solution z of (4.2.10) - that is of (3.5.2).*

Proof: The proof is similar to [Eva98, Section 7.2.2].

1. First we construct a Galerkin-approximation: Let $\{w_k\}_{k=1}^\infty$ be an orthonormal basis of $L^2(\mathbb{R}^n)$, which is an orthogonal basis for $H_0^1(\mathbb{R}^n)$. For fixed m let

$$z_m(t) = \sum_{k=1}^m d_m^k(t) w_k\,, \qquad t \in (0,T)\,,$$

where

$$d_m^k(T) = 0\,, d_m^{k\,\prime}(T) = 0 \text{ meaning that } z_m(T) = z_m'(T) = 0\,. \tag{3.5.3}$$

and

$$\begin{aligned} &\left\langle \frac{z_m''}{c^2}, w_k \right\rangle_{L^2(\mathbf{R}^n)} + \langle z_m, w_k \rangle_{H_0^1(\mathbf{R}^n)} = \langle h, w_k \rangle_{L^2(\Sigma)}\,, \\ &\text{for all } 0 < t < T\,, \text{ for all } k = 1, \ldots, m\,. \end{aligned} \tag{3.5.4}$$

Analogously to [Eva98, Theorem 1, Section 7.2.2] the Galerkin approximation can be shown.

2. The following estimates are different to [Eva98, Theorem 1, Section 7.2.2] and thus included - it is essential to consider an additional time integration. As in [Eva98] we use $z_m'(t) = \sum_{k=1}^m d_m^{k\,\prime}(t) w_k$ as a test function in the Galerkin approximation. However, we do not apply it pointwise for every $\tau \in (0,T)$, but in integrated form. Then from (3.5.4) it follows that

$$\int_\tau^T \int_{\mathbf{R}^n} \frac{z_m''(\hat{t})}{c^2} z_m'(\hat{t}) + \nabla z_m \cdot \nabla z_m' dx d\hat{t} = -\int_{\partial\Omega} \int_\tau^T h(\hat{t}) z_m'(\hat{t}) d\hat{t} dS(x)$$
$$\text{for all } \tau \in (0,T)\,.$$

Partial integration of the right hand side and evaluation of the integral terms on the left hand gives

$$\begin{aligned} &\int_\tau^T \frac{d}{d\hat{t}} \left(\left\| \frac{z_m'(\hat{t})}{c^2} \right\|_{L^2(\mathbf{R}^n)}^2 + \left\| z_m(\hat{t}) \right\|_{H_0^1(\mathbf{R}^n)}^2 \right) d\hat{t} \\ =& 2 \left(\int_{\partial\Omega} \int_\tau^T h'(\hat{t}) z_m(\hat{t})\, d\hat{t} dS(x) - \int_{\partial\Omega} h(\tau) z_m(\tau) dS(x) \right)\,. \end{aligned} \tag{3.5.5}$$

Since $z_m(T) = z_m'(T) = 0$, the left hand side equals

$$-(\|z_m'(\tau)\|_{L^2(\mathbf{R}^n)}^2 + \|z_m(\tau)\|_{H_0^1(\mathbf{R}^n)}^2)\,.$$

Estimating the right hand side by Cauchy-Schwarz-inequality and using mean inequality, we get for an arbitrary $D > 0$:

$$\begin{aligned} &\left\| \frac{z_m'(\tau)}{c^2} \right\|_{L^2(\mathbf{R}^n)}^2 + \|z_m(\tau)\|_{H_0^1(\mathbf{R}^n)}^2 \\ \leq& \frac{1}{D^2} \left(\int_\tau^T \left\| h'(\hat{t}) \right\|_{L^2(\partial\Omega)}^2 d\hat{t} + \|h(\tau)\|_{L^2(\partial\Omega)}^2 \right) \\ &+ D^2 \left(\int_\tau^T \left\| z_m(\hat{t}) \right\|_{L^2(\partial\Omega)}^2 d\hat{t} + \|z_m(\tau)\|_{L^2(\partial\Omega)}^2 \right)\,. \end{aligned}$$

Let

$$\mathcal{C}(h,\tau) := \int_\tau^T \left\| h'(\hat{t}) \right\|^2_{L^2(\partial\Omega)} d\hat{t} + \|h(\tau)\|^2_{L^2(\partial\Omega)} ,$$
$$\hat{\mathcal{C}}(h,t) := \int_t^T \mathcal{C}(h,\tau)\tau ,$$

and using the trace theorem (4.1.6) it follows that

$$\begin{aligned} &\left\| \frac{z_m'(\tau)}{c^2} \right\|^2_{L^2(\mathbf{R}^n)} + \|z_m(\tau)\|^2_{H_0^1(\mathbf{R}^n)} \\ \leq &\frac{1}{D^2}\mathcal{C}(h,\tau) + D^2 C_\gamma^2 \left(\int_\tau^T \left\| z_m(\hat{t}) \right\|^2_{H^1(\Omega)} d\hat{t} + \|z_m(\tau)\|^2_{H^1(\Omega)} \right) . \end{aligned}$$

By integrating of τ over $[t,T]$ we get the following estimate for all $t \in (0,T)$:

$$\begin{aligned} &\int_t^T \left\| \frac{z_m'(\tau)}{c^2} \right\|^2_{L^2(\mathbf{R}^n)} + \|z_m(\tau)\|^2_{H_0^1(\mathbf{R}^n)} \, d\tau \\ \leq &\frac{1}{D^2}\hat{\mathcal{C}}(h,t) + D^2 C_\gamma^2 \int_t^T \left(\int_\tau^T \left\| z_m(\hat{t}) \right\|^2_{H^1(\Omega)} d\hat{t} + \|z_m(\tau)\|^2_{H^1(\Omega)} \right) d\tau . \end{aligned} \tag{3.5.6}$$

In addition, because $z_m(T) = 0$, we know that

$$\begin{aligned} \left(\int_\Omega z_m(\tau) dx \right)^2 &= \left(\int_\Omega z_m(\tau) - z_m(T) dx \right)^2 \\ &= \left(\int_\tau^T \int_\Omega z_m'(\hat{t}) \, dx d\hat{t} \right)^2 \\ &\leq T|\Omega| c_{\max}^4 \int_\tau^T \int_\Omega \left(\frac{z_m'(\hat{t})}{c^2} \right)^2 dx d\hat{t} \\ &= T|\Omega| c_{\max}^4 \int_\tau^T \left\| \frac{z_m'(\hat{t})}{c^2} \right\|^2_{L^2(\mathbf{R}^n)} d\hat{t} . \end{aligned} \tag{3.5.7}$$

Moreover, we know from the inequality from [Eva98, 5.8, Theorem 1] that

$$\left\| z_m(\tau) - \frac{1}{|\Omega|} \int_\Omega z_m(\tau) dx \right\|_{L^2(\Omega)} \leq C_G \|z_m(\tau)\|_{H_0^1(\mathbf{R}^n)} ,$$

which implies that for all $\tau \in (0,T)$:

$$\|z_m(\tau)\|^2_{L^2(\Omega)} \leq \frac{2}{|\Omega|} \left(\int_\Omega z_m(\tau) dx \right)^2 + 2C_G^2 \|z_m(\tau)\|^2_{H_0^1(\mathbf{R}^n)} ,$$

and consequently

$$\|z_m(\tau)\|^2_{H^1(\Omega)} \leq \frac{2}{|\Omega|} \left(\int_\Omega z_m(\tau) dx \right)^2 + (2C_G^2 + 1) \|z_m(\tau)\|^2_{H_0^1(\mathbf{R}^n)} .$$

Thus it follows from (3.5.6) that

$$\begin{aligned}
&\int_t^T \left\| \frac{z_m'(\tau)}{c^2} \right\|_{L^2(\mathbf{R}^n)}^2 + \|z_m(\tau)\|_{H_0^1(\mathbf{R}^n)}^2 \, d\tau \\
\leq & \frac{1}{D^2} \hat{\mathcal{C}}(h,t) \\
& + D^2 C_\gamma^2 (2C_G + 1) \int_t^T \left(\int_\tau^T \left\| z_m(\hat{t}) \right\|_{H_0^1(\mathbf{R}^n)}^2 d\hat{t} + \|z_m(\tau)\|_{H_0^1(\mathbf{R}^n)}^2 \right) d\tau \\
& \quad + \frac{2D^2 C_\gamma^2 (T+1)}{|\Omega|} \int_0^T \left(\int_\Omega z_m(\tau) dx \right)^2 d\tau \, .
\end{aligned} \tag{3.5.8}$$

Taking $t = 0$ then gives

$$\begin{aligned}
&\int_0^T \left\| \frac{z_m'(\tau)}{c^2} \right\|_{L^2(\mathbf{R}^n)}^2 + \|z_m(\tau)\|_{H_0^1(\mathbf{R}^n)}^2 \, d\tau \\
\leq & \frac{1}{D^2} \hat{\mathcal{C}}(h,t) \\
& + D^2 C_\gamma^2 (2C_G + 1)(T+1) \int_0^T \left\| z_m(\hat{t}) \right\|_{H_0^1(\mathbf{R}^n)}^2 d\hat{t} \\
& \quad + \frac{2D^2 C_\gamma^2 (T+1)}{|\Omega|} \int_0^T \left(\int_\Omega z_m(\tau) dx \right)^2 d\tau \, .
\end{aligned} \tag{3.5.9}$$

Thus it follows from (3.5.7) that

$$\begin{aligned}
&\frac{1}{2T|\Omega| c_{\max}^4} \int_0^T \left(\int_\Omega z_m(\tau) dx \right)^2 d\tau + \\
&\quad \frac{1}{2} \int_0^T \left\| \frac{z_m'(\tau)}{c^2} \right\|_{L^2(\mathbf{R}^n)}^2 + \|z_m(\tau)\|_{H_0^1(\mathbf{R}^n)}^2 \, d\tau \\
\leq & \frac{1}{D^2} \hat{\mathcal{C}}(h,t) \\
& + D^2 C_\gamma^2 (2C_G + 1)(T+1) \int_0^T \left\| z_m(\hat{t}) \right\|_{H_0^1(\mathbf{R}^n)}^2 d\hat{t} \\
& \quad + \frac{2D^2 C_\gamma^2 (T+1)}{|\Omega|} \int_0^T \left(\int_\Omega z_m(\tau) dx \right)^2 d\tau \, .
\end{aligned}$$

Choosing D such that

$$\max \left\{ D^2 C_\gamma^2 (2C_G + 1)(T+1), 2|\Omega| D^2 C_\gamma^2 (T+1) \right\} \leq \frac{1}{2} ,$$

provides that

$$\begin{aligned}&\frac{1}{4T|\Omega|c_{\max}^4}\int_0^T\left(\int_\Omega z_m(\tau)dx\right)^2 d\tau+\\&\frac{1}{4}\int_0^T\left\|\frac{z_m'(\tau)}{c^2}\right\|^2_{L^2(\mathbf{R}^n)}+\|z_m(\tau)\|^2_{H_0^1(\mathbf{R}^n)}\,d\tau\\&\leq\frac{1}{D^2}\hat{\mathcal{C}}(h,t)\,.\end{aligned}\tag{3.5.10}$$

Therefore there exists a constant $\mathcal{C}$ such that

$$\max\left\{\|z_m'\|_{L^2(0,T;\mathbf{R}^n)},\|z_m\|_{L^2(0,T;H_0^1(\mathbf{R}^n))},\|z_m|_\Omega\|_{L^2(0,T;H^1(\Omega))}\right\}\leq\mathcal{C}\,,\tag{3.5.11}$$

where the last estimate is again due to inequality [Eva98, 5.8, Theorem 1], already used above.

Because $\{w_k\}$ is a basis it follows from (3.5.4) that for all $v\in L^2(0,T;V)$:

$$\sup_v\left\langle\frac{z_m''}{c^2},v\right\rangle_{L^2(0,T;\mathbf{R}^n)}\leq\sup_v\langle z_m,v\rangle_{H_0^1(0,T;\mathbf{R}^n)}+\sup_v\langle h,v\rangle_{L^2(\Sigma)}\leq C(h,\mathcal{C})\,,$$

where $C(h,\mathcal{C})$ is constant depending on h and $\mathcal{C}$, but is not dependent on m. This shows that $z_m''\in L^2(0,T;V')$.

3. (3.5.10) guarantees that $\{z_m\}$ is uniformly bounded in $L^2(0,T;H_0^1(\mathbb{R}^n))$, and $\{z_m|_\Omega\}$ is uniformly bounded in $L^2(0,T;H^1(\Omega))$. Moreover, $\{z_m'\}$ is uniformly bounded in $L^2(0,T;L^2(\mathbb{R}^n))$, and $\{z_m''\}$ is uniformly bounded in $L^2(0,T;V')$. Thus it has a weakly convergent subsequence, which we again denote by $\{z_m\}$ which is converging weakly in the following sense:

$$\begin{aligned}\{z_m\}&\rightharpoonup z\text{ with respect to }L^2(0,T;H_0^1(\mathbb{R}^n))\,,\\\{z_m|_\Omega\}&\rightharpoonup z|_\Omega\text{ with respect to }L^2(0,T;H^1(\Omega))\,,\\\{z_m'\}&\rightharpoonup\psi\text{ with respect to }L^2(0,T;L^2(\mathbb{R}^n))\,,\\\{z_m''\}&\rightharpoonup\rho\text{ with respect to }L^2(0,T;V')\,.\end{aligned}$$

We note that the trace operator $\gamma:H^1(\Omega)\to L^2(\partial\Omega)$ is bounded. Therefore, every test function $v\in L^2(0,T;V)$ satisfies $v|_{\partial\Omega}\in L^2(0,T;L^2(\partial\Omega))$. Consequently,

$$\int_0^T\int_{\partial\Omega}z_m v\,dS(x),dt\to\int_0^T\int_{\partial\Omega}zv\,dS(x),dt\,.$$

Now, let $v \in C_0^\infty((0,T)\times\mathbb{R}^n)$, then $v', v'' \in C_0^\infty((0,T)\times\mathbb{R}^n)$ as well, such that

$$\begin{aligned}\int_0^T\int_\Omega \psi v dxdt &= \lim \int_0^T\int_\Omega z_m' v dxdt \\ &= -\lim \int_0^T\int_\Omega z_m v' dxdt \\ &= \lim \int_0^T\int_\Omega z v' dxdt \\ &= \lim \int_0^T\int_\Omega z' v dxdt\,,\end{aligned}$$

which implies that $\psi = z'$. Analogously one can show that $z_m'' \to z''$ in $L^2(0,T;V')$. Therefore, z it is a solution of (3.5.2).

□

Theorem 3.5.4 *The solution of* (4.2.10) *is unique in* $L^2(0,T;V)$.

Proof: Let us assume that there exist two solutions z_1, z_2 of (4.2.10). Then

$$\begin{aligned}\frac{1}{c^2}(z_1-z_2)'' - \Delta(z_1-z_2) &= 0 \text{ in } \mathbb{R}^n\backslash\partial\Omega\times(0,T)\,,\\ (z_1-z_2)(T) = (z_1-z_2)'(T) &= 0 \text{ in } \mathbb{R}^n,\\ [(z_1-z_2)] = 0\,,\quad \left[\frac{\partial(z_1-z_2)}{\partial \boldsymbol{n}}\right] &= 0 \text{ on } \partial\Omega\times(0,T)\,.\end{aligned} \tag{3.5.12}$$

But this solution has only a trivial solution, which one sees from (4.2.3) and by noting the boundary conditions at ∞ of an $H_0^1(\mathbb{R}^n)$ function. □

4

Photoacoustic Tomography With Varying Compressibility and Density

Zakaria Belhachmi, Thomas Glatz and Otmar Scherzer

Abstract

This paper investigates photoacoustic tomography with two spatially varying acoustic parameters, the compressibility and the density. We consider the reconstruction of the absorption density parameter (imaging parameter of Photoacoustics) with complete and partial measurement data. We investigate and analyze three different numerical methods for solving the imaging problem and compare the results.
Keywords: Photoacoustic imaging, spatially varying compressibility and density, variable sound speed, regularization, time reversal.

4.1 Introduction

Photoacoustic Imaging (PAI) is a novel technique for tomographical imaging of small biological or medical specimens. The method makes use of the fact that an object expands after being exposed to ultrashort electromagnetic radiation, and emits an ultrasonic wave (see e.g. [XW06; Wan09]). The resulting acoustic pressure is assumed to be proportional to the electromagnetic *absorption*, which is the imaging parameter of Photoacoustics. It provides detailed anatomical and functional information.

Opposed to the conventional photoacoustic imaging [XW06; Wan09], which is based on the assumption that the *compressibility* and *density* of the medium are constant (and thus in turn the sound speed), this paper assumes *both* of these parameters spatially varying. The mathematical model describing the propagation of the ultrasonic pressure considered here is

$$\begin{aligned} \kappa(x)y''(x,t) - \nabla\cdot\Big(\rho(x)^{-1}\nabla y(x,t)\Big) &= 0 \text{ in } \mathbb{R}^n\times(0,\infty)\\ y(x,0) &= f(x) \text{ in } \mathbb{R}^n\\ y'(x,0) &= 0 \text{ in } \mathbb{R}^n. \end{aligned} \tag{4.1.1}$$

Here, κ is the material compressibility, ρ denotes the density and f denotes the amount of absorbed energy, i.e. the imaging parameter that encodes the material properties of physiological interest in PAI. We emphasize that the speed of sound is given by

$c(x) = \frac{1}{\sqrt{\kappa\rho}}$ and that this equation is more general than

$$\begin{aligned} y''(x,t) - c^2(x)\Delta y(x,t) &= 0 \text{ in } \mathbb{R}^n \times (0,\infty) \\ y(x,0) &= f(x) \text{ in } \mathbb{R}^n \\ y'(x,0) &= 0 \text{ in } \mathbb{R}^n, \end{aligned} \tag{4.1.2}$$

which also describes acoustic wave propagation in the case of variable sound speed. The latter equation is derived from (4.1.1) under the additional assumption that ρ is spatially slowly varying. For further details on the derivation of (4.1.1) from fluid- and thermodynamics, we refer to [CK92, Chapter 8.1].

The *photoacoustic reconstruction* consists in determining the function f from measurement data m of y on a surface $S \subseteq \partial\Omega$ over time $(0,T)$.

There exists a huge amount of literature on reconstruction formulas in the case $c \equiv 1$, see for instance [XXW02; XW02; XXW03; XW05; KK08; Kuc14] to name but a few. Time reversal in the case of variable sound speed has been studied for instance in [AK07; HKN08; SU09; Qia+11; Tre+11; Hua+12]. Time reversal for photoacoustic imaging based on (4.1.1) as well as on (4.1.2) has been given in [SU09] - note that both associated wave operators are special cases of the general operator from [SU09]. Their theory has been generalized to the elastic wave equation in [Tit12].

In this paper we focus on numerical realization and regularization theory of photoacoustic imaging based on (4.1.1) with different numerical methods. Most closely related to our numerical approach is a time reversal algorithm from [TC10], which employs the formula (4.3.7) below. Recently we applied iterative regularization techniques in the case of variable sound speed [BGS15a] and compared it with time reversal. The goal here is to generalize time reversal and iterative regularization for photoacoustic imaging in the case of spatially variable density and compressibility. A convergence in the least-squares-sense is thereby guaranteed by standard results from regularization theory (see e.g. [Gro84; EHN96]).

The paper is organized as follows: In Section 4.2 we analyze the mathematical equations describing wave propagation in the case of spatially variable compressibility and density. Imaging based on this model is analyzed in Section 4.3. Numerical results are presented for three different methods; Time reversal, Neumann series, and Landweber iteration in Section 5.9. The latter two seem to be new for the presented equation. We also investigate the case of partial measurement data.

4.1.1 Notation

In the beginning we summarize the basic notation, which is used throughout the paper.

Ω denotes a non-empty, open, bounded and connected domain in $\mathbb{R}^n$ with Lipschitz and piecewise C^1-boundary $\partial\Omega$. Moreover, $S \subseteq \partial\Omega$ is connected and relatively open. The vector $\boldsymbol{n}(x)$, with $x \in \partial\Omega$, denotes the outward pointing unit normal vector of Ω. The absorption density f, the compressibility κ and the density ρ are supposed to satisfy:

- $\kappa, \rho \in C^1(\mathbb{R}^n)$, satisfying $0 < \rho_{\min} \leq \rho(x) \leq \rho_{\max}$, $0 < \kappa_{\min} \leq \kappa(x) \leq \kappa_{\max}$. We also define $c_{\max} := (\kappa_{\min}\rho_{\min})^{-1/2}$. Moreover, we assume that κ, ρ are constant in $\mathcal{C}\Omega$ and satisfy $\kappa\rho = 1$ there.
- The absorption density function f has support in Ω: $\operatorname{supp}(f) \subseteq \Omega$.

For the sake of simplicity of notation we omit space and time arguments of functions whenever this is convenient and does not lead to confusions.

We use the following Hilbert spaces:

- We denote by $L^2(\Omega) = \{\phi \in L^2(\mathbb{R}^n) : \phi \equiv 0 \text{ in } \mathcal{C}\Omega\}$, where $\mathcal{C}\Omega$ denotes the complement of Ω, with inner product

$$\langle \phi_1, \phi_2 \rangle_{L^2(\Omega)} = \int_{\mathbf{R}^n} \phi_1 \phi_2 \partial x.$$

- For $\hat{\Omega} = \Omega$ or $\mathbb{R}^n$:
  - Let $H_0^1(\hat{\Omega})$ be the closure of differentiable functions on $\mathbb{R}^n$ with compact support in $\hat{\Omega}$, associated with the non-standard (but equivalent) inner product

$$\langle \phi_1, \phi_2 \rangle_{1;\kappa,\rho} = \int_{\mathbf{R}^n} \kappa \phi_1 \phi_2 + \rho^{-1} \nabla \phi_1 \cdot \nabla \phi_2 \partial x. \tag{4.1.3}$$

    The associated norm is denoted by $\|\phi\|_{1;\kappa,\rho}$.
  - The seminorm associated to the inner product

$$\langle \phi_1, \phi_2 \rangle_{1;\rho} = \int_{\mathbb{R}^n} \rho^{-1} \nabla \phi_1 \cdot \nabla \phi_2 dx \tag{4.1.4}$$

    is denoted by $|\phi|_{1;\rho}$.
  - The norm associated with the inner product

$$\langle \phi_1, \phi_2 \rangle_1 = \int_{\hat{\Omega}} \phi_1 \phi_2 + \nabla \phi_1 \cdot \nabla \phi_2 \partial x$$

    is denoted by $\|\phi\|_1$.
  - The norms $\|\phi\|_1$ and $\|\phi\|_{1;\kappa,\rho}$ are equivalent. In fact, we have

$$\sqrt{\min\left\{\kappa_{\min}, \rho_{\max}^{-1}\right\}} \|\phi\|_1 \leq \|\phi\|_{1;\kappa,\rho} \leq \sqrt{\max\left\{\kappa_{\max}, \rho_{\min}^{-1}\right\}} \|\phi\|_1 , \quad \text{for all } \phi \in H_0^1(\hat{\Omega}). \tag{4.1.5}$$

- $L^2(S)$ denotes the standard Hilbert space of square integrable functions on $\partial\Omega$ with support in S, together with the inner product

$$\langle \phi_1, \phi_2 \rangle_{L^2(S)} = \int_S \phi_1(x) \phi_2(x) \partial S(x).$$

  $L^2(\Sigma)$ denotes the standard Hilbert space of square integrable functions on $\partial\Omega \times (0,T)$ with support in $\Sigma := S \times (0,T)$, together with the inner product

$$\langle \phi_1, \phi_2 \rangle_{L^2(\Sigma)} = \int_0^T \int_S \phi_1(x,t) \phi_2(x,t) \partial S(x) dt.$$

  The induced norms are denoted by $\|\cdot\|_{L^2(S)}$, $\|\cdot\|_{L^2(\Sigma)}$.

  $C_0^\infty(\Sigma)$ denotes the space of smooth functions with support in Σ.

- The trace operator $\gamma_\Omega : H^1(\mathbb{R}^n) \to L^2(\partial\Omega)$ restricts functions defined on $\mathbb{R}^n$ onto $\partial\Omega$, respectively. This operator is the composition of the standard trace operator $\gamma : H^1(\Omega) \to L^2(\partial\Omega)$ and the restriction operator $R : H^1(\mathbb{R}^n) \to H^1(\Omega)$, which are both bounded [Ada75, Theorem 5.22], and thus itself bounded. We denote

$$\mathcal{C}_\gamma := \|\gamma \circ R\|. \tag{4.1.6}$$

4.2 Direct Problem of Wave Propagation

In this section we are analyzing the *wave operator* L mapping the absorption density f onto the solution y of (4.1.1) restricted to Σ:

$$L : H_0^1(\Omega) \to L^2(\Sigma), \quad f \mapsto y|_\Sigma. \tag{4.2.1}$$

First, we show that the operator L is bounded. Analogous to [BGS15a], we define the total wave energy by

$$E(t;y) := \frac{1}{2}\int_{\mathbf{R}^n} \kappa y'^2 + \rho^{-1}|\nabla y|^2 \,\partial x. \tag{4.2.2}$$

The time derivative of E, taking into account (4.1.1), is

$$E'(t;y) = \int_{\mathbf{R}^n} \kappa y'' y' - \nabla \cdot \left(\rho^{-1}\nabla y\right) y' \partial x = 0 \text{ for all } t > 0.$$

Consequently,

$$E(t;y) = E(0;y) = \frac{1}{2}|f|^2_{1;\rho} \text{ for all } t > 0. \tag{4.2.3}$$

This, together with (4.2.2) shows that

$$\int_{\mathbf{R}^n} \kappa y'^2 \partial x \le |f|^2_{1;\rho} \text{ and } |y(t)|_{1;\rho} \le |f|_{1;\rho} \text{ for all } t > 0. \tag{4.2.4}$$

A-priori this inequality does not provide a bound for y in the whole $\mathbb{R}^n$ with respect to the standard H^1-norm. This is provided for instance by the following lemma:

Lemma 4.2.1 *Let y be the solution of (4.1.1), then*

$$\|y(t)\|_{1;\kappa,\rho} \le \mathcal{C}(T)\,\|f\|_{1;\kappa,\rho}, \qquad \text{for all } t \in (0,T), \tag{4.2.5}$$

where

$$\mathcal{C}(T) := \sqrt{\max\{1+2T^2, 2\}}.$$

Proof: For arbitrary $\hat{t} \in (0,T)$ it follows from (4.2.4) that:

$$\begin{aligned}&\int_{\mathbf{R}^n} \kappa(x)(y(x,t)-y(x,0))^2 \partial x = \int_{\mathbf{R}^n} \kappa(x)\left(\int_0^{\hat{t}} y'(x,\hat{t})d\hat{t}\right)^2 \partial x \\ \le &\hat{t}\int_0^t \int_{\mathbf{R}^n} \kappa y'^2 \partial x d\hat{t} \le T^2 |f|^2_{1;\rho}.\end{aligned}$$

With the elementary inequality $(a-b)^2 \geq \frac{1}{2}a^2 - b^2$ it follows that

$$\begin{aligned}
&\int_{\mathbf{R}^n} \kappa(x)(y(x,t))^2 \partial x \\
\leq & 2\int_{\mathbf{R}^n} \kappa(x)(y(x,t)-y(x,0))^2 \partial x + 2\int_{\mathbf{R}^n} \kappa(x)(y(x,0))^2 \partial x \\
\leq & 2T^2 |f|^2_{1;\rho} + 2\left\|\sqrt{\kappa} f\right\|^2_{L^2(\mathbb{R}^n)}.
\end{aligned}$$

This, together with (4.2.4) shows the assertion. □

Now, we prove boundedness of L:

Theorem 4.2.2 *The operator $L : H_0^1(\Omega) \to L^2(\Sigma)$ is bounded and*

$$\|L\| \leq \frac{\mathcal{C}_\gamma \mathcal{C}(T)\sqrt{T}}{\sqrt{\min\left\{\kappa_{\min}, \rho_{\max}^{-1}\right\}}}. \tag{4.2.6}$$

Proof: For given f let y be the solution of (4.1.1). From (4.2.2) it follows that the solution y of (4.2.5) is in $H^1(\mathbb{R}^n)$ for every $t > 0$. Thus from (4.1.6) and (4.2.5) it follows that

$$\|y\|^2_{L^2(\Sigma)} = \int_0^T \int_{\partial\Omega} y^2(t) dS(x) dt \leq \mathcal{C}_\gamma^2 \int_0^T \|y(t)\|_1^2 dt \leq \frac{\mathcal{C}_\gamma^2 \mathcal{C}(T)^2 T \|f\|^2_{1;\kappa,\rho}}{\min\left\{\kappa_{\min}, \rho_{\max}^{-1}\right\}}.$$

□

Remark 4.2.3: From [Tat98, Theorem 1] it follows that the trace $L[f]$ is in fact in $H^{3/4}_{loc}(\partial\Omega \times (0,T))$. Therefore, by finite speed of propagation (Theorem 4.2.8), if we in addition assume that f is supported away from $\partial\Omega$, $L[f]$ is in fact in $H^{3/4}(\partial\Omega \times (0,T))$. The proof does not follow in a straightforward way from standard trace results, but utilizes the theory of Fourier integral operators and microlocal analysis. In special cases, this result can be further improved, see [SU09, Remark 5] and also [BS91; BS93]. For instance, for Ω strictly convex, we have $L[f] \in H^1(\partial\Omega \times (0,T))$. As a consequence, $L : H_0^1(\Omega) \to L^2(\Sigma)$ is compact, because it is a composition of bounded and a compact operator, using the fact that the embedding from $H^1(\partial\Omega \times (0,T))$ to $L^2(\partial\Omega \times (0,T))$ is compact (see e.g. [Aub82, Theorem 2.34]).

In the following we characterize the adjoint of $L : H_0^1(\Omega) \to L^2(\Sigma)$ on a dense subset of $L^2(\Sigma)$. Since $L^* : L^2(\Sigma) \to H_0^1(\Omega)$ is bounded (in fact, $\|L\| = \|L^*\|$), a characterization follows by limits of convergent sequences on dense subsets. Here we characterize L^* on $C_0^\infty(\Sigma)$ first and extend it by convergent sequences to $L^2(\Sigma)$.

Definition 4.2.4 Let i be the embedding operator from $H_0^1(\Omega)$ to $L^2(\Omega)$. Then $i^* : L^2(\Omega) \to H_0^1(\Omega)$ is the operator which maps a function $\psi \in L^2(\Omega)$ onto the solution of the equation

$$Du = \psi \text{ in } \Omega, \qquad u = 0 \text{ on } \partial\Omega, \tag{4.2.7}$$

with $D := \kappa - \nabla \cdot \rho^{-1} \nabla$. In other words $i^* = D^{-1}$.

In the following we derive the adjoint L^* of the operator L, which is required for the implementation of the Landweber iteration below, on a dense subset of $L^2(\Sigma)$. The boundedness of L^* is guaranteed by elementary Hilbert space theory. Therefore, we get a characterization on $L^2(\Sigma)$ by limits of convergent sequences.

Theorem 4.2.5 *For $h \in C_0^\infty(\Sigma)$ the adjoint of the operator L, defined in Equation 4.2.1, is given by*

$$L^*[h] = i^* \circ L_D^*[h] \tag{4.2.8}$$

where

$$L_D^*[h] = \kappa z'(0)|_\Omega, \tag{4.2.9}$$

and $z := z(h)$ is the weak solution of

$$\begin{aligned} \kappa z'' - \nabla \cdot (\rho^{-1} \nabla z) &= 0 \text{ in } \mathbb{R}^n \backslash \partial\Omega \times (0,T), \\ z(T) = z'(T) &= 0 \text{ in } \mathbb{R}^n, \\ [z] = 0, \quad \left[\frac{\partial z}{\partial \boldsymbol{n}}\right] &= h \text{ on } \Sigma, \\ [z] = 0, \quad \left[\frac{\partial z}{\partial \boldsymbol{n}}\right] &= 0 \text{ on } \partial\Omega \setminus \Sigma \times (0,T). \end{aligned} \tag{4.2.10}$$

Here

$$[z] := z^+|_\Sigma - z^-|_\Sigma \text{ and } \left[\frac{\partial z}{\partial \boldsymbol{n}}\right] := \left.\frac{\partial z^+}{\partial \boldsymbol{n}}\right|_\Sigma - \left.\frac{\partial z^-}{\partial \boldsymbol{n}}\right|_\Sigma$$

where $z^+ := z|_{\mathcal{C}\Omega \times (0,T)}$ and $z^- := z|_{\Omega \times (0,T)}$.

Proof: The existence of a weak solution of (4.2.10) is analogous to [BGS15a, Appendix A], where the transmission problem has been studied for variable sound speed. Multiplying the first equation of (4.2.10) by the solution of (4.1.1) y, it follows that $h \in C_0^\infty(\Sigma)$:

$$\begin{aligned} &\int_\Sigma hL[f] \partial S(x) dt = \int_\Sigma hy \partial S(x) dt = \int_\Omega \kappa z'(0) f \partial x \\ &= \int_\Omega D\left[D^{-1}\left[\kappa z'(0)\right]\right] f \partial x = \left\langle i^*\left[\kappa z'(0)\right], f \right\rangle_{1;\kappa,\rho}. \end{aligned} \tag{4.2.11}$$

□

The following results on finite speed of propagation of the solution of (4.1.1) are based on the results from [Eva10].

Definition 4.2.6 Let $\mathtt{d}(x) := \operatorname{dist}(x_0, x)$ be the distance between x_0 and x with respect to the Riemannian metric $\kappa\rho\partial x$. Note that this metric is chosen in accordance with the principal symbol of the elliptic operator

$$-\kappa^{-1} \nabla \cdot \left(\rho^{-1} \nabla \cdot\right).$$

The cone $\mathcal{K}$ with respect to the space-time point (t_0, x_0) is defined as

$$\mathcal{K} := \{(x,t) : \mathtt{d}(x) < t_0 - t\}.$$

we further introduce

$$\mathcal{K}_t := \{x : \mathtt{d}(x) < t_0 - t\},$$

the cross-section of $\mathcal{K}$ at fixed time t.

Remark 4.2.7: According to [Eva10, pp. 416] the function $\mathtt{d}$ *solves the PDE*

$$\frac{1}{\rho\kappa}|\nabla \mathtt{d}|^2 = 1, \quad \mathtt{d}(x_0) = 0. \tag{4.2.12}$$

This relation will be used in the proof of Theorem 4.2.8 below.

Theorem 4.2.8 *Let y be the solution of (4.1.1). Assume $y' \equiv 0$ on $\mathcal{K}_0$, then $y \equiv 0$ in $\mathcal{K}$.*

Proof: Let

$$E_{\mathcal{K}_t}(t; y) := \frac{1}{2}\int_{\mathcal{K}_t} \kappa y'^2 + \rho^{-1}|\nabla y|^2 \partial x \tag{4.2.13}$$

denote the local energy. Taking the time derivative of $E_{\mathcal{K}_t}$, it follows by application of the Leibniz rule for the differentiation of evolving region integrals [Eva10, p.713] that

$$E'_{\mathcal{K}_t}(t; y) = \int_{\mathcal{K}_t} \kappa y' y'' + \rho^{-1}\nabla y \cdot \nabla y' \partial y + \frac{1}{2}\int_{\partial\mathcal{K}_t} \left(\kappa y'^2 + \rho^{-1}|\nabla y|^2\right) \boldsymbol{v}\cdot\boldsymbol{n}\partial S(x),$$

where $\boldsymbol{v}$ denotes the normal velocity of the moving boundary ∂C_t and $\boldsymbol{n}$ is the outward pointing unit normal to $\mathcal{K}_t$. For a fixed point $x \in \mathcal{K}_t$, we have $\boldsymbol{v}(x) = \frac{\nabla \mathtt{d}(\mathtt{x})}{|\nabla \mathtt{d}(\mathtt{x})|^2}$ and $\boldsymbol{n}(x) = -\frac{\nabla \mathtt{d}(\mathtt{x})}{|\nabla \mathtt{d}(\mathtt{x})|}$. Therefore,

$$\begin{aligned} E'_{\mathcal{K}_t}(t; y) = &\int_{\mathcal{K}_t} \kappa y' y'' + \rho^{-1}\nabla y \cdot \nabla y' \partial y \\ &- \frac{1}{2}\int_{\partial\mathcal{K}_t} \left(\kappa y'^2 + \rho^{-1}|\nabla y|^2\right) \frac{1}{|\nabla \mathtt{d}|}\partial S(x) =: A - B\,. \end{aligned} \tag{4.2.14}$$

By application of Green's formula, A is rewritten to

$$A = \int_{\mathcal{K}_t} y'\left(\kappa y'' - \nabla\cdot\left(\rho^{-1}\nabla y\right)\right) dx + \int_{\partial\mathcal{K}_t} \rho^{-1} y' \nabla y \cdot \frac{\nabla \mathtt{d}}{|\nabla \mathtt{d}|}\partial S(x).$$

The first term vanishes since y is solution to (4.1.1) and thus from (4.2.12) it follows that

$$|A| \le \int_{\partial\mathcal{K}_t} \frac{|y'|\rho^{-1/2}|\nabla \mathtt{d}||\nabla y|\rho^{-1/2}}{|\nabla \mathtt{d}|}\partial S(x) = \int_{\partial\mathcal{K}_t} \frac{|y'|\kappa^{1/2}|\nabla y|\rho^{-1/2}}{|\nabla \mathtt{d}|}\partial S(x)\,.$$

Using Cauchy's inequality, we finally obtain

$$|A| \le \frac{1}{2}\int_{\partial\mathcal{K}_t} \left(\kappa y'^2 + \rho^{-1}|\nabla y|^2\right) \frac{1}{|\nabla \mathtt{d}|}\partial S(x) = B\,.$$

Thus, from (4.2.14) it follows that $E'_{\mathcal{K}_t}(t; y) \le 0$. □

4.3 Photoacoustic Imaging

The *photoacoustic imaging problem* can be expressed as the solution of the operator equation:

$$L[f] = m. \tag{4.3.1}$$

Uniqueness of the solution of (4.3.1) is closely related to a unique continuation result for the wave equation:

Theorem 4.3.1 (Unique Continuation [Rob91; HÖ92; Tat95]) *Let u be a solution to (4.1.1), and $y \equiv 0$ in $(-T,T) \times B_\varepsilon(x_0)$. Then*

$$y \equiv 0 \text{ in } \{(x,t) \in \mathbb{R} \times \mathbb{R}^n : \operatorname{dist}(x,x_0) \leq T - |t|\} .$$

Uniqueness of the solution of (4.3.1) requires a sufficiently large observation time

$$T_0 := \max_{x \in \operatorname{supp} f} \operatorname{dist}(x,S), \tag{4.3.2}$$

where $\operatorname{dist}(x,S)$ is the distance of x to the closest point $x' \in S$ with respect to the Riemannian metric $\kappa\rho\partial x$.

Corollary 4.3.2 (Injectivity of L [SU09]) *Let Ω be strictly convex and $T > T_0$. Moreover, let $\operatorname{supp} f \subset \Omega$. Then $L[f] = 0$ implies $f = 0$.*

In the following we discuss several numerical algorithms for solving (4.3.1).

4.3.1 Landweber Iteration

We are employing the Landweber's iteration for solving (4.3.1) and compare it with the time reversal methods presented in Subsection 4.3.2, which are the standard references in this field. More efficient iterative regularization algorithms are at hand [Han95], but these are less intuitive to be compared with time reversal. The Landweber algorithm reads as follows:

$$f_0 := 0 \quad \text{and} \quad f_k^\delta = f_{k-1}^\delta - \omega L^*[L[f_{k-1}^\delta] - m^\delta], \quad k = 1,2,\ldots, \tag{4.3.3}$$

where m^δ stands for error-prone data with $\left\| m^\delta - m \right\|_{L^2(\Sigma)} < \delta$, where $m = y|_\Sigma$. For a summary of results for Landweber regularization in Photoacoustics we refer to [BGS15a] and the references therein.

We emphasize that Landweber's iteration converges to the *minimum norm solution*

$$f^\dagger = L^\dagger[m], \tag{4.3.4}$$

where $L^\dagger$ is the Moore-Penrose inverse (see [Nas76] for a survey), if the data m is an element of the range of L. This is a property which is relevant when the observation time T is smaller than the critical time T_0 which guarantees injectivity of L.

4.3.2 Time Reversal

In this subsection, we first state the conventional time reversal and give a remark on necessary assumptions to obtain error estimates for this method. This is followed by a description of a modified time reversal approach, for which a theoretical analysis based on [SU09] can be provided.

Conventional Time Reversal

We formally define the time reversal operator:

$$\overline{L}[h] = z(\cdot, 0), \tag{4.3.5}$$

where z is a solution of

$$\begin{aligned} \kappa z'' - \nabla \cdot (\rho^{-1} \nabla z) &= 0 \text{ in } \Omega \times (0,T), \\ z(T) = z'(T) &= 0 \text{ in } \Omega, \\ z &= h \text{ on } \partial\Omega \times (0,T), \end{aligned} \tag{4.3.6}$$

The fundamental difference between $\overline{L}$ and L^* is that they are defined via differential equations on $\Omega \times (0,T)$ and $\mathbb{R}^n \times (0,T)$. The conventional time reversal reconstruction [TC10] consists of computing

$$f_{\mathrm{TR}} = \overline{L}[m]\,. \tag{4.3.7}$$

Remark 4.3.3: Assume that $S = \partial\Omega$, that $\rho \equiv 1$ and the speed of sound is non-trapping. For this case, Hristova [Hri09, Theorem 2] provides an error estimate for the time reversal method, employing results on the decay of solutions of the wave equation (e.g. [Vai75]).

Neumann Series

Stefanov and Uhlmann [SU09] define the modified time reversal for (4.1.1): Rather than assuming (in most cases unjustified) the initial data $z(T) \equiv 0$ we are again using the harmonic extension of the data term $h(s,T)$, for $s \in \partial\Omega$, as initial datum at T. That is, for

$$-\nabla \cdot (\rho^{-1} \nabla \phi) = 0 \text{ in } \Omega, \text{ with } \phi(\cdot) = m(\cdot, T) \text{ on } \partial\Omega$$

the modified time reversal operator

$$\widetilde{\overline{L}}[h] = z(\cdot, 0) \tag{4.3.8}$$

is defined by the solution of equation

$$\begin{aligned} \kappa z'' - \nabla \cdot (\rho^{-1} z) &= 0 \text{ in } \Omega \times (0,T), \\ z(T) = \phi, \quad z'(T) &= 0 \text{ in } \Omega, \\ z &= h \text{ on } \partial\Omega \times (0,T). \end{aligned} \tag{4.3.9}$$

Note that this algorithm has not been used as a basis for numerical reconstruction for the generalized (4.1.1).

Previously [SU09] showed stability of the modified time reversal reconstruction under non-trapping conditions and for sufficiently large measurement time for (4.1.2). In fact,

let $c=(\kappa\rho)^{-1/2}$ be non-trapping [HKN08] and T_1 denote the time when all singularities have left $\overline{\Omega}$. Then the result is directly convertible to (4.1.1):

Theorem 4.3.4 (Stability of Modified Time Reversal) *[SU09, Theorem 1] Let $T>T_1$ and $S=\partial\Omega$ be a closed C^2-surface. Moreover, let the coefficients κ, $\rho\in C^\infty(\mathbb{R}^n)$.*

Then $\widetilde{\widetilde{L}}L=Id-K$, where K is a compact operator from $H_0^1(\Omega)\to H_0^1(\Omega)$ satisfying $\|K\|<1$.

Note that [SU09, Theorem 1] works only for complete boundary measurement data.

By Theorem 4.3.4, the initial value f can be expanded into the Neumann series

$$f=\sum_{j=0}^{\infty}K^j[m]. \tag{4.3.10}$$

By induction one sees that the m-th iterate can be written as

$$f_k=f_{k-1}-\widetilde{\widetilde{L}}[L[f_{k-1}]-m], \tag{4.3.11}$$

where

$$f_k=\sum_{j=0}^{k}K^j[m].$$

Remark 4.3.5: Note that with partial data, the Neumann series reconstruction consists in formally applying (4.3.10) to the extended data m_s, where

$$m_s=m \text{ in } \Sigma'\subset\subset\Sigma \text{ and } m_s=0 \text{ in } \partial\Omega\setminus\Sigma\times(0,T), \tag{4.3.12}$$

in a way that $m_s\in H^1(\partial\Omega\times[0,T])$ serves as approximation to m in Σ.

Let now $S\subset\partial\Omega$ relatively open. To fix the terminology, we define for $(x,\xi)\in\mathbb{R}^n\times\mathbb{S}^{n-1}$ the curve

$$\gamma_{(x,\xi)}(\tau)$$

to be the geodesic (in the Riemannian metric $\kappa\rho\partial x$) through x in direction ξ, where $\tau\in(-\infty,\infty)$ and $\gamma_{(x,\xi)}(0)=x$. Note that

$$\tau_\pm(x,\xi)=\max\left\{\tau\geq 0:\gamma_{(x,\xi)}(\pm\tau)\in\overline{\Omega}\right\}.$$

give the (possibly infinite) times when the geodesics leave the domain in positive ($\mathrm{sgn}=+$) resp. negative ($\mathrm{sgn}=-$) direction. Regarding stability [SU09, Theorem 3] provides the following result, which holds also in the partial data case.

Theorem 4.3.6 *Assume that*

$$(\tau_{sgn}(x,\xi),\gamma_{(x,\xi)}(\tau_{sgn}(x,\xi))\in\Sigma$$

holds for all $(x,\xi)\in\Omega_1\times\mathbb{S}^{n-1}$ in at least one of the two directions $\mathrm{sgn}=+$, $\mathrm{sgn}=-$. Then there exists a constant $C>0$ such that for any $f\in C_0^\infty(\Omega_1)$, with $\Omega_1\subset\subset\Omega$, the

estimate

$$\|f\|_{H_0^1(\Omega_1)} \leq C \|Lf\|_{H^1(\Sigma)}$$

is valid.

4.4 Numerical Experiments and Results

We compare conventional time reversal (4.3.7), the Neumann series approach (4.3.11) and the Landweber iteration (4.3.3) for the photoacoustic imaging problem based on (4.1.1). Similar studies have been performed in [BGS15a] for photoacoustic imaging based on (4.1.2). Figure 4.1 displays the involved parameters, including absorption density f, material compressibility κ and density ρ.

For the numerical solution of the involved wave equations (4.1.1) and (4.2.10), we use a straight-forward adaptation of the BEM-FEM scheme outlined in [BGS15a]. (4.3.6) and (4.3.9) are discretized by finite element discretization.

For the simulation of the data, for all different wave equations, the mesh size has been chosen as $\Delta x = 0.0095$ and $\Delta t = \Delta x/(15 * c_{\max})$, leading to about 40000 nodal points in Ω. For all wave equations involved in reconstruction, we use a grid with $\Delta x_R = 0.01$ and $\Delta t_R = \Delta x_R/(15 * c_{\max})$.

Measurement data are assumed to be recorded on 630 detection points on the unit circle. In the partial data example, the measurements are restricted to the lower half of the circle.

The total measurement time was varied as multiples of T_0, which is defined as in (4.3.2).

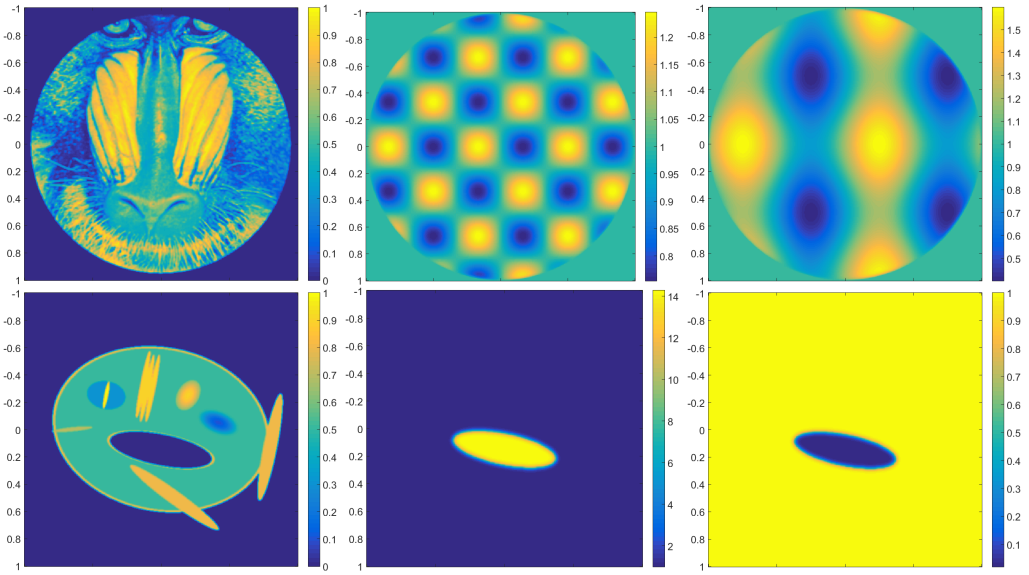

FIGURE 4.1: Parameters: **First line:** Test Example 1 – *Mandrill*. **Second line:** Test example 2 – *Fish*. **From left to right:** Initial pressure f, compressibility κ, density ρ.

4.4.1 Test Example 1 – *Mandrill*

We investigate the performance of the different photoacoustic imaging techniques, time reversal, Neumann series and Landweber iteration, respectively, with spatially varying κ and ρ. We show different test cases

a for partial measurement data (see Figure 4.2), where we show the imaging results for $T = 2T_0$ and $T = 4T_0$, where T_0, defined in (4.3.2) denotes the minimal time that guarantees unique reconstruction of the absorption density f

b as well as reconstructions from full data in the presence of noise (Figure 4.3). The noise level is stated as SNR (signal to noise ratio, in dB scale) with respect to the maximum signal value. The examples include moderate noise (SNR = 10dB) and high noise (SNR = 5dB).

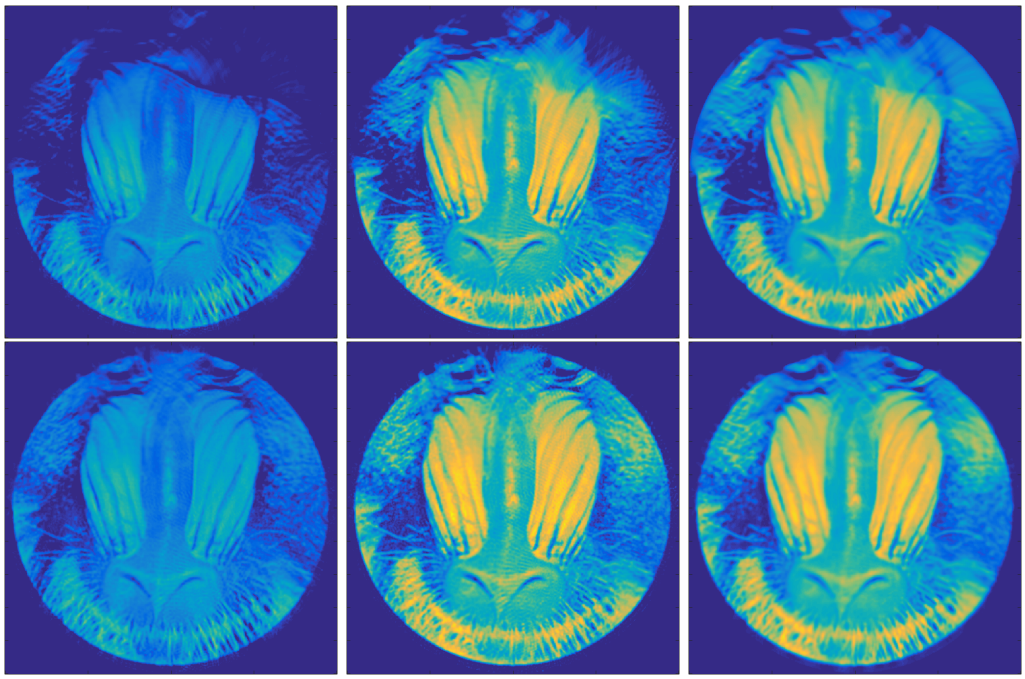

FIGURE 4.2: Partial data reconstructions: Data are recorded on the lower unit half-circle and the parameters κ, ρ are exactly given. Data are noise free and recorded for $T = 2T_0$, $4T_0$. Reconstructions for $T = 2T_0$, $4T_0$ are shown in the first and second line, respectively. **From left to right:** Time reversal, Neumann series with $k = 5$, Landweber iterate $k = 5$.

4.4.2 Test Example 2 – *Fish*

The second test concerns a parameter setting κ, ρ and associated sound speed $c = (\kappa\rho)^{-1/2}$, which is reconstructed with inversions (time reversal, Neumann series, Landweber iteration) based on (4.1.2).

The phantom simulates a water-like body (like, e.g., soft tissue) containing an inclusion with significantly different acoustic properties, like the air-filled swim-bladder

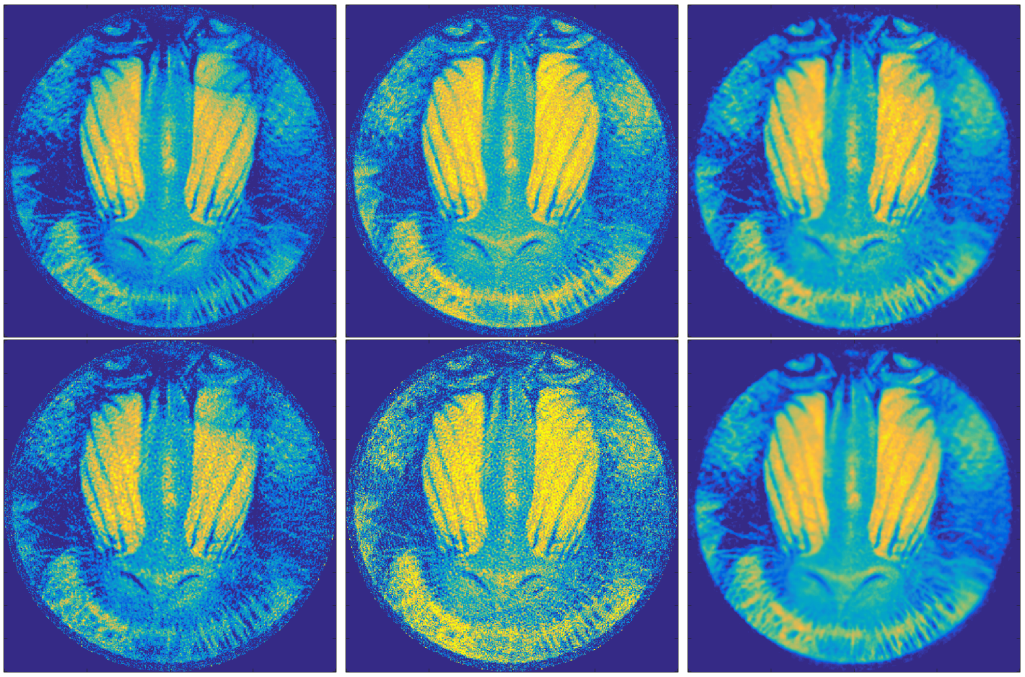

FIGURE 4.3: Reconstruction with complete, but noisy measurements and correct parameters κ, ρ, measurement time $T = 2T_0$. **First line**: SNR = 10dB. **Second line**: SNR = 5dB. **From left to right:** Time reversal, Neumann series with $k = 5$, Landweber iterate $k = 5$.

of a fish (see lower line of Figure 4.1). We choose the parameters to be bounded in the intervals $0.02 \leq \rho \leq 1$ and $1 \leq \kappa \leq 14.3$, with high gradients in the transition between the inclusion and the rest of the domain (see also Figure 4.1).

Moreover, we include the achievable results when only $c = (\kappa\rho)^{-1/2}$ is known, leading to a modeling error in the reconstructions.

a In the first line of Figure 4.4 we display the reconstructions with correct parameters κ, ρ as depicted in the second line of Figure 4.1.

b Next, reconstructions are performed by using the parameters $\kappa_1 = \kappa\rho$ and $\rho_1 = 1$. This displays the usually considered approximation (see second line of Figure 4.4).

c We also try it the other way round by setting $\rho_2 = \kappa\rho$, and $\kappa_2 \equiv 1$ (third line of Figure 4.4). This leads to the wave equation in pure divergence form, and displays the case where the compressibility variations are negligible.

However, in b and c the modeling error leads to severe artifacts near regions of high-gradient regions of the parameters.

4.4.3 Results

In the presented test examples, all three methods qualitatively reconstruct the same features. Time reversal however fails to give a quantitatively correct results, due to the relatively short measurement times in use. Neumann series and Landweber iteration

perform at the same level. As expected from theory, the Landweber reconstructions appear slightly smoother, specifically in Figure 4.3.

The second test clearly indicates that a modeling error in the reconstruction method can lead to severe artifacts near regions where the parameter gradients are large.

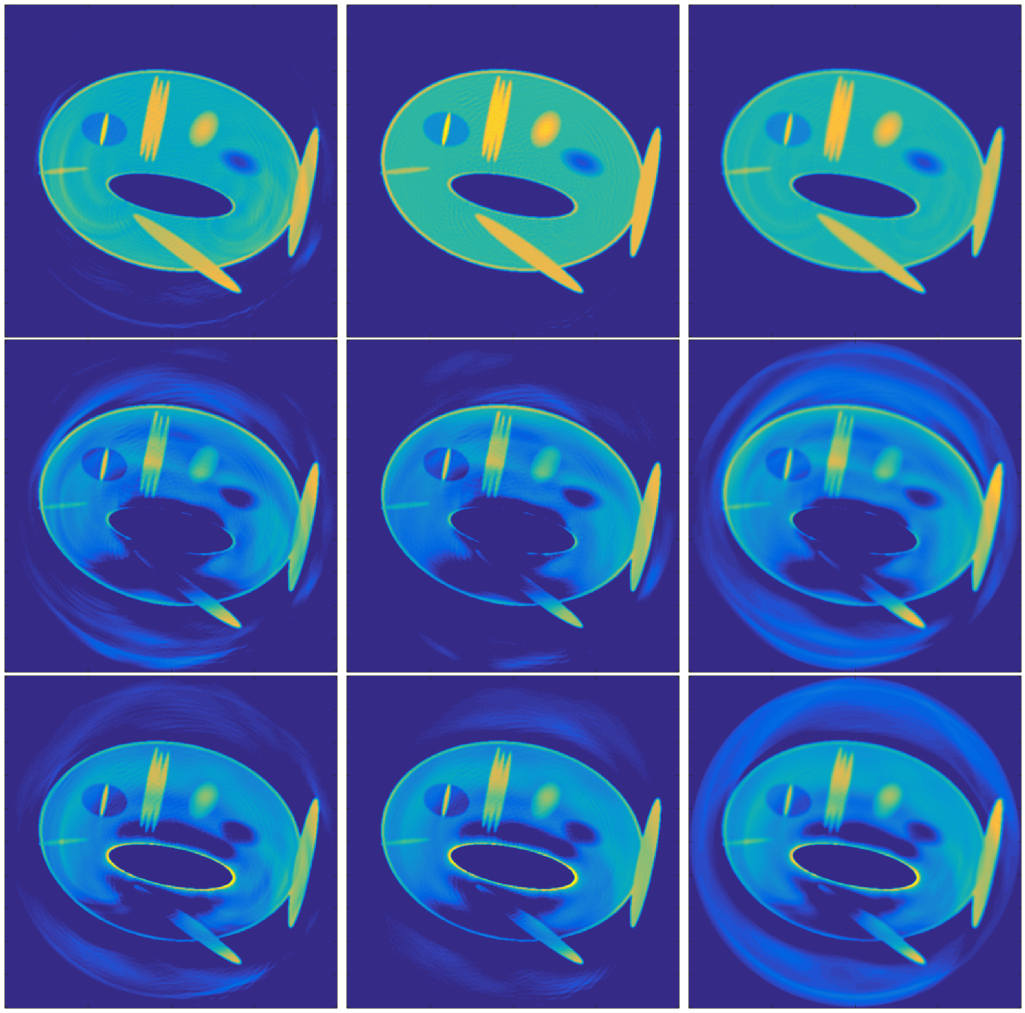

FIGURE 4.4: Reconstructions of the *Fish* phantom with $T = 2T_0$. **First line**: Reconstruction using correct parameters $\kappa_1 = \kappa$, $\rho_1 = \rho$ as pictured in the second line of Figure 4.1. **Second line**: Reconstruction with parameters $\kappa_1 = \kappa\rho$, $\rho_1 \equiv 1$. **Third line**: Reconstruction with parameters $\rho_1 = \kappa\rho$, $\kappa_1 \equiv 1$. **From left to right:** Time reversal, Neumann series with $k = 5$, Landweber iterate $k = 5$.

4.5 Conclusions

In this work we have studied photoacoustic imaging based on a general wave model with spatially variable compressibility and density, respectively. We have implemented Neumann series and Landweber iteration for photoacoustic imaging based on this general equation and we compared the result to conventional time reversal as discussed in [TC10].

The numercial methods for photoacoustic imaging reveal the differences as outlined in Table 4.1 with respect to convergence, stability and robustness against noise at the present stage of research. Stability is understood in the sense of regularization theory [Gro84], meaning that the Landweber iterates determined by a discrepancy principle approximate the minimum norm solution.

	Time Reversal	**Neumann**	**Landweber**
Convergence:			best approx. sol.
measurement time	$T \to \infty$	$T > T_1$	$T > 0$
sound speed	non-trapping	non-trapping	arbitrary
data	full	full	partial
Stability:			regularized sol.
measurement time	$T > T_1$	$T > T_1/2$	$T > 0$
sound speed	non-trapping	non-trapping	arbitrary
data	full	partial	partial
L^2**-Noise:**	no	no	yes

TABLE 4.1: Overview on the different photoacoustic imaging methods.

Numerical results show the reconstructions in the case of error prone data and under modeling errors. We emphasize that, so far, an error analysis is only possible for the Landweber iteration.

5

Non-equispaced Sampling in Photoacoustics with a Non-uniform FFT

Julian Schmid, Thomas Glatz, Behrooz Zabihian, Mengyang Liu, Wolfgang Drexler and Otmar Scherzer

Abstract

To obtain the initial pressure from the collected data on a planar sensor arrangement in photoacoustic tomography, there exists an exact analytic frequency domain reconstruction formula. An efficient realization of this formula needs to cope with the evaluation of the data's Fourier transform on a non-equispaced mesh. In this paper, we use the non-uniform fast Fourier transform to handle this issue and show its feasibility in 3D experiments with real and synthetic data. This is done in comparison to the standard approach that uses linear, polynomial or nearest neighbor interpolation. Moreover, we investigate the effect and the utility of flexible sensor location to make optimal use of a limited number of sensor points. The computational realization is accomplished by the use of a multi-dimensional non-uniform fast Fourier algorithm, where non-uniform data sampling is performed both in frequency and spatial domain. Examples with synthetic and real data show that both approaches improve image quality.

5.1 Introduction

Photoacoustic tomography is an emerging imaging technique that combines the contrast of optical absorption with the resolution of ultrasound images (see for instance [Wan09]). In experiments an object is irradiated by a short-pulsed laser beam. Depending on the absorption properties of the material, some of the pulse energy is absorbed and converted into heat. This leads to a thermoelastic expansion, which causes a pressure rise, resulting in an ultrasonic wave called photoacoustic signal. The signal is detected by an array of ultrasound transducers outside the object. Using this signal the initial pressure is reconstructed, offering a 3D image proportional to the amount of absorbed energy at each position. This is the imaging parameter of photoacoustics.

Common measurement setups rely on small ultrasound sensors, which are arranged *uniformly* along simple geometries, such as planes, spheres, or cylinders (see for instance [XW02; XFW02; XW03; Wan09; Bea11]).A non-equispaced arrangement of transducers aligned on a spherical array has already been used by [Xia+13]. Here we investigate photoacoustic reconstructions from ultrasound signals recorded at *not necessarily equispaced* positions on a planar surface. In other words, we use an irregular sensor point arrangement, where sensor points are denser towards the center. This is done in order to maximize image quality, when the number of sensor points is a limiting factor. Our

current setup allows to acquire data from 50 sensor points each second. As a consequence, data acquisition of a typical sample requires several minutes. Reducing this acquisition time is a crucial step in advancing photoacoustic tomography towards clinical and preclinical application. This approach can also be seen as new way for dealing with the limited view problem where deficiencies are caused by a small detection region.

For the planar arrangement of point-like detectors there exist several approaches for reconstruction, including numerical algorithms based on filtered back-projection formulas and time-reversal algorithms (see for instance [XFW02; KK08; XW05; XW06]).

The suggested algorithm in the present work realizes a Fourier inversion formula (see (5.2.1) below) using a fast Fourier transform (FFT) method suitable for non-equispaced grid points and frequencies [DR93; Bey95; Ste98]. Such methods have been designed for evaluation of Fourier transforms at non-equispaced points in frequency domain, or non-equispaced data points in spatial, respectively temporal domain. In the present realization introduced in [Fou03], the prior is called NER-NUFFT (non-equispaced range non-uniform FFT), whereas the latter is called NED-NUFFT (non-equispaced data non-uniform FFT). Both NUFFT methods have proven to achieve high accuracy and simultaneously reach the computational efficiency of conventional FFT computations on regular grids [Fou03].

For the reconstruction we propose a novel combination of NED- and NER-NUFFT, which we call NEDNER-NUFFT, based on the following considerations:

1. The discretization of the analytic inversion formula (5.2.1) contains evaluations at non-equidistant sample points in frequency domain.

2. In addition, and this comes from the motivation of this paper, we consider evaluation at non-uniform sampling points.

The first issue can be solved by a NER-NUFFT implementation: For *2D* photoacoustic inversion with *uniformly* placed sensors on a *measurement line*, such an implementation has been considered in [HSZ09a]. Furthermore, this method was used for biological photoacoustic imaging in [Sch+11]. In both papers the imaging was realized in 2D due to the use of integrating line detectors [Bur+05; Pal+09]. In this paper we will analyze the NER-NUFFT in a *3D* imaging setup with point sensors for the first time. The second issue is solved by employing the NED-NUFFT [Fou03]. Thus the name NEDNER-NUFFT for the combined reconstruction algorithm.

The outline of this work is as follows: In Section 5.2 we outline the basics of the Fourier reconstruction approach by presenting the underlying photoacoustic model. We state the Fourier domain reconstruction formula (5.2.1) in a continuous setting. Moreover, we figure out two options for its discretization. We point out the necessity of a fast and accurate algorithm for computing the occurring discrete Fourier transforms with non-uniform sampling points. In Section 5.3 we briefly explain the idea behind the NUFFT. We state the NER-NUFFT (Subsection 5.3.1) and NED-NUFFT (Subsection 5.3.2) formulas in the form we need it to realize the reconstruction on a non-equispaced grid. In Section 5.4 we introduce the *3D* experimental setup.

The sections thereafter describe the realized experiments. In Section 5.5 we compare the NER-NUFFT with conventional FFT reconstruction for synthetic data in 3D. For the real data comparisons we add a time reversal reconstruction. Section 5.6 explains how we choose and implement the non-equispaced sensor placement. In Section 5.7 we

turn to the NEDNER-NUFFT in 2D with simulated data, in order to test different sensor arrangements in an easily controllable environment. In Section 5.8 we interpolate an irregular equi-steradian sensor arrangement data from experimentally acquired data-sets. We apply our NEDNER-NUFFT approach to the non-uniform data and quantitatively compare the reconstructions to regular grid reconstructions. We conclude with a summary of the results in Section 5.9, where we also discuss the benefits and limitations of the presented methods.

5.2 Numerical Realization of a Photoacoustic Inversion Formula

Let $U \subset \mathbb{R}^d$ be an open domain in $\mathbb{R}^d$, and Γ a $d-1$ dimensional hyperplane not intersecting U. Mathematically, photoacoustic imaging consists in solving the operator equation

$$\mathbf{Q}[f] = p|_{\Gamma\times(0,\infty)}\,,$$

where f is a function with compact support in U and $\mathbf{Q}[f]$ is the trace on $\Gamma\times(0,\infty)$ of the solution of the equation

$$\begin{aligned}\partial_{tt}p - \Delta p &= 0 \text{ in } \mathbb{R}^d\times(0,\infty)\,,\\ p(\cdot,0) &= f(\cdot) \text{ in } \mathbb{R}^d\,,\\ \partial_t p(\cdot,0) &= 0 \text{ in } \mathbb{R}^d\,.\end{aligned}$$

In other words, the photoacoustic imaging problem consists in identifying the initial source f from measurement data $g = p|_{\Gamma\times(0,\infty)}$.

An explicit inversion formula for Q in terms of the Fourier transforms of f and $g := \mathbf{Q}[f]$ has been first formulated by [NL81] and introduced to photoacoustics by [Kös+01]. Let $(\boldsymbol{x}, y) \in \mathbb{R}^{d-1}\times\mathbb{R}^+$. Assume without loss of generality (by choice of proper basis) that Γ is the hyperplane described by $y = 0$. Then the reconstruction reads as follows:

$$\mathbf{F}[f](\boldsymbol{K}) = \frac{2K_y}{\kappa(\boldsymbol{K})}\mathbf{F}[\mathbf{Q}f](\boldsymbol{K}_{\boldsymbol{x}}, \kappa(\boldsymbol{K}))\,. \tag{5.2.1}$$

where $\mathbf{F}$ denotes the d-dimensional Fourier transform:

$$\mathbf{F}[f](\boldsymbol{K}) := \frac{1}{(2\pi)^{n/2}}\int_{\mathbb{R}^d} \mathrm{e}^{-\mathrm{i}\boldsymbol{K}\cdot(\boldsymbol{x},y)} f(\boldsymbol{x})\mathrm{d}\boldsymbol{x}\,,$$

and

$$\begin{aligned}\kappa(\boldsymbol{K}) &= \operatorname{sign}(K_y)\sqrt{\boldsymbol{K}_x^2 + K_y^2}\,,\\ \boldsymbol{K} &= (\boldsymbol{K}_x, K_y)\,.\end{aligned}$$

Here, the variables $\boldsymbol{x}, \boldsymbol{K}_{\boldsymbol{x}}$ are in $\mathbb{R}^{d-1}$, whereas $y, K_y \in \mathbb{R}$.

For the numerical realization these three steps have to be realized in discrete form. We hereby largely follow the description in [HSZ09a]. In addition, we give the according formula for the case of measurements taken on non-equispaced grid points.

Lets denote evaluations of a function φ at sampling points $(\boldsymbol{x}_m, y_n) \in (-X/2, X/2)^{d-1} \times (0, Y)$ by

$$\varphi_{m,n} := \varphi(\boldsymbol{x}_m, y_n)\,. \tag{5.2.2}$$

For convenience, we will modify this notation in case of evaluations on an equispaced Cartesian grid. We define the d-dimensional grid

$$\mathbf{G}_x \times \mathrm{G}_y := \{-N_x/2, \dots, N_x/2-1\}^{d-1} \times \{0, \dots, N_y - 1\}\,,$$

and assume our sampling points to be located on $\boldsymbol{m}\Delta_x, n\Delta_y$, where

$$(\boldsymbol{m}, n) \in \mathbf{G}_x \times \mathrm{G}_y\,,$$

and write

$$\varphi_{\boldsymbol{m},n} = \varphi(\boldsymbol{m}\Delta_x, n\Delta_y)\,, \tag{5.2.3}$$

where $\Delta_x := X/N_x$ resp. $\Delta_y := Y/N_y$ are the occurring step sizes.

In frequency domain, we have to sample symmetrically with respect to K_y. Therefore, we also introduce the interval

$$\mathrm{G}_{K_y} := \{-N_y/2, \dots, N_y/2-1\}.$$

Since we will have to deal with evaluations that are partially in-grid, partially not necessarily in-grid, we will also use combinations of (5.2.2) and (5.2.3). In this paper, we will make use of discretizations of the source function f, the data function g and their Fourier transforms $\hat{f}$ resp. $\hat{g}$.

Let in the following

$$\hat{f}_{\boldsymbol{j},l} = \sum_{(\boldsymbol{m},n) \in \mathbf{G}_x \times \mathrm{G}_y} f_{\boldsymbol{m},n} \mathrm{e}^{-2\pi \mathrm{i}(\boldsymbol{j}\cdot\boldsymbol{m} + ln)/(N_x^{d-1} N_y)}$$

denote the d-dimensional discrete Fourier transform with respect to space and time. By discretizing formula (5.2.1) via Riemann sums it follows

$$\begin{aligned} \hat{f}_{\boldsymbol{j},l} \approx \frac{2l}{\kappa_{\boldsymbol{j},l}} \sum_{n \in \mathrm{G}_y} & \mathrm{e}^{-2\pi \mathrm{i} \kappa_{\boldsymbol{j},l} n/N_y} \\ & \cdot \sum_{\boldsymbol{m} \in \mathbf{G}_x} \mathrm{e}^{-2\pi \mathrm{i}(\boldsymbol{j}\cdot\boldsymbol{m} + ln)/N_x^{d-1}} g_{\boldsymbol{m},n}\,, \end{aligned} \tag{5.2.4}$$

where

$$\begin{aligned} \kappa_{\boldsymbol{j},l} &= \operatorname{sign}(l) \sqrt{\boldsymbol{j}^2 + l^2}\,, \\ (\boldsymbol{j}, l) &\in \mathbf{G}_x \times \mathrm{G}_{K_y}\,. \end{aligned}$$

This is the formula from [HSZ09a].

Remark 5.2.1: Note that we use the interval notation for the integer multi-indices for notational convenience. Moreover, we also choose the length of the Fourier transforms to be equal to N_x in the first $d-1$ dimensions, respectively. This could be generalized without changes in practice.

Now, we assume to sample g at M, not necessarily uniform, points $\boldsymbol{x}_m \in (-X/2, X/2)^{d-1}$: Then,

$$\begin{aligned}\hat{f}_{\boldsymbol{j},l} \approx \frac{2l}{\kappa_{\boldsymbol{j},l}} \sum_{n \in \mathrm{G}_y} e^{-2\pi \mathrm{i} \kappa_{\boldsymbol{j},l} n / N_y} \\ \cdot \sum_{m=1}^{M} \frac{h_m}{\Delta_x^{d-1}} e^{-2\pi \mathrm{i} (\boldsymbol{j} \cdot \boldsymbol{x}_m)/M} g_{m,n} \, .\end{aligned} \tag{5.2.5}$$

The term h_m is a weighting term. It is inversely proportional to the local sampling point density of $\boldsymbol{x}_m$ on the detector surface and has to fulfil $\sum_{m=1}^{M} h_m = (N_x \Delta_x)^{d-1} = X^{d-1}$. Note that the original formula (5.2.4) can be received from (5.2.5) by choosing $\{\boldsymbol{x}_m\}$ to contain all points on the grid $\Delta_x \mathbf{G}_x$.

Formula (5.2.5) can be interpreted as follows: Once we have computed the Fourier transform of the data and evaluated the Fourier transform at non-equidistant points with respect to the third coordinate, we obtain the (standard, equispaced) Fourier coefficients of f. The image can then be obtained by applying standard FFT techniques.

The straightforward evaluation of the sums on the right hand side of (5.2.5) would lead to a computational complexity of order $N_y^2 \times M^2$. Usually this is improved by the use of FFT methods, which have the drawback that they need both the data and evaluation grid to be equispaced in each coordinate. This means that if we want to compute (5.2.5) efficiently, we have to interpolate both in domain- and frequency space. A simple way of doing that is by using polynomial interpolation. It is used for photoacoustic reconstruction purposes for instance in the *k-wave* toolbox for Matlab [TC10]. Unfortunately, this kind of interpolation seems to be sub-optimal for Fourier-interpolation with respect to both accuracy and computational costs [Fou03; XFW02]

A regularized inverse k-space interpolation has already been shown to yield better reconstruction results [Jae+07]. The superiority of applying the NUFFT, compared to linear interpolation, has been shown theoretically and computationally by [HSZ09a].

5.3 The non-Uniform Fast Fourier Transform (NUFFT)

This section is devoted to the brief explanation of the theory and the applicability of the non-uniform Fourier transform, where we explain both the NER-NUFFT (Subsection 5.3.1) and the NED-NUFFT (Subsection 5.3.2) in the form (and spatial dimensions) we utilize them afterwards.

The NEDNER-NUFFT algorithm used for implementing (5.2.5) essentially (up to scaling factors) consists of the following steps:

1. Compute a $d-1$ dimensional NED-NUFFT in the $\boldsymbol{x}$-coordinates due to our detector placement.

2. Compute a one-dimensional NER-NUFFT in the K_y-coordinate as indicated by the reconstruction formula (5.2.5).

3. Compute an equispaced d-dim inverse FFT to obtain a d dimensional picture of the initial pressure distribution.

Such an algorithm has been introduced in [DR93]. In contrast to the present approach that is based on [Fou03], it uses Gaussian bells as window functions. The presented error estimate could be improved in [Ste98]. For a qualitative comparison of the most common available methods see [Fou03].

5.3.1 The Non-equispaced Range (NER-NUFFT) Case

With the NER-NUFFT (non-equispaced range – non-uniform FFT) it is possible to efficiently evaluate the discrete Fourier transform at non-equispaced positions in frequency domain.

To this end, we introduce the one dimensional discrete Fourier transform, evaluated at non-equispaced grid points $\kappa_l \in \mathbb{R}$:

$$\hat{\varphi}_l = \sum_{n \in \mathrm{G}_y} \varphi_n \mathrm{e}^{-2\pi \mathrm{i} \kappa_l n/N}, \quad l = 1, \ldots, M. \tag{5.3.1}$$

In order to find an efficient algorithm for evaluation of (5.3.1), we use a window function Ψ, an oversampling factor $c > 1$ and a parameter $c < \alpha < \pi(2c-1)$ that satisfy:

1. Ψ is continuous inside some finite interval $[-\alpha, \alpha]$ and has its support in this interval and

2. Ψ is positive in the interval $[-\pi, \pi]$.

Then (see [Fou03; HSZ09a]) we have the following representation for the Fourier modes occurring in (5.3.1):

$$e^{-\mathrm{i}x\theta} = \frac{c}{\sqrt{2\pi}\Psi(\theta)} \sum_{k \in \mathbb{Z}} \hat{\Psi}(x - k/c) \mathrm{e}^{-\mathrm{i}k\theta/c}, \ |\theta| \leq \pi \,. \tag{5.3.2}$$

By assumption, both Ψ and $\hat{\Psi}$ are concentrated around 0. So we approximate the sum over all $k \in \mathbb{Z}$ by the sum over the $2K$ integers k that are closest to $\kappa_l + k$. By choosing $\theta = 2\pi n/N - \pi$ and inserting (5.3.2) in (5.3.1), we obtain

$$\begin{aligned} \hat{\varphi}_l &\approx \sum_{k=-K+1}^{K} \hat{\Psi}_{l,k} \sum_{n \in \mathrm{G}_y} \frac{\varphi_n}{\Psi_n} e^{-2\pi i l n/cN}, \\ l &= 1, \text{ł} \ldots, M \,. \end{aligned} \tag{5.3.3}$$

Here K denotes the interpolation length and

$$\begin{aligned} \Psi_n &:= \Psi(2\pi n/N_y - \pi), \\ \hat{\Psi}_{l,k} &:= \frac{c}{\sqrt{2\pi}} \mathrm{e}^{-\mathrm{i}\pi(\kappa_l - (\mu_{l,k}))} \hat{\Psi}(\kappa_l - (\mu_{l,k})), \end{aligned} \tag{5.3.4}$$

where $\mu_{l,k}$ is the nearest integer (i.e. the nearest equispaced grid point) to $\kappa_l + k$.

The choice of Ψ is made in accordance with the assumptions above, so we need Ψ to have compact support. Furthermore, to make the approximation in (Equation 5.3.3) reasonable, its Fourier transform $\hat{\Psi}$ needs to be concentrated as much as possible in $[-K, K]$. In practice, a common choice for Ψ is the Kaiser-Bessel function, which fulfills the needed conditions, and its Fourier transform is analytically computable.

5.3.2 The Non-equispaced Data (NED-NUFFT) Case

A second major aim of the present work is to handle data measured at non-equispaced acquisition points $\boldsymbol{x}_m$ in an efficient and accurate way. Therefore we introduce the non-equispaced data, $d-1$ dimensional DFT

$$\begin{aligned} \hat{\varphi}_{\boldsymbol{j}} &= \sum_{m=1}^{M} \varphi_m \mathrm{e}^{-2\pi \mathrm{i}(\boldsymbol{j}\cdot\boldsymbol{x}_m)/N}, \\ \boldsymbol{j} &\in \mathbf{G}_x \,. \end{aligned} \tag{5.3.5}$$

The theory for the NED-NUFFT is largely analogous to the NER-NUFFT [Fou03] as described in Subsection 5.3.1. The representation (5.3.2) is here used for each entry of $\boldsymbol{j}$ and inserted (with now setting $\theta = 2\pi n/N$) into formula (5.3.5), which leads to

$$\begin{aligned} \hat{\varphi}_{\boldsymbol{j}} \approx \frac{1}{\Psi_{\boldsymbol{j}}} \sum_{m=1}^{M} \sum_{\boldsymbol{k}\in\{-K,\dots,K-1\}^{d-1}} & \varphi_m \hat{\Psi}_{\boldsymbol{j},\boldsymbol{k}} \\ & \cdot \mathrm{e}^{-2\pi \mathrm{i}\left(\boldsymbol{j}\cdot\boldsymbol{\mu}_{m,\boldsymbol{k}}\right)/cM}, \end{aligned} \tag{5.3.6}$$

where the entries in $\boldsymbol{\mu}_{m,\boldsymbol{k}}$ are the nearest integers to $\boldsymbol{x}_m + \boldsymbol{k}$. Here we have used the abbreviations

$$\begin{aligned} \Psi_{\boldsymbol{j},\boldsymbol{k}} &:= \prod_{i=1}^{d-1} \Psi(2\pi \boldsymbol{j}/N_x), \\ \hat{\Psi}_{\boldsymbol{j},\boldsymbol{k}} &:= \prod_{i=1}^{d-1} \left(\frac{c}{\sqrt{2\pi}}\right) \hat{\Psi}((\boldsymbol{x}_m)_i - (\boldsymbol{\mu}_{m,\boldsymbol{k}})_i), \end{aligned}$$

for the needed evaluations of Ψ and $\hat{\Psi}$.

Further remarks on the implementation of the NED- and NER-NUFFT, as well as a summary about the properties of the Kaiser-Bessel function and its Fourier transform can be found in [Fou03; HSZ09a].

5.4 The Experimental Setup

Before we turn to the evaluation of the algorithm we describe the photoacoustic setup. A detailed explanation and characterization of the working principles of our setup can be found in [ZLB08]. It consists of a Fabry Pérot (FP) polymer film sensor for interrogation [Bea05; BPM99], a 50 Hz pulsed laser source and a subsequent optical parametric oscillator (OPO) which emits optical pulses. These pulses have a very narrow

bandwidth and can be tuned within the visible and near infrared range. The optical pulses propagate through an optical fiber. When the light is emitted it diverges and impinges upon a sample. Some of this light is absorbed and partially converted into heat. This leads to a pressure rise generating a photoacoustic wave, which is then recorded via the FP-sensor head. The sensor head consists of an approximately 38 μm thick polymer (Parylene C) which is sandwiched between two dichroic dielectric coatings. These dichroic mirrors have a noteworthy transmission characteristic. Light from 600 to 1200 nm can pass the mirrors largely unattenuated, whereas the reflectivity from 1500 to 1650 nm (sensor interrogation band) is about 95% [ZLB08]. The acoustic pressure of the incident photoacoustic wave produces a change in the optical thickness of the polymer film. A focused continuous wave laser, operating within the interrogation band, can now determine the change of thickness at the interrogation point via FP-interferometry. The frequency response of this specific setup of up to 100 MHz has been analytically predicted, based on a model used in [BPM99] and experimentally confirmed [ZLB08]. There is a linear roll-off reaching zero at 57.9 MHz, with a subsequent rise.

5.5 Comparison of the NER-NUFFT Reconstruction with FFT and Time Reversal

In this section several reconstruction methods will be compared for regular grids. This will be done with synthetic data as well as with experimental data. All CPU based reconstructions are carried out with a workstation PC (Quad Core @ 3.6 GHz). All parameters that are not unique to the reconstruction method are left equal.

5.5.1 Synthetic Data

For the comparison of different implementations of the FFT based reconstruction we conduct a forward simulation of a solid sphere on a $200 \cdot 200 \cdot 100$ computational grid, using the *k-wave 1.1* Matlab library. The maximum intensity projections of the xy and the xz plane of all reconstructions are shown in Figure 5.1.

To obtain the closest possible numerical reconstruction of the Fourier based inversion formula, we directly evaluate the right hand side of formula (5.2.4), and subsequently invert a 3D equispaced Fourier transform by applying the conventional 3D (inverse) FFT. We call this reconstruction *direct FT*. It serves as ground truth for computing the correlation coefficient (appendix Subsection 5.9.2).

For the NUFFT reconstruction, the temporal frequency oversampling factor in (5.3.3) is set to $c = 2$ and the interpolation length is set to $K = 2$. In the linear interpolation FFT case, we use both $c = 1$ and $c = 2$. The FFT-reconstruction with $c = 1$ was conducted via the *k-wave* toolbox, which doesn't provide oversampling options out of the box. However the oversampling still can be achieved in a computationally not optimal way by adding zeros at the end of the data term in the time dimension. After reconstruction, the temporal dimension translates into the z axis. In the xy dimension no oversampling is performed.

The correlation coefficient and the computational time of the methods can be found in table Table 5.1. The errors indicate the superiority of the NUFFT reconstruction in comparison to linear interpolation, with a comparable computational effort (Table

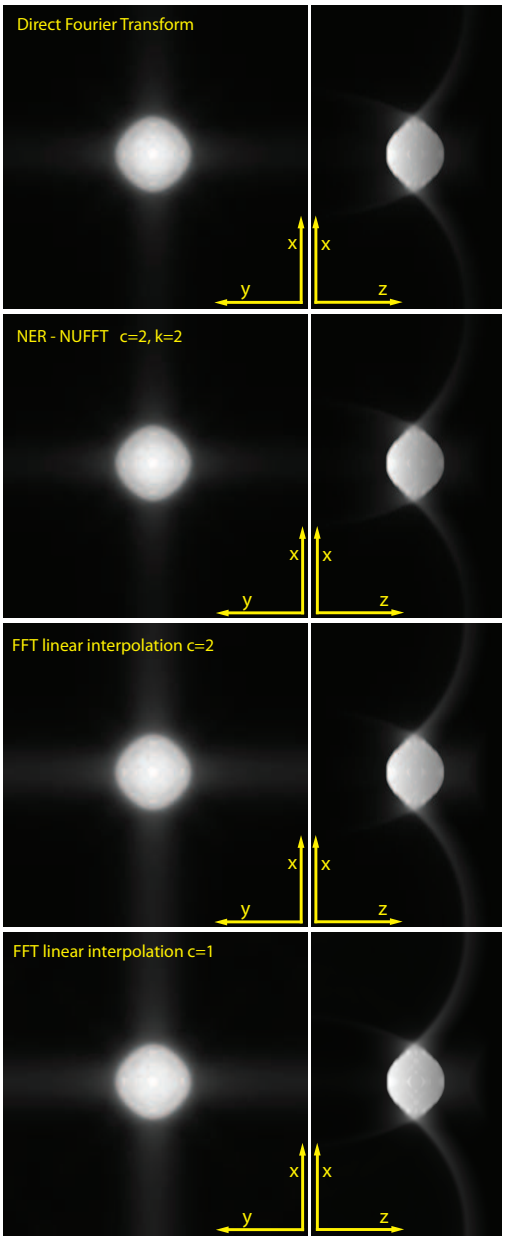

FIGURE 5.1: Maximum intensity projections (MIPs) in the xy and xz plane of different reconstructions, for a solid sphere. The direct Fourier Transform (top) serves as ground truth. c denominates the upsampling factor in the time domain and k the interpolation width of the Kaiser-Bessel function in (5.2.4).

	time	(correlation-100) in %			
	(s)	3D	xy	xz	yz
NER (c=2)	59	0.005	0.0003	0.001	0.001
FFT (c=2)	56	3.457	0.54	0.45	0.45
FFT (c=1)	53	14.00	0.65	0.81	0.81

TABLE 5.1: The first column compares computational times. In the last four columns the difference to a full correlation with the direct FT reconstruction method is given in %, for the 3D data and the 3 maximum intensity projections.

	time (s)	
embryo stage [HH92]	HH21	HH27
NER-NUFFT (k=2,c=2)	21	24
NER-NUFFT with precomputed Ψ	13	14
FFT with linear interpolation (c=2)	20	23
Time Reversal	7236	7659

TABLE 5.2: Comparison of the computational effort of two chick embryo data sets, with different reconstruction methods.

Table 5.1). The results also show that in the FFT case, an artificial oversampling in the temporal frequency dimension is highly recommended.

5.5.2 Experimentally Acquired Data

For an overall qualitative assessment two data sets, of a 3.5, and a 5 day old chick embryo, are used [Liu+14]. This corresponds to the development stages HH21 and HH27 of the Hamburger & Hamilton (HH) criterion [HH92]. The data are sampled with a spatial step size of $60\,\mu$m, covering an area of $1.008 \cdot 1.008\text{mm}^2$ (3.5 days) and $1.02 \cdot 1.02\text{mm}^2$ (5 days) and a time step size of 16 ns, corresponding to a maximum frequency of 31.25 MHz. To avoid aliasing the signal is low pass filtered to the maximal spatial frequency of 25.3 MHz. A full reconstruction with the NER-NUFFT for the 5 day old embryo is shown in Figure 5.6.

The time reversal reconstruction is performed via the *k-wave* toolbox. The spatial upsampling factor in the x, y direction is set to 2. For time reversal this is realized by linearly interpolating the sensor data to a finer grid, whereas for the FFT based reconstructions zero padding in the Fourier domain is performed.

The oversampling factor for the FFT reconstructions in the time domain is $c = 2$. The number of time steps used for the reconstruction covers more than twice the depth range of the visible objects and is 280 for the HH21 and 320 for the HH27 embryo.

In table Table 5.2 a comparison for the computational time is shown. For the NUFFT case, Ψ as defined in (5.3.4) can be precomputed, which roughly halves reconstruction time in subsequent reconstructions using the same discretization, as has been already reported in [Sch+11]. Moreover, the computation time improves by a factor of 200 when using FFT-based reconstructions instead of time reversal.

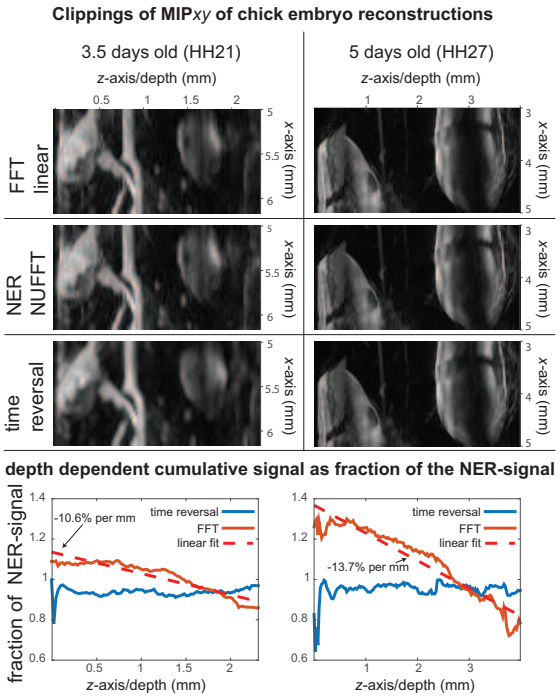

FIGURE 5.2: The top shows clippings of the MIPs along the y-axis for the two chick embryos. The three reconstruction methods from top to bottom are: FFT with linear interpolation, NER-NUFFT and time reversal. All reconstructions are normalized, so their maximum value is 1. On the bottom graphs, the cumulative signal for each z-axis layer is plotted as a fraction of the corresponding NER-NUFFT layer. While the depth dependent signal between the time reversal reconstruction and the NER-NUFFT roughly remains the same, for the FFT with linear interpolation a fall-off can be observed. The linear fit suggests a reduction of 10.6 % per mm for the 3.5 days old chick embryo and 13.7 % per mm for the 5 days old data.

The relative Tenenbaum sharpness (appendix Subsection 5.9.2) for the 3D data of the 3.5 days old chick embryo was slightly better for the NER-NUFFT reconstruction (44.2) than for time reversal (43.0) and FFT with linear interpolation (41.1). A comparison of clippings of the maximum intensity projection (MIP) in the xz plane is shown in Figure 5.2. The time reversal reconstruction seems smoothed compared to the FFT reconstructions, which is probably a result of the different spatial upsampling modalities.

In the bottom graphs of Figure 5.2 the cumulative reconstructed signal for each layer is plotted, as fraction of the NER-NUFFT cumulative signal. The additional fall-off for the FFT with linear interpolation has been determined by a line fit. For the 3.5 day old embryo it was 10.6 % per mm and 13.7 % per mm for the 5 day old embryo. While it intuitively makes sense that the z-axis is primarily affected by errors introduced by a sub-optimal implementation of equation (5.2.1), this problem needs further research to be fully understood.

5.6 Non-equispaced Sensor Placement

The current setups allow data acquisition at just one single sensor point for each laser pulse excitation. Since our laser is operating at 50 Hz data recording of a typical sample requires several minutes. In an effort to reduce data acqusition time, we try to maximize the image quality for a given number of acquisition points and a given region of interest.

Our newly implemented NEDNER-NUFFT is ideal for dealing with non-equispaced positioned sensors, as error analyses for the NED- and the NER-NUFFT indicate [Fou03]. This newly gained flexibility of sensor positioning offers many possibilities to enhance the image quality compared to a rectangular grid.

Also any non-equispaced grids that may arise from a specific experimental setup can be efficiently computed via the NEDNER-NUFFT approach.

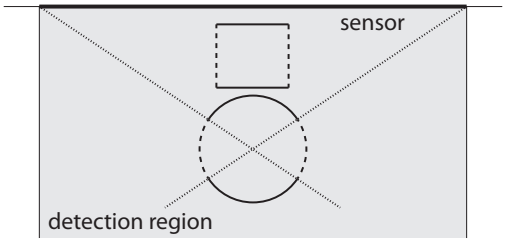

FIGURE 5.3: Depiction of the limited view problem. Edges whose normal vectors cannot intersect with the sensor surface are invisible to the sensor. The invisible edges are the coarsely dotted lines. The detection region is marked by a grey background. The finely dotted lines are used to construct the invisible edges. Edges perpendicular to the sensor surface are invisible for a plane sensor.

5.6.1 Equi-angular and Equi-steradian Projections

In this article, we use the NEDNER-NUFFT to tackle the limited view or limited aperture problem, for the case of a limited number of available detectors, which can be placed discretionary on a planar surface. To understand the limited view problem, it is helpful to define a detection region. According to [Xu+04], this is the region which is enclosed by the normal lines from the edges of the sensor. Mathematically speaking, the wave front propagates on straight lines in the direction of the singularity [HÖ3, Chapter VIII]. As a consequence the reconstruction is locally stable if the straight line through the normal to the object boundary passes through the detector surface [LQ00]. Therefore certain edges are invisible to the detector, as depicted in Figure 5.3. One approach to overcome this problem experimentally has been made by enclosing the target in a reverberant cavity [CAB07]. In addition, a lot of effort has been made to enhance reconstruction techniques in order to deal with the limited view problem [FQ15; Dan+12; Xu+04; TL10; Ana+08; Wan+11].

Our approach to deal with this problem is different. It takes into account that in many cases the limiting factor is the number of sensor points and the limited view a consequence of this constraint. We use an irregular grid arrangement that is dense close to a center of interest and becomes sparser the further away the sampling points are located.

We realize this by means of an equi-angular, or equi-steradian sensor arrangement, where for a given point of interest each unit angle or steradian gets assigned one sensor point. This arrangement can also be seen as a mock hemispherical detector.

For the equi-angular sensor arrangement a point of interest is chosen. Each line, connecting a sensor point with the point of interest, encloses a fixed angle to its adjacent line. In this sense we mimic a circular sensor array on a straight line. The position of the sensor points is pictured on top of the third image in Figure 5.4.

The obvious expansion of an equi-angular projection to 3D is the equi-steradian projection. Here we face a problem analogous to the problem of placing equispaced points on a 3D sphere and then projecting the points, from the center of the sphere, onto a 2D plane outside the sphere (the detector plane).

The algorithm used for this projection is explained in detail in appendix Subsection 5.9.2. Our input variables are the diameter of the detection region, which we define as the diameter of the disc where the sensor points are located, the distance of the center of interest from the sensor plane r and the desired number of acquisition points. In the top left section of Figure 5.7 and Figure 5.8 the sensor arrangements are depicted.

5.6.2 Weighting Term

To determine the weighting term h_m in (5.2.5) for 3D we introduce a function that describes the density of equidistant points per unit area ρ_p. In our specific case, ρ_p describes the density on a sphere around a center of interest. Further we assume that ρ_p is spherically symmetric and decreases quadratically with the distance from the center of interest r: $\rho_{p,s} \propto 1/r^2$. We now define $\rho_{p,m}$ for a plane positioned at distance r_0 from the center of interest. In this case $\rho_{p,s}(r)$ attenuates by a factor of $\sin\alpha$, where $\alpha = \arcsin(r_0/r)$ is the angle of incidence. Hence $\rho_{p,m} \propto r_0/r^3$. This yields a weighting term of:

$$h_m(r) \propto r^3$$

Analogously we can derive h_m for 2D:

$$h_m(r) \propto r^2$$

For the application of this method to the FP setup it is noteworthy that there is a frequency dependency on sensitivity which itself depends on the angle of incidence. These characteristics have been extensively discussed in [CB07].

5.7 Application of the NEDNER-NUFFT with Synthetic Data in 2D

A tree phantom, designed by Brian Hurshman and licensed under CC BY 3.0[1], is chosen for the 2 dimensional computational experiments on a grid with $x = 1024$ $z = 256$ points. A forward simulation is conducted via *k-wave 1.1* [TC10]. The forward simulation of the k-wave toolbox is based on a first order k-space model. A PML (perfectly matched layer) of 64 grid points is added. Also white noise is added to obtain an SNR (signal to noise ratio) of 30 dB.

[1] http://thenounproject.com/term/tree/16622/

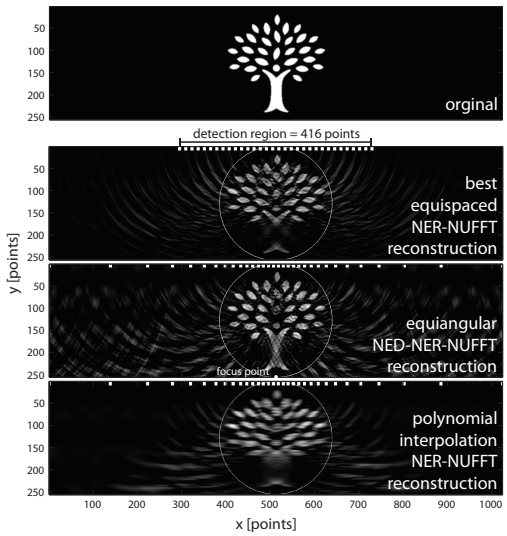

FIGURE 5.4: Various reconstructions of a tree phantom (top) with different sensor arrangements. All sensor arrangements are confined to 32 sensor points. The sensor positions are indicated as white rectangles on the top of the images. The second image shows the best (see Figure 5.5) equispaced sensor arrangement, with a distance of 13 points between each sensor. The third image shows the NEDNER-NUFFT reconstruction with equi-angular arranged sensor positions. The bottom image shows the same sensor arrangement, but all omitted sensor points are polynomially interpolated and afterwards a NER-NUFFT reconstruction was conducted.

In Figure 5.4 our computational phantom is shown at the top. For each reconstruction a subset of 32 out of the 1024 possible sensor positions was chosen. In Figure 5.4 their positions are marked at the top of each reconstructed image. For the equispaced sensor arrangements, we let the distance between two adjacent sensor points sweep from 1 to 32, corresponding to a detection region sweep from 32 to 1024. The sensor points are always centered in the x-axis.

To compare the different reconstruction methods we use the correlation coefficient and the Tenenbaum sharpness. These quality measures are explained in appendix Subsection 5.9.2.

We apply the correlation coefficient only within the region of interest marked by the white circle in Figure 5.4. The Tenenbaum sharpness was calculated on the smallest rectangle, containing all pixels within the circle. The results are shown in Figure 5.5.

The Tenenbaum sharpness for the equi-angular sensor placement is 23001, which is above all values for the equispaced arrangements. The correlation coefficient is 0.913 compared to 0.849, for the best equispaced arrangement. In other words, the equi-angular arrangement is 42.3 % closer to a full correlation than any equispaced grid.

In Figure 5.4 the competing reconstructions are compared. While the crown of the tree is depicted quite well for the equispaced reconstruction, the trunk of the tree is barely visible. This is owed to the limited view of the detection region. As the equispaced interval and the detection region increase, the trunk becomes visible, but at the cost of

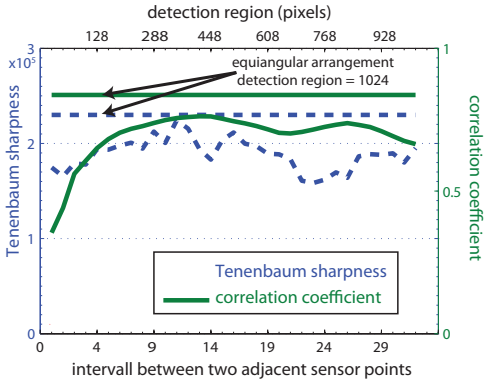

FIGURE 5.5: Correlation coefficient and Tenenbaum sharpness for equispaced sensor arrangements with intervals between the sensor points reaching from 1 to 32. The maximum of the correlation coefficient is at 13. The corresponding reconstruction is shown in Figure 5.4. The straight lines indicate the results for the equi-angular projection.

the crown's quality. In the equi-angular arrangement a trade off between these two effects is achieved. Additionally the weighting term for the outmost sensors is 17 times the weighting term for the sensor point closest to the middle. This amplifies the occurrence of artifacts, particularly outside the region of interest.

The bottom image in Figure 5.4 shows the equi-angular sensor arrangement, where the missing sensor points are polynomially interpolated to an equispaced grid and a NER-NUFFT reconstruction is applied afterwards. The interpolation is conducted for every time step from our subset to all 1024 sensor points. The correlation coefficient for this outcome was 0.772 while the sharpness measure is 15654. This outcome exemplifies the clear superiority of the NUFFT to conventional FFT reconstruction when dealing with irregular grids.

5.8 Application of the NEDNER-NUFFT with Experimental Data in 3D

We will now examine if the positive effects of the NEDNER-NUFFT reconstruction with non-equispaced detectors are transferred to 3D data. For these comparisons we use the data sets of the two chick embryos already presented in Subsection 5.5.2. By the use of polynomial interpolation for each time step, we map this data to discretionarily placed points on the acquisition plane. Thus sensor data is obtained for regular and irregular grids with arbitrary step sizes. The sensor positions are indicated by the red dots in Figure 5.7 and Figure 5.8.

This procedure allows us to use a full reconstruction as a ground truth and thus ensures a quantitative quality control via the correlation coefficient (Appendix Subsection 5.9.2). We are also safe from any experimental errors that could be introduced between measurements. A drawback is that we can only interpolate to step sizes $\geqq 60\mu$m without loss of information. Therefore the presented images are always made with rather

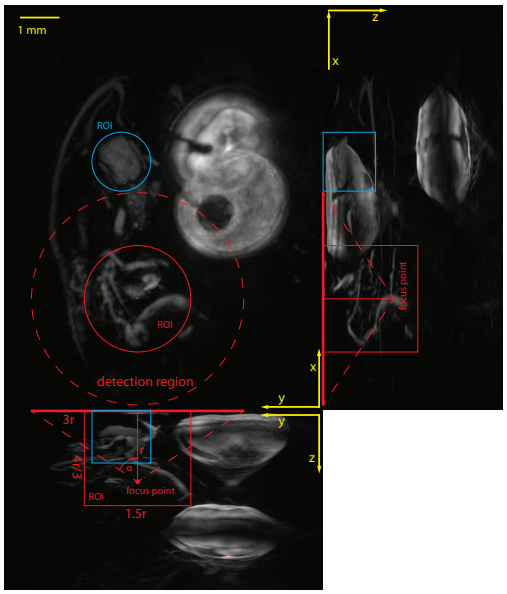

FIGURE 5.6: MIPs (maximum intensity projections) of a full NER-NUFFT reconstruction of a 5 day old chick embryo (HH27), cropped along the y-axis. Two cylindrical ROIs (regions of interest) are indicated, each by a circle and two rectangles. The red ROI is discussed in Figure 5.8, the blue ROI in Figure 5.7. For the red ROI the focus point for the equi-steradian arrangement is shown and the detection region, which marks the area where sensor points are located. The distance r of the 'focus point' from the plane governs the size of the detection region and the ROI, according to the proportions shown. Within the detection region all sensor points occupy the same steradian from the focus point's perspective.

few sensor points and naturally of a lower quality. However we want to emphasize that this is a result of our experimental procedure.

For all comparison reconstructions the NEDNER-NUFFT has been used for practical reasons. While the NER-NUFFT cannot deal with non rectangular grids, it is equivalent to the NEDNER-NUFFT for rectangular regular grids. Using the NEDNER-NUFFT the spacing of the computational grid can be chosen freely. It corresponds to the width of the Kaiser-Bessel function for interpolation (see (5.3.6)). If the computational grid is much finer than the local sensor point density, a strong signal close to the sensor surface will produce high intensity spots with an intensity distribution according to the Kaiser-Bessel function, instead of a homogeneous area. Making the computational grid coarser than the sensor point density produces a more blurry reconstruction with a reduced lateral resolution. The computational grid therefore is chosen as fine as possible without reducing the lateral resolution.

We use the two chick embryo data sets to extract the irregular sensor data via layer-wise polynomial interpolation. A clipping of the MIPxz of reconstruction of both chick embryos is shown in Figure 5.2. A full NER-NUFFT reconstruction of the 5 day old chick embryo is shown in Figure 5.6. For the comparisons we define a region of interest (ROI) in the form of a cylinder with a height to diameter ratio of 8:9. The area where the sensor points are located for a given reconstruction will be called the *detection region*. The proportions between the ROI and the detection region is the same for all measurements as depicted in Figure 5.8.

In order to avoid spatial aliasing the time data have been low pass filtered with a cut off frequency according to $F_{cutoff} = c_{sound}/2dx$ where c_{sound} is the sound speed and dx the step size. In the equi-steradian grid, the (locally varying) stepsize dx has been defined as the distance to the nearest neighboring point.

We now conduct a fair comparison between the equi-steradian sensor arrangement described in appendix Subsection 5.9.2 and regular grid arrangements for the given ROI. This is done by maximizing image fidelity, while always using (approximately) the same number of sensor points. The comparisons are undertaken for three different ROIs. This is done to show that the advantages of the equi-steradian arrangement are not confined to a single case, but rather consistent for different features and volume sizes. All selected ROIs need to have a detection region, that is fully covered by the underlying data set.

The results are shown in Figure 5.7, Figure 5.8 and Figure 5.9. The figures are organized in a similar manner and depict different reconstructions via maximum intensity projections (MIPs). On the top left segment, the equi-steradian grid arrangement is shown. The top right segment shows the ground truth: A NEDNER-NUFFT reconstruction using all original sensor points that are placed within the detection region. In the segments below, the regular grid reconstructions are shown. On the left the detection region coincides with the region of interest, on the right it is coincides with the detection region. Figure 5.7 and Figure 5.8 also show the sensor point placement. While in the small detection region the reconstructions have a good resolution, edges are blurred and certain features are invisible. As the detection region increases, these features appear, at the cost of reduced overall resolution. The equi-steradian grid arrangement has a rather high resolution towards the center, while still displaying the mentioned features.

All the above figures contain four graphs, which depict the correlation coefficient for the three MIPs and the volume data. The detection region for the regular grids is

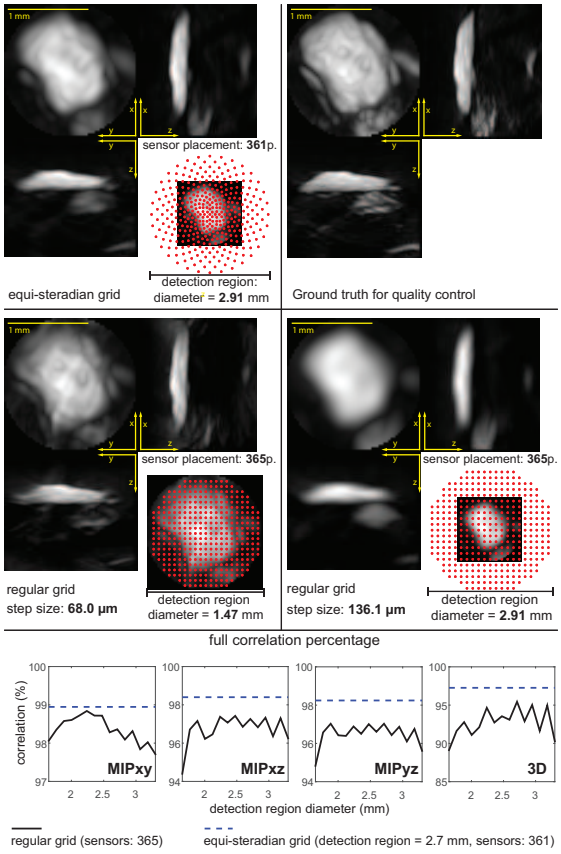

FIGURE 5.7: Comparisons of different reconstructions for a region of interest (ROI), (marked blue in Figure 5.6) with roughly 360 sensor points. All reconstructions are presented in the form of MIPs. The top right shows the ground truth, the top left the equi-steradian sensor arrangement. Below them the reconstructions of the regular grids for the largest and the smallest detection region are depicted. On the bottom the correlation coefficient for different regular grids is shown for the three MIPs and the 3D-data.

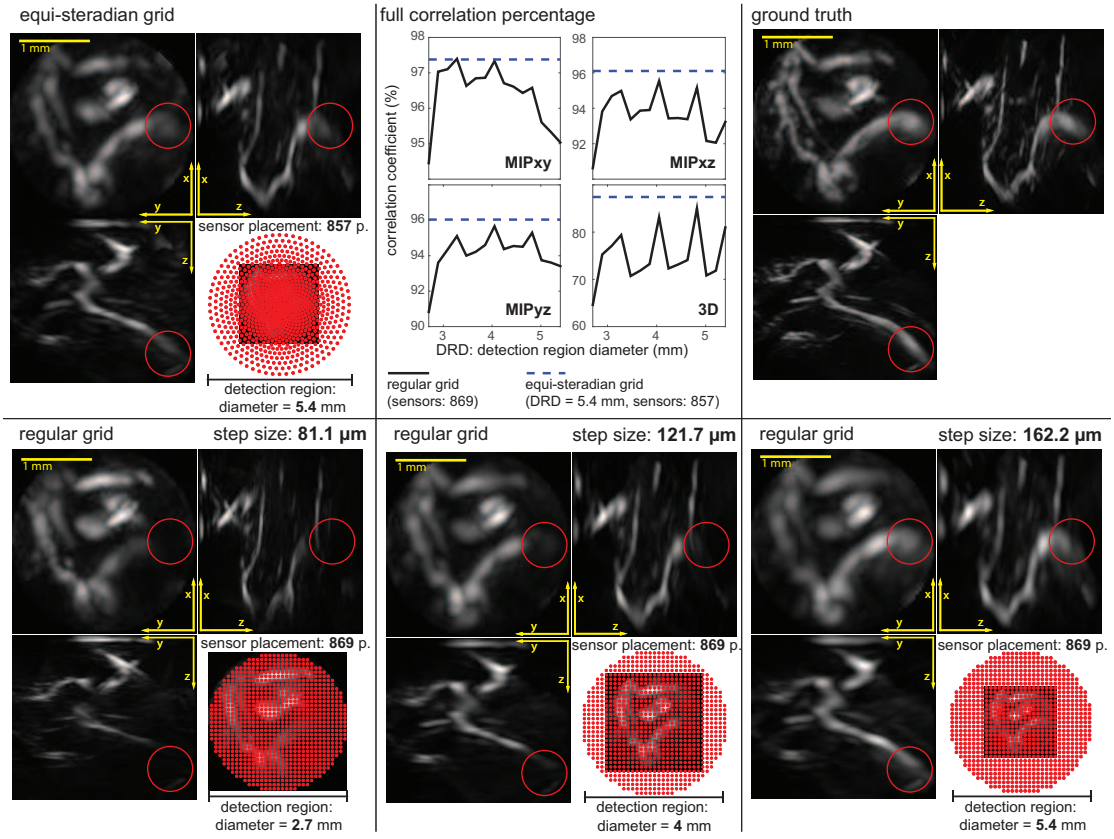

FIGURE 5.8: Comparisons of different reconstructions for a region of interest (ROI), (marked as red in Figure 5.6) with roughly 870 sensor points. All reconstructions have been cropped to the cylindrical ROI. Three maximum intensity projections (MIPs), are shown for every reconstruction. The sensor placement is indicated by red dots, which overlay the MIPxy on the bottom right of the dedicated segment. The three bottom segments show regularly arranged sensor points. The detection region diameter (DRD) for the three bottom segments is 2.7, 4 and 5.4 mm while the number of sensor points always remains 869. Certain features (red circle) are not visible for the small detection regions, due to the limited view problem. As the detection region becomes larger, these features start to appear, at the cost of overall resolution. The equi-steradian arrangement shown on the top left still shows these features, while maintaining a high resolution. On the top right a reconstruction with all original points of the detection region is shown. This was used as ground truth. On the top center segment, the correlation coefficient, for different regular grids is shown.

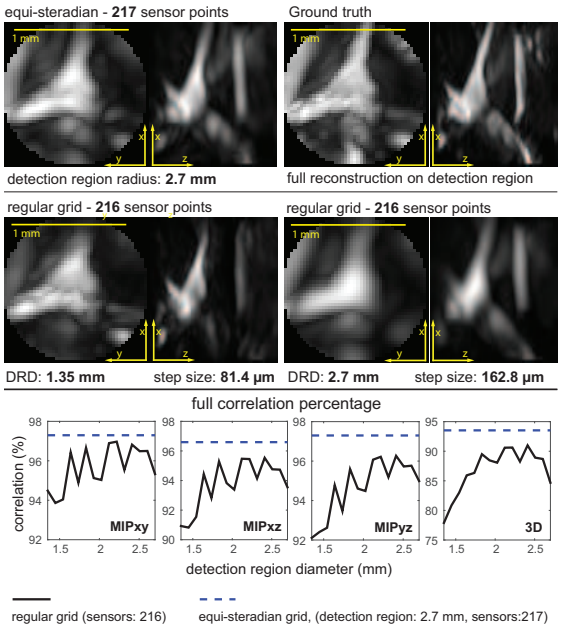

FIGURE 5.9: Reconstruction comparisons of the center region of the 3.5 day old chick embryo (HH21). The depiction is analog to Figure 5.7, without the MIPyz and the sensor placement.

increased and shown on the x-axis, while the number of acquisition points stays constant. The computational grid was chosen to be as small as possible but greater than the step size and has been increased in steps of 30μm in order to have a consistent μm/pixel spacing in the reconstruction.

The results show that the equi-steradian arrangement consistently produces reconstructions that outperform every regular grid arrangement. It provides a good combination of a large detection region and high resolution at the region of interest. This is demonstrated by the juxtaposition of different reconstructions and also confirmed via the correlation coefficient.

5.9 Conclusions

5.9.1 Summary and Results

We computationally implemented a 3D non-uniform FFT photoacoustic image reconstruction, called NER-NUFFT (non equispaced range-non uniform FFT) to efficiently deal with the non-equispaced Fourier transform evaluations arising in the reconstruction formula.

In the computational results, it could be shown that the NER-NUFFT is much closer (more than 100 times in the test piece) to perfect correlation than the FFT reconstruction with linear interpolation.

We then used real data sets for comparison, recorded with a FP-planar sensor setup [ZLB08] and included the *k-wave* time reversal algorithm. Regarding reconstruction time the results of [Sch+11] and [HSZ09a] could be confirmed for 3D, where the FFT with

linear interpolation performs similar to NER-NUFFT. Additionally, the NER-NUFFT reconstruction time could be significantly reduced (almost halved), if the values of the interpolation functions Ψ and $\hat{\Psi}$ had already been pre-computed for the chosen discretization. The time reversal computation took more than 300 times longer on a CPU, than any FFT based reconstruction. Concerning image quality, the NER-NUFFT and time reversal reconstruction perform on a very similar level, while the conventional FFT method fails to correctly image the depth-dependent intensity fall-off. While this fall-off is almost synchronous for time reversal and NER-NUFFT, there was an additional intensity drop of about 10 % per mm in the linear interpolation FFT based reconstruction.

The second application of the NUFFT approach concerned the applicability of irregular grid arrangements, which were new in photoacoustic tomography. In fact, this was done by implementing the NEDNER-NUFFT (non equispaced data-NER-NUFFT). Our goal was to maximize image quality in a given region of interest, using a limited number of sensor points. To do this we developed an equi-angular sensor placement for 2D and an equi-steradian placement in 3D, which assigns one sensor point to each angle/steradian for a given center of interest.

For the 2D simulations we showed that this arrangement enhances the image quality for a given region of interest and a confined number of sensor points in comparison to regular grids.

In 3D we used the aforementioned chick embryo data and reconstructed with an interpolated subset of the original sensor data. We thus conducted a fair comparison between regular grid arrangements and the equi-steradian arrangement with a limited number of sensor points for three regions of interest. While the volume of these regions ranged from 1.7 to 13.7 mm^3 the shape always remained a cylinder with a height to diameter ratio of 8:9.

For our regions of interest, the correlation of the equi-steradian arrangement to the full reconstruction, was consistently higher than any regular grid arrangement, using an almost equal number of sensor points.

5.9.2 Discussion

For the case of regular sampled grids the results of [HSZ09a] where confirmed for 3D in the synthetic data experiments. The synthetic data results further show the importance of using a zero-pad factor of at least 2 in the time domain, when using FFT based reconstruction methods. In the case of real data, The main identifiable difference was the additional intensity drop for greater depth of the FFT reconstruction in comparison to the other two methods. The great computational advantage of using FFT based reconstructions makes it the most suitable method for most cases in a planar sensor geometry setup. There was no detectable difference in the reconstruction quality between the NER-NUFFT and time reversal. From our point of view, the use of the NER-NUFFT therefore seems to be especially useful in the case of high resolution imaging in relatively deep-lying regions.

The NEDNER-NUFFT implementation allowed to efficiently reconstruct data from non-equispaced sensor points. This is used to extend the primary application of a planar sensor surface, recording images over a large area, by the possibility to image a well defined region of interest with a shorter acquisition time. Thus we designed a sensor mask to better image small regions in larger depths at a fixed number of sensor points,

using a design that projects an equispaced hemispherical detector geometry onto a planar sensor surface. For this case our sensor arrangement produced consistently better reconstructions than any regular grid, because it allowed to maintain a high resolution within our region of interest, while still capturing features that could only be detected outside the region of interest. In our test examples, the NEDNER-NUFFT further enhances the image quality in deep regions while maintaining a reasonable computational effort.

In comparison to a real hemispherical detector, there is an increase of acoustic attenuation. This is countered by greater accessibility, scalability and flexibility on the planar detector. The region of interest not necessarily needs to fit into a spherical shape, the size of the region of interest just has an upper bound and the number of acquisition points is limited by the measurement time.

As an outlook, we mention that the case where the field of view is much larger than the imaging depth has not been investigated in this paper. For this case a similar approach of expanding the field of view by non-equispaced sensor point placement is possible. This could mitigate the image degradation towards the boundaries of the detection region. However the achievable benefit of such a method would decrease with an increase of the ratio of the detection region area to the detection region boundary and the maximum imaging depth.

Acknowledgment

This work is supported by the Medical University of Vienna, the European projects FAMOS (FP7 ICT 317744) and FUN OCT (FP7 HEALTH 201880), Macular Vision Research Foundation (MVRF, USA), Austrian Science Fund (FWF), Project P26687-N25 (Interdisciplinary Coupled Physics Imaging), and the Christian Doppler Society (Christian Doppler Laboratory "Laser development and their application in medicine"). We further want to thank Barbara Maurer and Wolfgang J. Weninger from the Center for Anatomy and Cell Biology at the Medical University of Vienna for providing us with the chick embryo.

Appendix: Algorithm for Equi-steradian Sensor Arrangement

In our algorithm, the diameter of the detection region and the distance of the center of interest from the sensor plane is defined. The number of sensor points N will be rounded to the next convenient value.

Our point of interest is placed at $z = r_0$, centered at a square xy grid. The point of interest is the center of a spherical coordinate system, with the polar angle $\theta = 0$ at the z-axis towards the xy-grid.

First we determine the steradian Ω of the spherical cap from the point of interest, that projects onto the acquisition point plane via

$$\Omega = 2\pi \left(1 - \cos\left(\theta_{max}\right)\right) .$$

This leads to a unit steradian $\omega = \Omega/N$ with N being the number of sensors one would like to record the signal with. The sphere cap is then subdivided into slices k which

satisfy the condition

$$\omega\, j_k = 2\pi \left(\cos\left(\theta_{k-1}\right) - \cos\left(\theta_k\right)\right),$$

where θ_1 encloses exactly one unit steradian ω and j_k has to be a power of two, in order to guarantee some symmetry. The value of j_k doubles, when $r_s > 1.8 \cdot r_k$, where r_s is the chord length between two points on k and r_k is the distance to the closest point on $k-1$. These values are chosen in order to approximate local equidistance between acquisition points on the sensor surface.

The azimuthal angles for a slice k are calculated according to:

$$\varphi_{i,k} = \left(2\pi i\right)/j_k + \pi/j_k + \varphi_r\,,$$

with $i = 0, \ldots, j-1$, where

$$\varphi_r = \varphi_{j_{k-1},k-1} + \left(k-1\right) 2\pi/\left(j_{k-1}\right)$$

stems from the former slice $k-1$. The sensor points are now placed on the xy-plane at the position indicated by the spherical angular coordinates:

$$(\mathrm{pol}, \mathrm{az}) = \left(\left(\theta_k + \theta_{k+1}\right)/2, \varphi_{i,k}\right)$$

Appendix: Quality Measures

In the case where a ground truth image is available, we choose the correlation coefficient ρ, which is a measure of the linear dependence between two images U_1 and U_2. Its range is $[-1,1]$. A correlation coefficient close to 1 indicates linear dependence [Sch11]. It is defined via the variance $\mathrm{Var}\left(U_i\right)$ of each image and the covariance $\mathrm{Cov}\left(U_1, U_2\right)$ of the two images:

$$\rho\left(U_1, U_2\right) = \frac{\mathrm{Cov}(U_1,U_2)}{\sqrt{\mathrm{Var}(U_1)\mathrm{Var}(U_2)}}\,. \tag{5.9.1}$$

We decided not to use the widely applied L^p distance measure because it is a morphological distance, meaning it defines the distance between two images by the distance between their level sets. Therefore two identical linearly dependent images can have a correlation coefficient of 1 and still a huge L^p distance. This can be dealt with by normalizing the data as in [Xu+04; TL10]. We choose the correlation coefficient instead, because in experimentally acquired data single high intensity artifacts can occur, which would have a disproportionately large effect on the normalized L^p distance.

In case of experimentally collected data, there are only a few methods available for the comparison of different reconstruction methods. A possible way for measuring sharpness is obtained from a measure for the high frequency content of the image [GYL85].

Out of the plethora of published focus functions we select the Tenenbaum function, because of its robustness to noise:

$$F_{\mathrm{Tenenbaum}} = \sum_{x,y} \left(g * U_{x,y}\right)^2 + \left(g^T * U_{x,y}\right)^2\,, \tag{5.9.2}$$

with g as the Sobel operator:

$$g = \begin{pmatrix} -1 & 0 & 1 \\ -2 & 0 & 2 \\ -1 & 0 & 1 \end{pmatrix}. \tag{5.9.3}$$

Like the L^2 norm and unlike the correlation coefficient, the Tenenbaum function is an extensive measure, meaning it increases with image dimensions. Therefore we normalized it to $\overline{F}_{\text{Tenenbaum}} = F_{\text{Tenenbaum}}/N$, where N is the number of elements in U.

6

Texture Generation for Photoacoustic Elastography

Thomas Glatz, Otmar Scherzer and Thomas Widlak

Abstract

Elastographic imaging is a widely used technique which can in principle be implemented on top of every imaging modality. In elastography, the specimen is exposed to a force causing local displacements, and imaging is performed before and during the displacement experiment. The computed mechanical displacements can either directly be used for clinical diagnosis, or deliver a basis for the deduction of material parameters. Photoacoustic imaging is an emerging image modality, which exhibits functional and morphological contrast. However, opposed to ultrasound imaging, for instance, it is considered a modality which is not suited for elastography, because it does not reveal speckle patterns. However, this is somehow counter-intuitive, because photoacoustic imaging makes available the whole frequency spectrum as opposed to single frequency standard ultrasound imaging. In this work, we show that in fact artificial speckle patterns can be introduced by using only a band-limited part of the measurement data. We also show that after introduction of artificial speckle patterns, deformation estimation can be implemented more reliably in photoacoustic imaging.

6.1 Introduction

Elastography is an imaging technology for visualization of biomechanical properties; among its current clinical applications are early detection of skin, breast and prostate cancer, detection of liver cirrhosis, and characterization of artherosclerotic plaque in vascular imaging (see for instance [Doy12; PDR11; Wej+10; Aig+11; Wan+09; Woo+06; Bis+10]).

Typically, elastography is implemented as an *on top imaging method* to various existing imaging techniques, such as ultrasound imaging (see for instance [Ler+88; Oph+91]), magnetic resonance imaging (see for instance [Mut+95; Man+01]) or optical coherence tomography (see for instance [SSY11; Nah+13]). With all these techniques, it is possible to visualize momentum images, from which mechanical displacements $\boldsymbol{u}$ can be calculated, which forms the basis of clinical examinations.

For motion estimation in *ultrasound elastography (USE)*, *optical coherence elastography (OCE)* and in certain variants of *magnetic resonance elastography (MRE)*, common techniques are optical flow and motion tracking algorithms [PDR11; Boh+00; Sch98; PB14; PM92; Fu+11]; in USE and OCE, these are specifically referred to as *speckle tracking methods*. Speckle tracking can only be realized if the imaging data contains a high amount of correlated pattern information. This is the predominant structure in ultrasound imaging.

Photoacoustic imaging is an emerging functional and morphological imaging technology, which, for instance, is particularly suited for imaging of vascular systems [Bea11; NSP14; LW09]. Opposed to ultrasound imaging, photoacoustic imaging is considered to reveal little speckle patterns [LW06], which is considered an advantage for imaging but a disadvantage for elastography. Passive coupling of photoacoustic imaging and elastography has been reported in [Eme+04], where the contrast of photoacoustic imaging, ultrasound, and US-elastography has been fused (see also [PDR11, sec.4.9]). Active coupling of photoacoustic and elastography has not been reported so far. The reason for that is that motion estimation and speckle tracking cannot be implemented reliably because of homogeneous regions in monospectral photoacoustic imaging, which do not allow for detection of microlocal displacements.

In this paper, we provide a mathematically founded way of introducing speckle in photoacoustic imaging data. Theoretically, photoacoustic imaging is based on the assumption that the whole frequency spectrum of the pressure can be measured by the detectors. Common ultrasound imaging, on the contrary, is operating with a fixed single frequency mode. This superficial comparison motivates us to investigate, using [Hal11; HSZ09b], how much effect band-limited measurements have on the imaging process. In fact, as we show by mathematical consideration, the use of band-limited data enforces speckling-like patterns in the reconstructions. Our suggested approach then consists of carefully choosing a frequency band of measurements and back-projecting these data. Because these data is speckled, it can be used to support tracking and optical flow techniques for displacement estimations.

Our method of choice for detecting displacements in the photoacoustic imaging data is the *optical flow*. In pure mathematical terms, the equation is well-defined only for smooth imaging data. The high contrast of photoacoustic data causes a violation of this smoothness assumption. To make the photoacoustic data applicable for optical flow computations one can smooth the data prior to estimating the optical flow field [BSW05]. In this paper, we show that the proposed method of texture generation is a convergent regularization method; compared to other smoothing techniques, like for instance Gaussian filtering, it performs better on high-contrast image data.

The structure of the article is as follows: We first review the principles of elastography in Section 6.2. In Section 6.3 we review the principles of photoacoustic imaging and in Section 6.4, we treat the case of band-limited data in photoacoustics. Then, in Section 6.5, we describe the methods to create texture patterns in photoacoustic imaging and use them for motion estimation for photoacoustic elastography. Section 6.6 provides a regularization point of view on texture generation: Anticipating the necessity of smoothing high contrast image data before optical flow processing, we show that smooth imaging data is in fact very well approximated by the proposed texture generation process. in Section 6.7, we show the results of imaging experiments. The paper ends with a discussion (Section 6.8).

6.2 Elastographic Imaging

In this section we explain the basic principles of elastography. In theory, elastography can be implemented on top of any imaging technique. Below, we review mathematical models which are used for qualitative elastography.

6.2.1 Experiments and Measurement Principle

According to [Doy12], elastography consists of the following consecutive steps:

1. The specimen is exposed to a mechanical source. Imaging is performed before and during source exposition.
2. **Qualitative elastography:** From the images the tissue displacement $\boldsymbol{u}$ is determined.
3. **Quantitative elastography:** Mechanical properties are computed from the displacement $\boldsymbol{u}$.

In the literature there have been documented various ways to perturb the tissue, such as quasi-static, transient and time-harmonic excitation.

In this paper we focus on qualitative elastography in the quasi-static case, which is reviewed below.

6.2.2 Motion Estimation in Quasi-static Qualitative Elastography

Although it is theoretically possible to perform quantitative imaging all at once, in practice, qualitative imaging is performed beforehand. Depending on the used modalities different models are used for qualitative elastography (see for instance [PDR11]):

We start from images $f(\boldsymbol{x},t)$, which are recorded during the mechanical excitation. These images can be B-scan data in US-imaging, MRI magnitude images, OCT images, or in principle, images from any modality [PDR11; WM04].

In a *quasi-static* experiment, there are two images: before and after the mechanical excitation from the exterior, which we denote as $f_1(\boldsymbol{x}) = f(\boldsymbol{x},t_1)$ and $f_2(\boldsymbol{x}) = f(\boldsymbol{x},t_2)$.

In the following, we derive the model for the continuous case, but later we specialize to the quasi-static case.

The most general model of continuity mechanics is the relation

$$f(\boldsymbol{x}(t),t) = \rho(t), \tag{6.2.1}$$

describing the change of intensity in a particle transported along the trajectory $\boldsymbol{x}(t)$. The displacement is then given by $\boldsymbol{u} = \dot{\boldsymbol{x}}(t)$. Taking the derivative in (6.2.1) and using $\frac{\partial \rho}{\partial t} + f\nabla\cdot\boldsymbol{u} = 0$ [Seg77], we obtain an equation for the displacement vector field:

$$\nabla f\cdot\boldsymbol{u} + f_t = -f\nabla\cdot\boldsymbol{u}. \tag{6.2.2}$$

In the practice of elastography, it is almost always assumed that the tissue is incompressible, satisfying $\nabla\cdot\boldsymbol{u} = 0$, as well as $\delta(t) = const.$

The common models in elastography therefore are based either on

$$f(\boldsymbol{x}(t),t) = const. \tag{6.2.3}$$

or on the linearization

$$\nabla f\cdot\boldsymbol{u} + f_t = 0\,, \tag{6.2.4}$$

which is also called the *optical flow constraint*.

A model such as (6.2.3) can serve as a basis for an *image registration* model to recover (also larger) displacements $\boldsymbol{u} = \dot{\boldsymbol{x}}(t)$ from f (see [Mod03] for general methods and for the special application [J.+05] for detection of the movement of the heart, e.g.). In general, these are computationally expensive.

An alternative to registration is *block matching* [Boh+00]. Additionally to (6.2.3), one assumes here that the displacement is constant in defined regions; using a target block, one compares the image patterns in subsequent frames by using a correlation measure.

Alternatives are *optical flow* methods [ZQM10]. These methods are based on (6.2.4). This is the method used and analysed in this article.

We now consider the variant (6.2.4) in the *quasi-static case*. Here we are calculating the spatial dependent flow $\boldsymbol{u}(\boldsymbol{x})$ only by solving:

$$\nabla f_1 \cdot \boldsymbol{u} + (f_2 - f_1) = 0\,. \tag{6.2.5}$$

The equation is underdetermined with respect to $\boldsymbol{u}$. Optical flow algorithms are designed to approximate a minimal norm solution $\boldsymbol{u}^\dagger$ of (6.2.5). For instance, the variational Horn-Schunck model [HS81], consisting in computing

$$\boldsymbol{u} = \arg\min_{\boldsymbol{v}} \|\nabla f_1 \cdot \boldsymbol{v} + (f_2 - f_1)\|^2_{L^2(\Omega)} + \lambda \int_\Omega |\nabla_{\boldsymbol{x}} \boldsymbol{v}|^2 \,\mathrm{d}\boldsymbol{x}\,, \tag{6.2.6}$$

approximates (for $\lambda \to 0$) a minimizer of the constrained optimization problem:

$$\int_\Omega |\nabla_{\boldsymbol{x}} \boldsymbol{v}|^2 \,\mathrm{d}\boldsymbol{x} \text{ subject to } \nabla f_1 \cdot \boldsymbol{v} = f_1 - f_2\,. \tag{6.2.7}$$

6.2.3 The Role of Texture in Motion Estimation

In ultrasound imaging and optical coherence tomography, texture is provided by patterns in the images referred to as *speckle*. These are correlated texture patterns which provide a signature of the points. Block-matching-type algorithms are therefore often called as *speckle tracking* algorithms [Boh+00; Pan+14]. Sometimes, any motion estimation in USE or OCE is comprehensively referred to as *speckle tracking* [RMM05; ZQM10].

In MRI, it was observed that part of tissue motion is invisible in magnitude images because of homogeneous regions. To overcome this limitation, artificial tags have been introduced in the image [PM92; Fu+11]. These make motion estimation possible in regions where no intensity is initially present.

Artificial speckle or texture introduction is a frequently used technique for deformation detection in material science. Here, often airbrush techniques are being used as a pre-processing step to correlation techniques [ZG01; Lec+06].

In the next section, we review photoacoustic imaging. In Section 6.4 we demonstrate that band-limitation of the measurement data creates a speckle-like texture pattern in photoacoustic image data.

6.3 Photoacoustic Imaging

Photoacoustic imaging (PAI) is among the most prominent coupled-physics techniques [AS12]. It operates with laser excitation and records acoustic pressure, as the coupled modality. We first review the imaging formation in PAI.

6.3.1 Mathematical Modeling

Commonly, in Photoacoustics, the wave equation is used to describe the propagation of the acoustic pressure p:

$$\begin{aligned} p_{tt} - \Delta_{\boldsymbol{x}} p &= I_t f, && \text{in } \mathbb{R}^n \times (0,T], \\ p &= 0, && \text{in } \mathbb{R}^n \times (-\infty,0). \end{aligned} \tag{6.3.1}$$

The function I models the laser excitation and is usually considered a time dependent δ-distribution. The function f represents the capability of the medium to transfer electromagnetic waves into pressure waves; f is material dependent and is visualized in photoacoustic imaging.

Details of deduction of (6.3.1) from the Euler equations and the diffusion equation of thermodynamics can be found for instance in [Sch+09].

If we assume the excitation to be perfectly focused in time (that is $I(t) = \delta(t)$), equation (6.3.1) can be reformulated as a homogeneous initial value problem [Sch+09]

$$\begin{aligned} p_{tt} - \Delta_{\boldsymbol{x}} p &= 0, && \text{in } \mathbb{R}^n \times (0,\infty), \\ p(t=0) &= f, && \text{in } \mathbb{R}^n, \\ p_t(t=0) &= 0, && \text{in } \mathbb{R}^n. \end{aligned} \tag{6.3.2}$$

This (direct) problem is well-posed under suitable smoothness assumptions on f (see, e.g., [Eva98]). We denote by

$$\mathcal{P}f(\boldsymbol{x},t) = p(\boldsymbol{x},t), \quad \boldsymbol{x} \in \mathbb{R}^n,\ t \in (0,\infty), \tag{6.3.3}$$

the operator that maps the initial pressure f to the solution of (6.3.2).

Remark 6.3.1: Since we want to apply a convolution to our solution p, we have to extend it to negative values of t in a way that the wave equation (6.3.2) is still fulfilled. We distinguish the causal extension $\mathcal{P}f = 0$ for $t < 0$ (that we denote again with the letter $\mathcal{P}$), and the even extension

$$\mathcal{P}_{even} f(\boldsymbol{x},t) := \begin{cases} \mathcal{P}f(\boldsymbol{x},t), & t \geq 0, \\ \mathcal{P}f(\boldsymbol{x},-t), & t < 0. \end{cases} \tag{6.3.4}$$

6.3.2 Photoacoustic Imaging as an Inverse Problem

In Photoacoustics, we assume the pressure to be measured on a surface Γ over time. The inverse problem now consists of reconstructing the initial pressure f in (6.3.2) from these data, ideally given as trace of the solution on Γ. For the sake of simplicity of notation,

we are denoting this operator by

$$\mathcal{P}f = p|_{\Gamma\times(0,\infty)} \tag{6.3.5}$$

as well. Here, $\mathcal{P}$ is mapping f to the trace of the solution p of (6.3.2) at the surface Γ. The *Photoacoustic inverse problem* consists in solving equation (6.3.5) for f.

This problem obtains a unique solution, provided Γ is a so-called uniqueness set (for a review over existing results see [KK08]). These uniqueness sets contain the case of a closed measurement surface surrounding the photoacoustic source.

For some of the most important simple geometrical shapes of closed manifolds Γ, there exist analytical reconstruction formulae of series expansion and/or filtered backprojection type (see again [KK08] and the references therein, for instance [**Nil97**; Nor80; NL81; Faw85; Ram85; Pal04; FR05; FHR07; ESS12]).

This paper focuses on the case where Γ is a sphere in $\mathbb{R}^2$ (circle) or $\mathbb{R}^3$. For photoacoustic reconstruction, we make use of the explicit filtered backprojection formulas established in [FR05; FHR07]. Since we will have to deal with initial sources not necessarily of compact support, we remark that a result in [ABK96] guarantees injectivity of the photoacoustic problem provided certain integrability conditions on the source hold. Particularly, the photoacoustic mapping is injective if and only if the source is L^p-integrable on the entire space, where $p \leq 2n/(n-1)$.

6.4 Photoacoustics with Band-Limited Data

We create speckle patterns computationally from photoacoustic data using band-limited measurements for back-projection and approximating the initial source f. To be more precise, instead of measuring the exact trace of the solution of (6.3.2) at Γ, we instead assume to measure the band-limited data $m = \phi *_t p$ (see Definition 6.4.3).

The mathematical background is an application of some results by Haltmeier [Hal11, pp. Lmm. 3.1] (see also [HSZ09b; HZ10]) to convolution kernels which do not necessarily have compact support. Before we state the theorem, we define the Radon und Fourier transform (based on [Hel11, p.1 ff]):

Definition 6.4.1 The Radon transform $\mathcal{R}\varphi(\theta, s)$ maps $\varphi(\boldsymbol{x})$ to its integrals over hyperplanes in $\mathbb{R}^n$ with distance $s \in \mathbb{R}$ to the origin and unit normal vector $\theta \in S^{n-1}$. Namely,

$$\mathcal{R}\varphi(\theta, s) = \int_{\theta\cdot\boldsymbol{y}=s} \varphi(\boldsymbol{y})d\boldsymbol{y}. \tag{6.4.1}$$

In the case $n = 1$, the Radon transform corresponds to the absolute value of the function. In the case where φ is rotationally symmetric, the Radon transform $\mathcal{R}\varphi$ is independent of θ. We can therefore write

$$\mathcal{R}\varphi(\theta, s) = \phi(s) \tag{6.4.2}$$

for a suitable, even function $\phi : \mathbb{R} \to \mathbb{R}$.

Definition 6.4.2 The n-dimensional Fourier transform $\widehat{\varphi}(\boldsymbol{\kappa})$ of φ is defined as

$$\widehat{\varphi}(\boldsymbol{\kappa}) = \frac{1}{(2\pi)^{n/2}} \int_{\mathbf{R}^n} \varphi(\boldsymbol{y}) e^{-\mathrm{i}\boldsymbol{y}\cdot\boldsymbol{\kappa}} d\boldsymbol{y}\,. \tag{6.4.3}$$

If not stated differently, the Fourier transform of a time-dependent function $q(\boldsymbol{x},t)$ is with respect to the time variable, i.e.

$$\widehat{q}(\boldsymbol{x},\kappa) = \frac{1}{\sqrt{2\pi}} \int_{\mathbb{R}} q(\boldsymbol{x},t) e^{-\mathrm{i}t\kappa} dt \,.$$

Definition 6.4.3 The n-dimensional convolution $f *_{\boldsymbol{x}} g$ is defined, as usual, by

$$f *_{\boldsymbol{x}} g(\boldsymbol{x}) = \int_{\mathbb{R}^n} f(\boldsymbol{y}) g(\boldsymbol{x}-\boldsymbol{y}) d\boldsymbol{y}\,, \tag{6.4.4}$$

where f, g functions from $\mathbb{R}^n$ to $\mathbb{R}$. The sub-index in $*_{\boldsymbol{x}}$ thereby clarifies the variable, in which the convolution is performed.

In a formal manner, the following theorem has been stated already by Haltmeier [Hal11]. However, there is a subtle difference to our work, which is that the convolution function Ψ has compact support in [Hal11, Lemma 3.1], which is not the case here.

Theorem 6.4.4 *Let $p = \mathcal{P}f$ be a solution of (6.3.3) with initial pressure $f \in H^1(\mathbb{R}^n)$, with compact support. Moreover, let $\Psi \in L^p(\mathbb{R}^n)$, for some p such that $1 \le p < n/(n-1)$, be radially symmetric, i.e., $\Psi(\boldsymbol{x}) = \psi(|\boldsymbol{x}|)$. Then*

$$(\mathcal{P}(\Psi *_{\boldsymbol{x}} f))(\boldsymbol{x},t) = (\mathcal{R}\Psi *_t \mathcal{P}_{\mathrm{even}} f)(\boldsymbol{x},t)\,, \tag{6.4.5}$$

for all $\boldsymbol{x} \in \mathbb{R}^n$, $t > 0$.

Under the assumptions of the theorem the proof is analogous to the proof in [Hal11, Lemma 3.1]. It employs that the Radon transform, in an *almost everywhere* sense, is injective on L^p-functions for $1 \le p < n/(n-1)$ [Sol87]. Note, however, that because of the non-compactness of the support of the function Ψ, the minimal smoothness assumptions on the imaging data f and the convolution kernel are not clarified so far, and are open to basic research.

For application of Theorem 6.4.4 to the measured, *causal* band-limited data, we need to give a relation to the data *even* in time, as they appear in the theorem. This relation is given in the following proposition:

Proposition 6.4.5 *Let $1 \le p < n/(n-1)$. Moreover, let $\Psi \in L^p(\mathbb{R}^n)$ be radially symmetric. Then (see (6.4.2)) $\phi(s) := \mathcal{R}\Psi(\theta,s)$ is even and independent of θ. Moreover, let*

$$m(\boldsymbol{x};t) = (\phi *_t \mathcal{P}f)(\boldsymbol{x};t) \quad \text{on } \Gamma \times (0,\infty)\,.$$

Then,

$$m_{even}(\boldsymbol{x},t) = (\phi *_t P_{even} f)(\boldsymbol{x},t) \quad \text{on } \Gamma \times (0,\infty)\,, \tag{6.4.6}$$

where $\boldsymbol{x} \in \Gamma, t \in (0,\infty)$ can be computed from the causal measurement data $m(\boldsymbol{x},t)$, via the Fourier relation

$$\widehat{m_{even}}(\boldsymbol{x},\kappa) = 2\mathrm{Re}\,(\widehat{m}(\boldsymbol{x},\kappa)) \quad \text{on } \Gamma \times (0,\infty)\,.$$

Proof: Let p denote the solution of (6.3.2). Since $p(\boldsymbol{x};t)$ is real-valued, it follows that

$$\widehat{p}(\boldsymbol{x},-\kappa) = \overline{\widehat{p}(\boldsymbol{x},\kappa)} \qquad \forall x \in \mathbb{R}^n, \kappa \in \mathbb{R}\,,$$

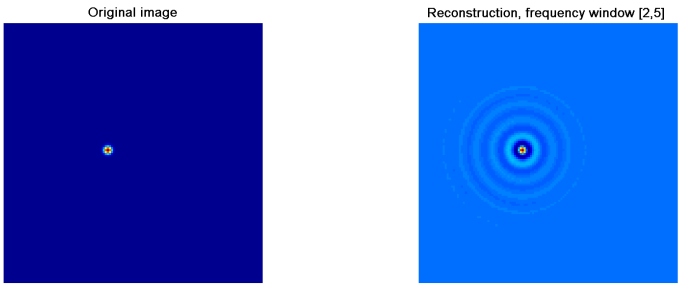

FIGURE 6.1: Point source (left) and textured reconstruction (right).

and therefore

$$\widehat{\mathcal{P}_{\text{even}} f}(\boldsymbol{x}, \kappa) = 2\,\text{Re}\,(\widehat{p}(\boldsymbol{x}, \kappa)) \qquad \forall \boldsymbol{x} \in \mathbb{R}^n, \kappa \in \mathbb{R}\,.$$

Thus, from (6.4.6) it follows that

$$\begin{aligned} \widehat{m_{\text{even}}}(\boldsymbol{x}, \kappa) &= \widehat{\phi}(\kappa) \widehat{\mathcal{P}_{\text{even}} f}(\boldsymbol{x}, \kappa) \\ &= \widehat{\phi}(\kappa)\, 2\,\text{Re}\left(\widehat{\mathcal{P} f}(\boldsymbol{x}, \kappa)\right) \\ &= 2\,\text{Re}\left(\widehat{\phi}(\kappa)\, \widehat{\mathcal{P} f}(\boldsymbol{x}, \kappa)\right) \\ &= 2\,\text{Re}\,(\widehat{m}(\boldsymbol{x}, \kappa)) \qquad \forall \boldsymbol{x} \in \Gamma, \forall \kappa \in \mathbb{R}, \end{aligned} \tag{6.4.7}$$

where in the third equality we use that $\widehat{\phi}$ is real-valued, since ϕ is a real-valued and even function. □ □

Proposition 6.4.5 gives a simple relation between convolved m_{even} and measurement data m. In fact Theorem 6.4.4 and Proposition 6.4.5 then show that

$$(\mathcal{P}(\Psi *_{\boldsymbol{x}} f))(\boldsymbol{x}, t) = (\mathcal{R}\Psi *_t \mathcal{P} f)_{\text{even}}(\boldsymbol{x}, t)\,, \tag{6.4.8}$$

which can be computed directly from the measurement data $\mathcal{P} f$.

6.5 PAI Elastography Using Texture Information

The results of Section 6.4 give the theoretical background on the influence of band-limitation of the measurement data on the photoacoustic imaging. In the following subsection we describe how to find pairs of filter functions ϕ and Ψ in practice. Moreover, we give an example of a pair of oscillating functions, that we use in what follows to create speckle-like patterns on photoacoustic images. The rest of the paper treats the case of two spatial dimensions. Since the theoretical considerations from Section 6.4 are valid in any spatial dimension, the application to 3D images works in complete analogy to the two-dimensional case described below.

6.5.1 Speckle Generation in 2D Photoacoustics

We assume to measure the bandpass data

$$m = \phi *_t \mathcal{P} f \,,$$

where

$$\phi(t) = \frac{2\sqrt{2}\cos(\kappa_0 t)\sin(at)}{\sqrt{\pi} t} \,, \tag{6.5.1}$$

is the Fourier transform of the bandpass filter:

$$\widehat{\phi}(\boldsymbol{x}, \kappa) = \chi_{[\kappa_{\min}, \kappa_{\max}]}(|\kappa|) \,. \tag{6.5.2}$$

Here $2a = \kappa_{\max} - \kappa_{\min}$ is the bandwidth and $\kappa_0 = \kappa_{\min} + a$ is the center frequency of the filter.

The results of Section 6.4 describe the equivalence relationship of the filter for the measurement data in time and a resulting filter in space for the imaging data. But since we actually want to compute this space filter explicitly, it is convenient to make use of the so-called *Fourier-slice* theorem for the Radon transform [Hel11, p.4][Sol87], that relates the Fourier transform of the Radon transform (in radial direction) to the Fourier transform of the image (in all spatial dimensions).

The corresponding point-spread function Ψ is given by

$$\Psi(\boldsymbol{x}) = \frac{\kappa_{\max} J_1(\kappa_{\max}|\boldsymbol{x}|) - \kappa_{\min} J_1(\kappa_{\min}|\boldsymbol{x}|)}{\sqrt{2\pi}|\boldsymbol{x}|} \,, \tag{6.5.3}$$

where J_1 is the first-kind Bessel function of order 1. By using an asymptotic estimate of J_1 for large arguments, it is easy to check that $\Psi \in L^p(\mathbb{R}^2)$ iff $p > 4/3$, which means that Ψ fulfils the integrability requirements demanded in Theorem 6.4.4. This ensures that the result actually applies to the used filter.

Note that the function pair (6.5.1),(6.5.3) does not have compact support, so that we really need the extension to L^p functions in Theorem 6.4.4.

Our suggested approach for texture generation then is this: We choose $\kappa_{\max}$ and $\kappa_{\min}$ to determine the impulse response ϕ. Then we compute m_{even} and solve the photoacoustic inverse problem with data m_{even}. Theorem 6.4.4 then ensures that this yields the perturbed reconstruction

$$f *_{\boldsymbol{x}} \Psi \,. \tag{6.5.4}$$

With the right choice of $\kappa_{\min}$ and $\kappa_{\max}$, this is a natural candidate for a textured variant of the photoacoustic data f.

In Figure 6.1, a point source and its photoacoustic reconstruction from band-limited data (i.e., data convolved with the impulse response in (6.5.1)) are shown. The oscillations introduced by the present band-limited photoacoustic reconstruction method introduce additional texture on the image.

In Figure 6.2, a sample containing homogeneous regions is shown, together with the effect of band-limitation for fixed $\kappa_{\max} = 10$, but varying values of $\kappa_{\min}$. In this more

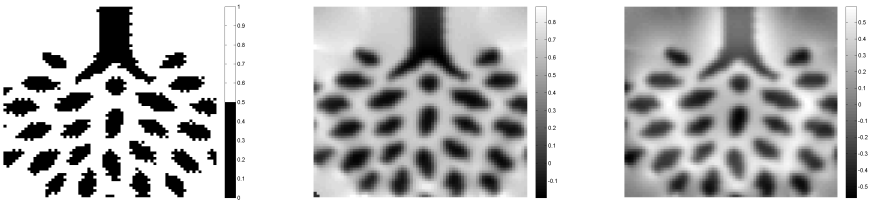

(A) no texture

(B) $\kappa_{\min} = 0$

(C) $\kappa_{\min} = 0.4$

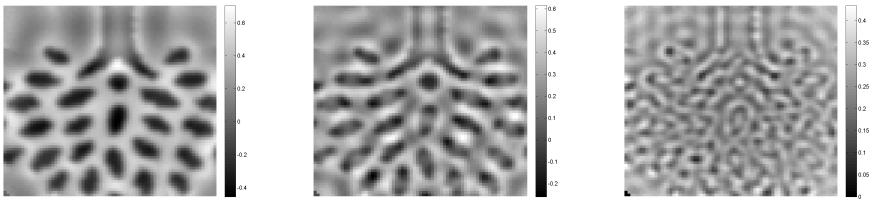

(D) $\kappa_{\min} = 0.8$

(E) $\kappa_{\min} = 1.2$

(F) $\kappa_{\min} = 1.8$

FIGURE 6.2: The filling-in-effect of the bandpass limitation: homogeneous regions are filled by the neighboring structures. Different versions computed with $\kappa_{\max} = 10$, with varying $\kappa_{\min}$.

complex sample, we see that the oscillations introduced by band-limitation serve to fill in homogeneous regions of the sample, and the structure of the edges is propagated locally around the shapes. This exhibits, particular for larger values, a texture pattern in the image. The use of this texture in estimating the optical flow between two photoacoustic images is investigated in the following sections.

6.5.2 Principle of PAI Elastography

In the previous subsection, we introduced a texture method for photoacoustic images. We now will study how motion estimation can be performed and amended by adding texture to photoacoustic images.

We emphasize that the initial pressure f introduced in (6.3.2) in the photoacoustic forward problem is spatially varying and can either represent the image before (i.e., f_1) or after (f_2) mechanical deformation as described in Subsection 6.2.2.

The main concept in the proposed method of *photoacoustic elastography* is to perform the following steps in the first step in Subsection 6.2.1:

a) record a PAI image f_1 using the texture-generating method

b) perturb the tissue using a mechanical source

c) record the perturbed configuration f_2 using the texture-generation method

We will now estimate the displacement $\boldsymbol{u}$ as in the second step in Subsection 6.2.1.

Remark 6.5.1: We emphasize that the convolution introduced in (6.5.4) commutes with rigid deformations: From (6.4.4), we have

$$f *_{\boldsymbol{x}} \Psi(\boldsymbol{x}) = \int_{\mathbf{R}^n} \Psi(\boldsymbol{y}) f(\boldsymbol{x}-\boldsymbol{y}) d\boldsymbol{y},$$

hence

$$\begin{aligned} f *_{\boldsymbol{x}} \Psi(\boldsymbol{x}-\boldsymbol{z}) &= \int_{\mathbf{R}^n} \Psi(\boldsymbol{y}) f(\boldsymbol{x}-\boldsymbol{y}-\boldsymbol{z}) d\boldsymbol{y} \\ &= (f(\boldsymbol{x}-\boldsymbol{z}) *_{\boldsymbol{x}} \Psi)(\boldsymbol{x}), \end{aligned}$$

which implies commutation with translations.

For a rotation $\boldsymbol{R}: \boldsymbol{x} \mapsto \boldsymbol{R}\boldsymbol{x}$, we have

$$f *_{\boldsymbol{x}} \Psi(\boldsymbol{R}\boldsymbol{x}) = \int_{\mathbf{R}^n} \Psi(\boldsymbol{y}) f(\boldsymbol{R}\boldsymbol{x}-\boldsymbol{y}) d\boldsymbol{y}\,. \tag{6.5.5}$$

On the other hand,

$$\begin{aligned} (f(\boldsymbol{R}\boldsymbol{x}) *_{\boldsymbol{x}} \Psi)(\boldsymbol{x}) &= \int_{\mathbf{R}^n} \Psi(\boldsymbol{y}) f(\boldsymbol{R}\boldsymbol{x}-\boldsymbol{R}\boldsymbol{y}) d\boldsymbol{y} \\ &= \int_{\mathbf{R}^n} \Psi(\boldsymbol{R}^{-1}\boldsymbol{z}) f(\boldsymbol{R}\boldsymbol{x}-\boldsymbol{z}) d\boldsymbol{z}\,. \end{aligned}$$

Due to rotation invariance of Ψ, we have that $\Psi(\boldsymbol{R}^{-1}\boldsymbol{y}) = \Psi(\boldsymbol{y})$, therefore we have the same result as on the right hand side of (6.5.5).

For any rigid motion, the texture created by our method behaves strictly as a material characteristic advected with the vector field.

One might conjecture that for non-linear deformations $\boldsymbol{u}$, the convolution does not commute with forward transport along $\boldsymbol{u}$. An example of the different variants is given in Figure 6.3 for simulated data and a non-linear vector field (later employed in Experiment 2). This is shown for two values of the band-width, $\kappa_{min} = 0.4$ and $\kappa_{min} = 1.8$

In the first picture, the image f is textured, and then transported. In the second picture, the image f is transported, then textured. The third picture shows the difference. In fact, for the deformations we used, this difference in the optical flow is not significant. This is shown in the experiments of the Section 6.7.

6.6 Feasibility of Texture Generation: A Regularization Point of View

The Horn-Schunck method (6.2.6) is a special instance of Tikhonov regularization [Sch+09, p. 3.1]. In this section, we show that adapting the Horn-Schunck method to textured images introduced in Section 6.4, yields a convergent regularization scheme in the sense of Proposition 6.4.5 below.

Note first that the optical flow equation (6.2.4), (6.2.5) is only well-defined if the image data f, f_1 and f_2, respectively, are smooth enough. This is typically not the case in photoacoustic imaging, because the images have high contrast, or in other words f_1

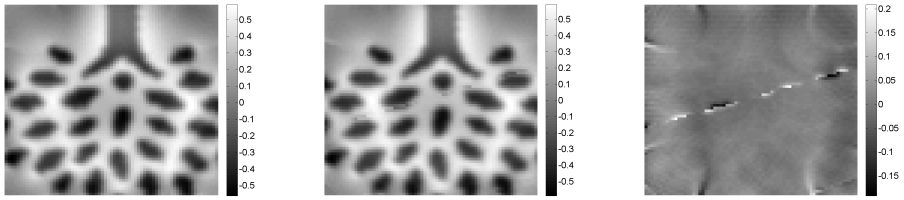

(A) Band 0.4 DT

(B) Band 0.4 TD

(C) Band 0.4 Diff. DT-TD

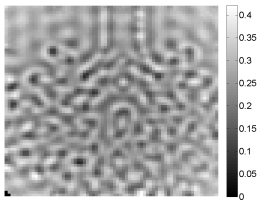

(D) Band 1.8 DT

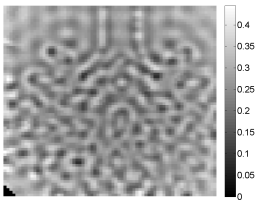

(E) Band 1.8 TD

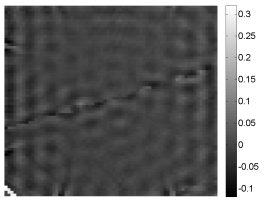

(F) Band 1.8 Diff. DT-TD

FIGURE 6.3: The difference of the order of deformation (D) and texturation (T), with texture from $\kappa_{\min} = 0.4$ (first row) and $\kappa_{\min} = 1.8$ (second row). See text for discussion.

and f_2 can have jump interfaces. In order to make the smoothness statement precise we have to formulate the optical flow equation in a function space setting.

6.6.1 Optical Flow Equation in a Function Space Setting

Our optical flow algorithm choice for elastography is the Horn-Schunck method (6.2.6). To make sure that it is well-posed we have to make sure ensure that (6.2.5) holds in an L^2-setting, or in other words that the optical flow residual is an element of $L^2(\Omega)$ and that the flow is in $H_0^1(\Omega)$.

To further proceed we introduce the parameter $0 < \varepsilon < 1$, and associate

$$\kappa_{\max} = 1/\varepsilon \text{ and } \kappa_{\min} = \varepsilon\,.$$

Accordingly we define the parametric family of functions,

$$\Psi_\varepsilon(\boldsymbol{x}) = \frac{\frac{1}{\varepsilon} J_1\left(\frac{1}{\varepsilon}|\boldsymbol{x}|\right) - \varepsilon J_1\left(\varepsilon|\boldsymbol{x}|\right)}{\sqrt{2\pi}|\boldsymbol{x}|}\,, \tag{6.6.1}$$

and introduce the operators

$$\begin{aligned} F &: H_0^1(\Omega) \to L^2(\Omega), \qquad \boldsymbol{u} \mapsto \nabla f_1 \cdot \boldsymbol{u}\,, \\ F_\varepsilon &: H_0^1(\Omega) \to L^2(\Omega), \qquad \boldsymbol{u} \mapsto \nabla (f_1 * \Psi_\varepsilon) \cdot \boldsymbol{u}\,. \end{aligned} \tag{6.6.2}$$

With these operators the quasi-static optical flow equation (6.2.5) can be rewritten as

$$F\boldsymbol{u} = f_1 - f_2 \,. \tag{6.6.3}$$

In contrast, if we base optical flow calculations on speckled data $f *_{\boldsymbol{x}} \Psi_\varepsilon$, then the according quasi-static optical flow equation (6.2.5) reads as follows:

$$F_\varepsilon \boldsymbol{u} = (f_1 - f_2) *_{\boldsymbol{x}} \Psi_\varepsilon \,. \tag{6.6.4}$$

In the following we prove that F and F_ε are well-defined and continuous:

Lemma 6.6.1 *Let $f_1 \in H_0^2(\Omega)$. Then the operators F, F_ε in (6.6.3), (6.6.4) are well-defined and bounded.*

Proof: Let $\boldsymbol{a} \in H_0^1(\Omega)$.

Then, by using the Euclidean Cauchy-Schwarz inequality, continuity of the the Sobolev-embedding from $H^1(\Omega)$ into $L^4(\Omega)$ and the Poincaré-Friedrichs inequality [AF03] it follows that:

$$\int_\Omega |\boldsymbol{a}\cdot\boldsymbol{u}|^2 d\boldsymbol{x} \le \int_\Omega |\boldsymbol{a}|^2|\boldsymbol{u}|^2 \le \left(\int_\Omega |\boldsymbol{a}|^4 \int_\Omega |\boldsymbol{u}|^4\right)^{1/2} \tag{6.6.5}$$

$$\le C_1 \|\boldsymbol{a}\|^2_{H^1(\Omega)} C_2 \|\boldsymbol{u}\|^2_{H^1(\Omega)} \le C \|\nabla \boldsymbol{u}\|^2_{L^2(\Omega)} \,. \tag{6.6.6}$$

Thus for either choice $\boldsymbol{a} = \nabla f_1$ and $\boldsymbol{a} = \nabla f_1 *_{\boldsymbol{x}} \Psi_\varepsilon$ the continuity assertion about F and F_ε follows.□ □

Moreover, in the following, we derive an estimate for the operator perturbation $\|F - F_\varepsilon\|$. Therefore, we use the following lemma:

Lemma 6.6.2 *Let Ψ_ε as defined in (6.6.1). Let $f_1, f_2 \in H_0^2(\Omega)$. Then the following the following statements hold:*

1. $\lim_{\varepsilon\to 0} \|\nabla (f_1 - f_1 *_{\boldsymbol{x}} \Psi_\varepsilon)\|^2_{H^1(\Omega)} = 0 \,.$
2. *The operator $F - F_\varepsilon$ is bounded, and the operator norm $\|F - F_\varepsilon\|$ goes to zero, as $\varepsilon \to 0$.*
3. *The L^2-distance $\|f_i - f_i *_{\boldsymbol{x}} \Psi_\varepsilon\|_{L^2(\mathbb{R}^n)} = \mathcal{O}(\varepsilon)$, with $i = 1,2$ as $\varepsilon \to 0$.*

Proof: The function $f_i \in H_0^2(\Omega)$, where $i = 1,2$, is identified with the function $f_i : \mathbb{R}^2 \to \mathbb{R}$, which is vanishing outside of Ω. With this extension it follows that

$$\|\nabla (f_1 - f_1 *_{\boldsymbol{x}} \Psi_\varepsilon)\|^2_{H^1(\Omega)} \le \|\nabla (f_1 - f_1 *_{\boldsymbol{x}} \Psi_\varepsilon)\|^2_{H^1(\mathbb{R}^2)} \,.$$

In the following let us denote by $\mathbb{B}_r$ a ball with radius r in $\mathbb{R}^2$. Then by using the equivalence of the Sobolev norm to the Fourier representation [AF03, p. 252], it follows

that

$$\begin{aligned}
&\|\nabla\left(f_1 - f_1 *_{\boldsymbol{x}} \Psi_\varepsilon\right)\|^2_{H^1(\mathbf{R}^2)} \\
\leq& C\|(1+|\boldsymbol{\xi}|)|\boldsymbol{\xi}||\widehat{f_1}|(1-\Psi_\varepsilon)\|^2_{L^2(\mathbf{R}^n)} \\
\leq& C\left(\int_{\mathbb{B}_\varepsilon}(1+|\boldsymbol{\xi}|^2)|\boldsymbol{\xi}|^2|\widehat{f_1}|^2 + \int_{\mathbf{R}^2\setminus\mathbb{B}_{\frac{1}{\varepsilon}}}(1+|\boldsymbol{\xi}|^2)|\boldsymbol{\xi}|^2|\widehat{f_1}|^2(1-\widehat{\Psi}_\varepsilon)\right),
\end{aligned} \tag{6.6.7}$$

by splitting the integral into an inner and outer part. Since we have $\widehat{\Psi} \equiv 1$ on the annulus $|\boldsymbol{\xi}| \in (\varepsilon, \frac{1}{\varepsilon})$, the integral vanishes in this area. Since $\widehat{f} \in L^\infty(\mathbb{R}^2)$ (due to the absolute integrability of f), the integrand in the first term can be bounded by $C(1+\varepsilon^2)\varepsilon^2$. This implies that the first integral is of order ε^4, as ε goes to zero. That is,

$$\begin{aligned}
&\|\nabla\left(f_1 - f_1 *_{\boldsymbol{x}} \Psi_\varepsilon\right)\|^2_{H^1(\Omega)} \\
&\leq C\int_{\mathbf{R}^2\setminus\mathbb{B}_{\frac{1}{\varepsilon}}}(1+|\boldsymbol{\xi}|^2)|\boldsymbol{\xi}|^2|\widehat{f_1}|^2(1-\widehat{\Psi}_\varepsilon) + \mathcal{O}(\varepsilon^4),
\end{aligned}$$

as $\varepsilon \to 0$. Due to the Lebesgue dominated convergence theorem and the assumption that $f \in H^2(\mathbb{R}^n)$, the remaining term converges to zero as well. This shows the first assertion. Statement two then follows immediately from (6.6.5) by choosing

$$\boldsymbol{a} = \nabla(f_1 - f_1 *_{\boldsymbol{x}} \Psi_\varepsilon).$$

To prove the last statement, we use Plancherel's identity and the fact that $f_i \in H^1_0(\Omega)$ to estimate

$$\begin{aligned}
&\|f_i - f_i *_{\boldsymbol{x}} \Psi_\varepsilon\|^2_{L^2} = \|\widehat{f_i} - \widehat{\Psi}_\varepsilon\widehat{f_i}\|^2_{L^2} = \int_{\mathbb{R}^2}|\widehat{f_i}|^2(1-\widehat{\Psi}_\varepsilon) \\
&= \int_{\mathbb{B}_\varepsilon}|\widehat{f_i}|^2 + \int_{\mathbb{R}^2\setminus\mathbb{B}_{\frac{1}{\varepsilon}}}|\widehat{f_i}|^2 \\
&\leq \int_{\mathbb{B}_\varepsilon}|\widehat{f_i}|^2 + \frac{1}{(1+1/\varepsilon^2)}\int_{\mathbb{R}^2\setminus\mathbb{B}_{\frac{1}{\varepsilon}}}(1+|\boldsymbol{\xi}|^2)|\widehat{f_i}|^2
\end{aligned} \tag{6.6.8}$$

Using the same argumentation as in (6.6.7), both terms are of order $\mathcal{O}(\varepsilon^2)$ as $\varepsilon \to 0$, which finishes the proof. □ □

Remark 6.6.3: In Lemma 6.6.2, we try to demand the minimal smoothness assumptions on f_1 necessary to guarantee the validity of statement 1. *Note that, analogous to the considerations in* (6.6.8)*, we could employ higher smoothness of f to receive a convergence rate estimate for $\|F - F_\varepsilon\|$.*

6.6.2 General Regularization Theory

In the following we review a classical results from regularization theory [Mor84, Thm.11, p. 21] (in a slightly simplified form). The referenced theorem says that Tikhonov regularization with an operator perturbation is a convergent regularization procedure.

Let $F : W \to Y$ be a bounded operator between Hilbert spaces W and Y. For y in the range of F a minimum-norm-solution $w^\dagger$ satisfies

$$w^\dagger = \operatorname{argmin}_W \{\|w\|_W : Fw = y\} .$$

Theorem 6.6.4 *Let $F, F_\varepsilon : W \to Y$ be bounded linear operators between Hilbert spaces W, Y with*

$$\|F - F_\varepsilon\| \to 0 . \tag{6.6.9}$$

Moreover, let $y \in R(F)$ and y^δ satisfy

$$\|y - y^\delta\| \to 0 . \tag{6.6.10}$$

Let Tikhonov regularized solutions according to F_ε be defined as

$$w^\delta_{\alpha,\varepsilon} := \arg\min \|F_\varepsilon w - y^\delta\|_Y^2 + \alpha \|w\|_W^2 . \tag{6.6.11}$$

Then there exists a parameter choice $\alpha := \alpha(\delta, \varepsilon)$ such that

$$\lim_{\delta \to 0, h \to 0} w^\delta_{\alpha,h} = w^\dagger . \tag{6.6.12}$$

6.6.3 Application of General Regularization Theory to the Optical Flow Problem

We apply the general Theorem 6.6.4 to Horn-Schunck regularization. To establish the coherence we take $W = H_0^1(\Omega), Y = L^2(\Omega)$ and F, F_ε as in (6.6.3) and (6.6.4). Note that according to Lemma 6.6.2, we have that $F_\varepsilon \to F$. We set

$$\begin{aligned} &w = \mathbf{u}, \qquad y = f_2 - f_1, \qquad \delta = \varepsilon, \\ &y^\delta = (f_2 - f_1) *_{\boldsymbol{x}} \Psi_\varepsilon \to y . \end{aligned}$$

Therefore, with $\varepsilon \to 0$, both the model perturbation condition (6.6.9) as well as the data perturbation condition (6.6.10) hold.

Define now $\boldsymbol{u}_{\alpha,\varepsilon}$ as the regularized solution (6.6.11) for our case:

$$\boldsymbol{u}_{\alpha,\varepsilon} := \arg\min_{\boldsymbol{v}} \|\nabla(f_1 * \Psi_\varepsilon) \cdot \boldsymbol{v} - (f_2 - f_1) * \Psi_\varepsilon\|_{L^2}^2 + \alpha \|\boldsymbol{v}\|_{H_0^1}^2 . \tag{6.6.13}$$

Now we easily derive that the minimizer according (6.6.13) provides a convergent regularization scheme:

Corollary 6.6.5 *For given $f_1, f_2 \in H_0^2(\Omega)$ let there exist a solution $\mathbf{u}$ of (6.2.5). Then there exists a solution $\mathbf{u}^\dagger$ of (6.2.7) (i.e. it is a minimum norm solution).*

Moreover, let $\boldsymbol{u}_{\alpha,\varepsilon}$ be the minimizer of (6.6.13). Then there exists a parameter choice $\alpha = \alpha(\varepsilon)$, such that

$$\lim_{\varepsilon \to 0^+} \boldsymbol{u}_{\alpha,\varepsilon} = \boldsymbol{u}^\dagger . \tag{6.6.14}$$

Remark 6.6.6: The above results show that if the input image sequence for the optical flow is in $H_0^2(\Omega)$, then the Horn-Schunck regularized solutions with band-filtered data approximate the solution of the constrained optimization problem (6.2.6) and (6.2.7) if

the band tends to cover the whole frequency range. In practice, a limited frequency range gives already quite accurate reconstructions. On the other hand we also have outlined that image data smoothing is indispensable for optical flow computations because the optical flow equation is not well-defined when discontinuities or singularities appear in the images.

6.7 Experiments

There are many different varieties of experiments one can perform. In this section, we present a first selection, using structures which contain homogeneous regions, similar to vascular structures.

6.7.1 Simulations

We simulate photoacoustic measurement data using the k-wave toolbox [TC10]. For reconstruction, we use a filtered back-projection algorithm. Displacement vector fields have been simulated using the FEM and mesh-generating packages GetDP and Gmsh [Dul+98; GR09].

6.7.2 Material, Displacement and Parameters

The synthetic material was chosen to exhibit homogeneous regions surrounded by edges. In each experiment, we evaluated a rigid deformation and a non-rigid deformation.

In Experiments 1 and 2, we use a tree structure designed by Brian Hurshman and licensed under CC BY 3.0[1].

6.7.3 Texture Modes

We compare the proposed texture creation in (6.5.4) to different alternative versions of filling in homogeneous regions in the image data. To this purpose, we choose one the following texture operators T. We give the different abbreviations we use for these texture modes in Table 6.1, Table 6.2, Table 6.3.

For the band-limitation-induced texture in (6.5.4), we set $\kappa_{\max} = 10$, and compare $\Psi_{\kappa min}$ for different values of $\kappa_{\min}$, precisely we compare

$$T: \qquad f \mapsto f * \Psi_{0.4} \tag{6.7.1}$$

which is referred to as *Band 0.4*, and

$$T: \qquad f \mapsto f * \Psi_{1.8} \tag{6.7.2}$$

which is referred to as *Band 1.8*.

Other possible operations on the image to fill in homogeneous regions are:

$$T: \qquad f \mapsto f + r \tag{6.7.3}$$

[1] http://thenounproject.com/term/tree/16622/

Texture Mode	AAE	AEEabs	AEErel	s-warp	o-warp
none	0.1780	0.0617	2.9980	0.4886	0.4886
Gauss 0.3 SW	0.1830	0.0628	3.0553	0.5471	0.4886
Band FBP 0.4	0.0905	0.0135	0.6583	0.1285	0.1821
Band FBP 0.4 SW	0.0882	0.0141	0.6909	0.1298	0.1958
Band FBP 1.8	**0.0461**	0.0190	0.9233	0.0538	0.2313
Band FBP 1.8 SW	0.1217	0.0184	0.8933	0.0536	0.2313
Gauss Conv 3x3	0.1730	0.0544	2.6470	0.4722	0.4886
Gauss Conv 3x3 SW	0.1731	0.0545	2.6480	0.4723	0.4863
Aver Conv 3x3	0.1632	0.0411	1.9985	0.3997	0.4595
Aver Conv 3x3 SW	0.1641	0.0417	2.0298	0.4036	0.4613
SaltPepper 0.1	0.2036	0.0051	0.2473	0.3961	0.0715
SaltPepper 0.1 SW	0.0851	0.0196	0.9552	0.4519	0.2536

TABLE 6.1: Different texture modes for Experiment 2, with 10% noise, $\lambda = 11.2202$ (see also Figure 6.6)

where r is Gaussian random noise of 30 %, abbreviated as *Gaussian 0.3*;

$$T: \qquad f \mapsto f * \sigma \tag{6.7.4}$$

where σ is a Gauss kernel of size $3x3$ pixels, abbreviated as *Gauss Conv 3x3*;

$$T: \qquad f \mapsto f * \chi \tag{6.7.5}$$

where χ is constant with $\mathrm{supp}(\chi)$ being a rectangle of pixel length 3, with $\int_\Omega \chi = 1$, referred to as *Aver Conv 3x3*;

$$T: \qquad f \mapsto SP(f) \tag{6.7.6}$$

where SP is Salt and Pepper noise applied to the image with parameter $p = 0.1$. This is referred to as *Salt and Pepper 0.1*.

The baseline condition, with which these texture variants are compared, is taking the original image with no texture at all, that is

$$T: \qquad f \mapsto f, \tag{6.7.7}$$

abbreviated as *none* in the tables.

In Table 6.2, Table 6.3, the choices for T in (6.7.1), (6.7.2), (6.7.7), (6.7.3) are compared, along with different variants to mix them with texture, specified below in (6.7.8), (6.7.9).

In Table 6.1, the results for all choices of T outlined above are compared.

6.7.4 Deformation

By forward-projecting and interpolating, we compute, for image data f, the deformed image $W(f, \boldsymbol{u})$, for which

$$W(f, \boldsymbol{u})(\boldsymbol{x} + \boldsymbol{u}(\boldsymbol{x})) = f(\boldsymbol{x})$$

holds.

For computing the data for the optical flow computation, the preferred choice follows principle Subsection 6.5.2, first applying the deformation, then the texture. Therefore we set

$$f_1 = T(f)$$

as well as

$$f_2 = T(W(f, \boldsymbol{u})). \tag{6.7.8}$$

Alternatively, we compare these with violating principle Subsection 6.5.2, first applying the texture, then deforming the image:

$$f_2 = W(T(f), \boldsymbol{u}). \tag{6.7.9}$$

The latter choice will be referred to with the letters DT in Table 6.1, Table 6.2, Table 6.3.

We also define

$$f_1^O = f(\boldsymbol{x}), \qquad f_2^O = W(f, \boldsymbol{u}). \tag{6.7.10}$$

for the validation.

6.7.5 Optical Flow Computation

With f_1 and f_2 determined as above, we compute

$$\boldsymbol{u} = \arg\min_{\boldsymbol{v}} \|\nabla Q(f_1) \cdot \boldsymbol{v} - (Q(f_2) - Q(f_1))\|_{L^2}^2 + \alpha \|\boldsymbol{v}\|_{H_0^1} . \tag{6.7.11}$$

Here, we apply

$$Q : f \mapsto f + r,$$

with r being additive Gaussian noise calibrated to 10 % of the maximum value of f.

This procedure has been applied to all results in Table 6.1, Table 6.2 and Table 6.3. – The effect of noise addition to texture is studied separately for the case of Experiment 2 (see Figure 6.4).

6.7.6 Validation

The field which is computed with the optical flow algorithm should approximately match the correct motion field. In order to study how PAI and textured PAI images behave under mechanical deformations, we adopt the following validation procedure to compare the computed vector field with *ground-truth* data:

Synthetic Data Verification

- Choose a particular vector field $\boldsymbol{u}_0$, as well as a reference image f_1
- Choose a texture method T
- Compute f_1, f_2 as in subsection Subsection 6.7.4
- Compute the optical flow $\boldsymbol{u}(\boldsymbol{x})$ as in (6.7.11)
- Compare the result $\boldsymbol{u}$ against the ground-truth vector field $\boldsymbol{u}_0$

Error Measures To compare the computed flows produced to the ground truth field, we use the angular and distance error, and to assess the prediction quality of the flow,

we calculate the warping error. To define these error measures, write

$$\boldsymbol{u}_0(\boldsymbol{x}) = r_0(\boldsymbol{x})\, e^{\mathrm{i}\varphi_0(\boldsymbol{x})}$$
$$\boldsymbol{u}(\boldsymbol{x}) = r(\boldsymbol{x})\, e^{\mathrm{i}\varphi(\boldsymbol{x})}.$$

Then we define the

- average angular error (AAE)

$$\int_\Omega |\varphi(\boldsymbol{x}) - \varphi_0(\boldsymbol{x})| d\boldsymbol{x}$$

- average endpoint error (AEE)

$$\int_\Omega \|\boldsymbol{u} - \boldsymbol{u}_0\| d\boldsymbol{x}$$

- average relative endpoint error (AEErel)

$$\int_\Omega \frac{1}{\|\boldsymbol{u}_0\|} \|\boldsymbol{u} - \boldsymbol{u}_0\| d\boldsymbol{x}$$

- the warping error w.r.t. the textured images (s-warp)

$$\int_\Omega \|f_2(\boldsymbol{x}) - W(f_1, \boldsymbol{u}))\| d\boldsymbol{x},$$

- the warping error w.r.t. the original images (o-warp)

$$\int_\Omega \|W(f, \boldsymbol{u}_0)(\boldsymbol{x}) - W(f, \boldsymbol{u})\| d\boldsymbol{x}\,.$$

6.8 Discussion

As mentioned in the introduction, elastography often relies on speckle tracking methods, including correlation techniques and optical flow. It is clear that such methods have a problem with homogeneous regions. As for the optical flow, this can be seen from (6.2.4), where the data term for homogeneous regions provides no information at all.

In Experiments 1-4, we used several pieces of synthetic data showing homogeneous regions and investigated the effect of the homogeneity in several regions of the data (see Figs. 6.5a- 6.8a).

The visualization of the computed motion fields in Figs. 6.5c, 6.6c, 6.7c and 6.8c shows aberrations from the respective ground truth fields. Comparing the values for the angular, distance and warping errors in Table 6.2 to Table 6.3 shows these aberrations, if one restricts to the untextured original images.

We then applied the texture generation methods introduced in Section 6.5. The results in section Section 6.7 show that addition of texture is able to alleviate this problem

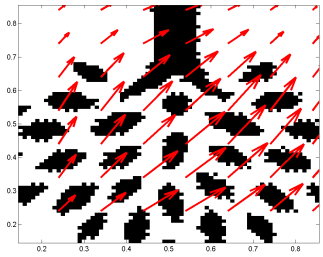

(A)
none +0% noise

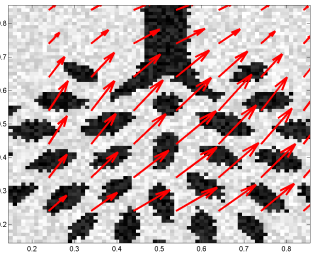

(B)
none + 30% noise

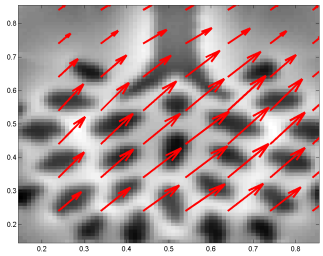

(C)
Band 0.4 + 0% noise

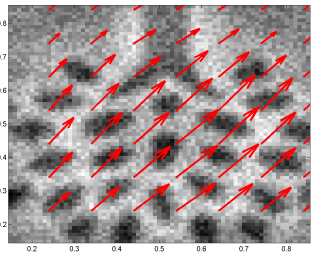

(D)
Band 0.4 + 30% noise

Texture Mode	AAE	AEEabs	AEErel	Warping
none + 0% noise	0.2499	0.0445	3.3232	0.3739
none + 5% noise	0.2494	0.0445	3.3233	0.3847
none + 10% noise	0.2492	0.0444	3.3199	0.3949
none + 20% noise	0.2515	0.0445	3.3229	0.4166
none + 30% noise	0.2493	0.0445	3.3270	0.4369
Band 0.4 + 0% noise	0.1880	0.0101	0.7548	0.0737
Band 0.4 + 5% noise	0.1876	0.0101	0.7546	0.0803
Band 0.4 + 10% noise	0.1883	0.0101	0.7560	0.0928
Band 0.4 + 20% noise	0.1929	0.0101	0.7583	0.1224
Band 0.4 + 30% noise	0.1825	0.0101	0.7522	0.1560

(E) Errors for $\lambda = 12.5893$

FIGURE 6.4: Comparision of different noise levels in Experiment 1 (see also Figure 6.5), the average over 10 experiments has been taken

of homogeneous regions to a considerable amount. The effect shows up in the different error types.

For the specimens we used, the angular error decreases about 20-30 % compared to the original error, and in extreme cases the decrease is as high as 75 % (as seen from Table Table 6.2). As seen from Figs. 6.5h- 6.8h, where the errors were plotted as a function of the regularization parameters, the distance error reaches its minimum in the textured variant at lower regularization values than the original data. In this context, we

note that the angular error is a monotonically increasing function of the regularization parameters in the cases we investigated. In some cases (as seen from Fig. 6.5h and Fig. 6.7h), the textured versions give also a lower distance error for the optimal regularization value; in other cases, with the motion estimation we used, the distance error is about the same magnitude as in the original versions.

The fact that the displacement estimation using the texture-method results in a vector field with optimum distance error at smaller regularization values (therefore also allowing a smaller angular error) points at the fact that the texture variant itself acts like a regularizer.

The optimum frequency windows for the texture generating method differ for the rigid and the non-rigid deformations we used. Whereas for the rigid deformations, the window with $\kappa_{\min} = 0.4$ gave best results, the non-rigid deformations best results with $\kappa_{\min} = 1.8$.

The possible non-commutation, which we mentioned in the Remark of Subsection 6.5.2, does not influence the result of the optical flow computations in a significant way, as seen from Table 6.2-Table 6.3.

The results are relatively robust to noise, as seen from Figure 6.4. While there are changes up to one tenth in the angular error, the band-pass-filtered images perform better than the original images, even with addition of 30% noise.

Notice that, in Experiments 1-4, we studied the addition of noise to a static image and then deformed it. This does not give a significant change in the accuracy of the optical flow (see Table 6.2 and Table 6.3). See also Table 6.1 for other results in that direction.

The effect of adding texture seems to come from a filling-in-effect in the optical flow equation (6.2.4). Although the regularization term is responsible for such an interpolation usually, here this filling-in-effect originates from the data term; the function Ψ seems to propagate the information from within the objects out across the edges and boundaries. This seems also to alleviate the aperture problem in optical flow, as the new texture creates also new gradients around edges. This may account for the lessening of the angular error.

Overall, the results point at the phenomenon that an effect which has deteriorating the image quality in one contrast (here the photoacoustic contrast) can have an advantageous effect on another contrast (here the mechanical contrast, which is inherent in the displacement $\boldsymbol{u}$).

6.9 Conclusion

We studied the topic of texture generation in photoacoustics, and applied bandwidth filter techniques for generating such texture in the reconstructed images. This kind of texture was mathematically characterized. Then we tested an application of the PAI texture for elastography purposes. It turned out that the texture generation technique has the potential to fill in otherwise untextured regions. The displacements can be better measured then, making photoacoustic elastography viable.

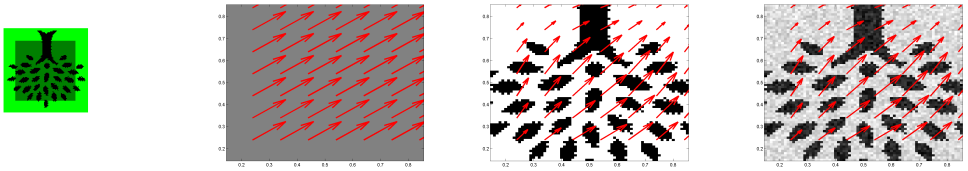

(A) Visualized mask

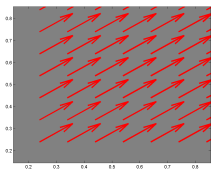

(B) Ground truth

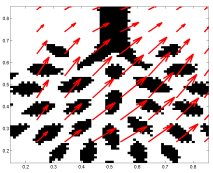

(C) none

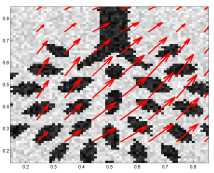

(D) Gauss 0.3 SW

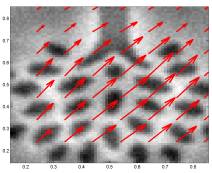

(E) Band 0.4

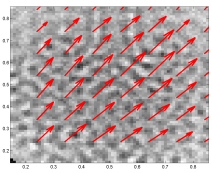

(F) Band 1.8

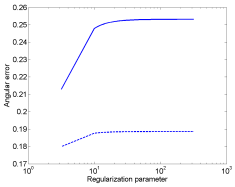

(G) Angular error

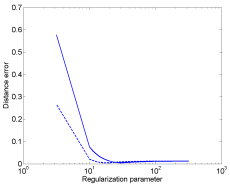

(H) Distance error

FIGURE 6.5: (Experiment 1) (c)-(f): Computed vector fields. (g)-(h): Different error measures for regularization parameter $10^{-3} \leq \lambda \leq 10^3$, full line: original data; dashed line: Band-limitation texture $\kappa = 0.4$

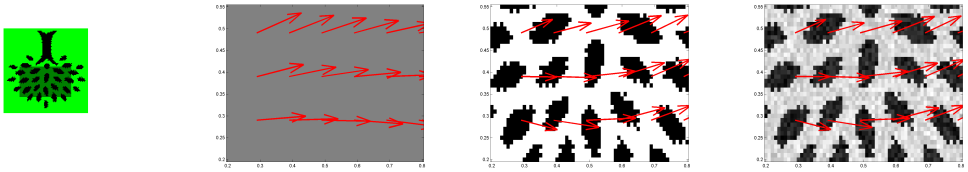

(A) Visualized mask

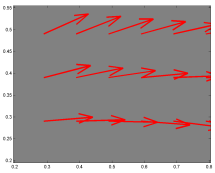

(B) Ground truth

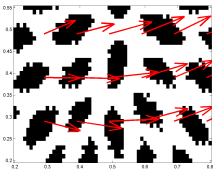

(C) none

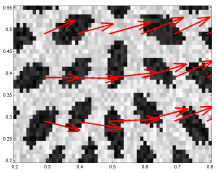

(D) Gauss 0.3 SW

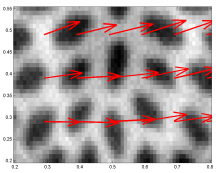

(E) Band 0.4

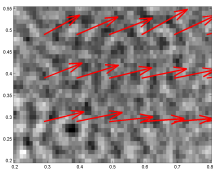

(F) Band 1.8

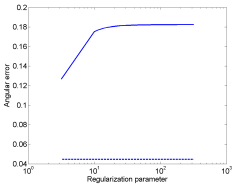

(G) Angular error

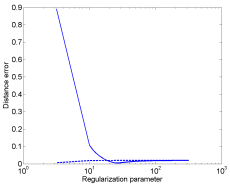

(H) Distance error

FIGURE 6.6: (Experiment 2) Different error measures for regularization parameter $10^{-3} \leq \lambda \leq 10^3$, full line: original data; dashed line: Band-limitation texture $\kappa = 1.8$

Acknowledgement

We thank Joyce McLaughlin, Paul Beard and Ben Cox for helpful discussions and express our gratitude to the referees for their stimulating remarks. We acknowledge support

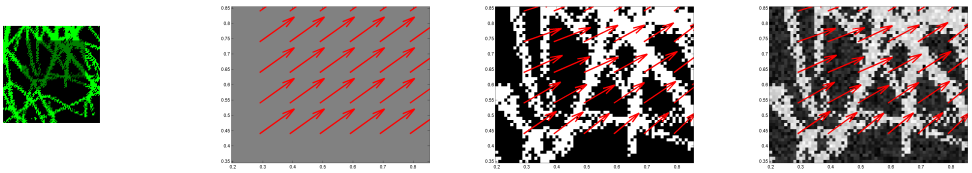

(A) Visualized mask

(B) Ground truth

(C) none

(D) Gauss 0.3 SW

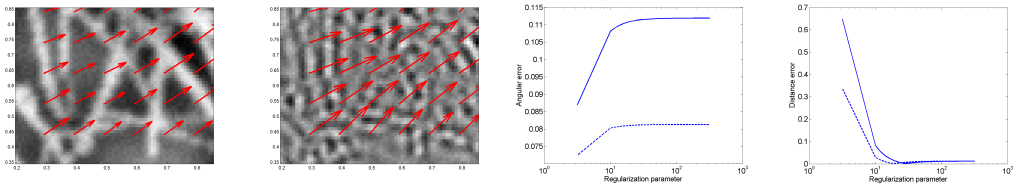

(E) Band 0.4

(F) Band 1.8

(G) Angular error

(H) Distance error

FIGURE 6.7: (Experiment 3) (c)-(f): Computed vector fields for $\lambda = 12.5893$. (g)-(h): Different error measures for regularization parameter $10^{-3} \leq \lambda \leq 10^{3}$, full line: original data; dashed line: Band-limitation texture $\kappa = 0.4$

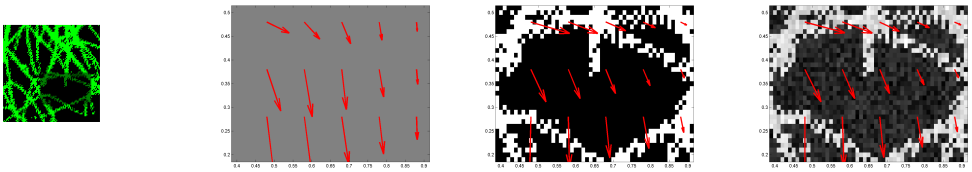

(A) Visualized mask

(B) Ground truth

(C) none

(D) Gauss 0.3 SW

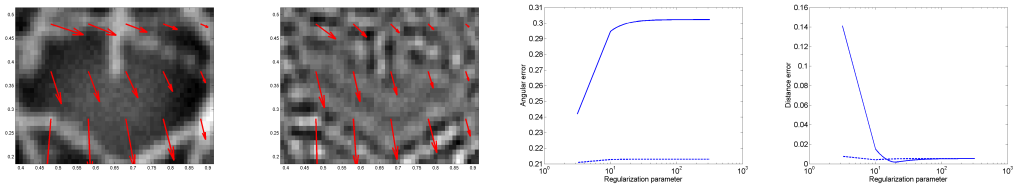

(E) Band 0.4

(F) Band 1.8

(G) Angular error

(H) Distance error

FIGURE 6.8: (Experiment 4) Different error measures for regularization parameter $10^{-3} \leq \lambda \leq 10^{3}$, full line: original data; dashed line: Band-limitation texture $\kappa = 1.8$

from the Austrian Science Fund (FWF) in projects S10505-N20 and P26687-N25.

TABLE 6.2: Experiments 1 and 2: Error analysis

(A) Rigid experiment, $\lambda = 12.5893$ (see Figure 6.5)

Texture Mode	AAE	AEEabs	AEErel	Warping
none	0.2499	0.0445	3.3232	0.3739
Gauss 0.3 SW	0.2429	0.0448	3.3480	0.4391
Gauss 0.1 noise	0.2500	0.0447	3.3386	0.3970
Band 0.4	0.1962	0.0105	0.7838	0.0945
Band 1.8	0.2344	0.0114	0.8531	0.0434

(B) Non-rigid experiment, $\lambda = 12.5893$ (see Figure 6.6)

Texture Mode	AAE	AEEabs	AEErel	Warping
none	0.1780	0.0617	2.9980	0.4886
Gauss 0.3 SW	0.1761	0.0620	3.0145	0.5393
Gauss 0.1 noise	0.1778	0.0617	3.0013	0.5060
Band 0.4	0.0913	0.0135	0.6607	0.1309
Band 1.8	0.1188	0.0190	0.9231	0.0552

TABLE 6.3: Experiments 3 and 4: Error analysis

(A) Rigid experiment, $\lambda = 11.2202$ (see Figure 6.7)

Texture Mode	AAE	AEEabs	AEErel	Warping
none	0.1089	0.0635	4.7460	0.4382
Gauss 0.3 SW	0.1106	0.0637	4.7639	0.4991
Gauss 0.1 noise	0.1084	0.0636	4.7567	0.4580
Band 0.4	0.0805	0.0214	1.5985	0.1829
Band 1.8	0.1313	0.0093	0.6966	0.0556

(B) Non-rigid experiment, $\lambda = 11.2202$ (see Figure 6.8)

Texture Mode	AAE	AEEabs	AEErel	Warping
none	0.2962	0.0112	1.3676	0.2053
Gauss 0.3 SW	0.2975	0.0111	1.3577	0.2795
Gauss 0.1 noise	0.3017	0.0114	1.3969	0.2298
Band 0.4	0.3259	0.0024	0.3063	0.0388
Band 1.8	0.2128	0.0044	0.5320	0.0283

Part III

Appendices

A

Derivation of a Reconstruction Formula for Planar Measurements

We follow here the lecture notes [SM15] that give an elementary computation in 2D. The approach can be transferred to any spatial dimension in a straightforward way: Assume that $\Gamma = \{x_n = 0\}$ and that $\mathrm{supp}(f)$ is on one side of Γ, say w.l.o.g. $\mathrm{supp}(f) \subset \{x_n > 0\}$. Therefore, Take the Fourier transform of y w.r.t. the spatial coordinate x of

$$y''(x,t) - \Delta y$$

to see that

$$\widehat{y}''(k,t) + |k|^2 \widehat{y}(k,t) = 0, \quad \forall k \in \mathbb{R}^2, t > 0\,,$$

where

$$\widehat{y}(k,t) = \frac{1}{(2\pi)^{n/2)}} \int_{\mathbb{R}^n} \mathrm{e}^{\mathrm{i}k\cdot x} y(x,t) dx$$

denotes the Fourier transform of y with respect to the spatial coordinates. This is an ODE with solution

$$\widehat{y}(k,t) = C_1(k)\mathrm{e}^{\mathrm{i}|k|t} + C_2(k)\mathrm{e}^{-\mathrm{i}|k|t}, \quad \forall k \in \mathbb{R}^2, t > 0\,.$$

By employing the initial conditions, it follows that

$$\widehat{y}(k,t) = \frac{1}{2}\widehat{f}(k)\left(\mathrm{e}^{\mathrm{i}|k|t} + \mathrm{e}^{-\mathrm{i}|k|t}\right), \quad \forall k \in \mathbb{R}^2, t > 0\,.$$

Now note that $\frac{1}{2}\left(\mathrm{e}^{\mathrm{i}|k|t} + \mathrm{e}^{-\mathrm{i}|k|t}\right) = \cos(|k|t)$. By using the abbreviations $\tilde{k} := (k_1, \ldots, k_{n-1})$ $\tilde{x} := (x_1, \ldots, x_{n-1})$ and employing the inverse Fourier transform for the spatial dimensions, the data $m(\tilde{x},t) = y(\tilde{x},t)$ can be written as

$$m(\tilde{x},t) = \frac{1}{(2\pi)^{n/2}} \int_{\mathbb{R}^n} \mathrm{e}^{-\mathrm{i}\tilde{k}\cdot\tilde{x}} \cos(|k|t)\widehat{f}(k) dk\,.$$

At this point, we introduce the one-to-one transform

$$\begin{aligned} &S : \mathbb{R}^n \to A := \{(\tilde{k},\omega) : |\tilde{k}| \le |\omega|, \omega \in \mathbb{R}\}\,,\\ &(\tilde{k}, k_n) \to (\tilde{k},\omega)\,, \end{aligned}$$

where $\omega = \mathrm{sgn}(k_n)\sqrt{|\tilde{k}|^2 + k_n^2}$. Note that $|\omega| = |k|$. In addition, we define

$$g(\tilde{k},\omega) = \begin{cases} \widehat{f}(\tilde{k},w)\sqrt{\omega^2 - |\tilde{k}|^2}\dfrac{|\omega|}{\sqrt{\omega^2 - |\tilde{k}|^2}} & \text{for } (\tilde{k},\omega) \in A\,,\\ 0 & \text{else}\,. \end{cases}$$

A change of coordinates by application of S gives

$$m(\tilde{x},t) = \frac{1}{(2\pi)^{n/2}} \int_{\mathbf{R}^n} \mathrm{e}^{-\mathrm{i}(\tilde{k}\cdot\tilde{x})} \cos(\omega t) g(\tilde{k},\omega) d\omega d\tilde{k} \,.$$

Since f is causal in the last coordinate, it is $\widehat{f}(\cdot,k_n) = \overline{\widehat{f}(\cdot,-k_n)}$, which also holds for g. Thus,

$$\int_{\mathbf{R}} \cos(\omega t) g(\tilde{k},\omega) d\omega = \int_{\mathbf{R}} \mathrm{e}^{-\mathrm{i}\omega t} \mathcal{R}\left(g(\tilde{k},\omega)\right) d\omega \,.$$

It follows (see (6.4.7)) that

$$2m(\tilde{x},t) = \frac{1}{(2\pi)^{n/2}} \int_{\mathbf{R}^n} \mathrm{e}^{-\mathrm{i}\tilde{k}\cdot\tilde{x}-\mathrm{i}\omega t} g(\tilde{k},\omega) d\omega d\tilde{k}\,, \quad t>0\,.$$

This can be inverted in a straight-forward way by employing the $n-1$ dimensional inverse Fourier transform to the first argument and the 1D inverse Fourier transform to the last argument. Now note that $\frac{\omega}{\sqrt{\omega^2-|\tilde{k}|^2}} = \frac{\sqrt{|\tilde{k}|^2+k_n^2}}{k_n}$. One can easily follow that

$$\widehat{f}(\tilde{k},k_n) = \frac{2|k_n|}{\sqrt{|\tilde{k}|^2+k_n^2}} \widehat{m}\left(\tilde{k}, \mathrm{sgn}(k_n)\sqrt{|\tilde{k}|^2+k_n^2}\right), \quad \forall k \in \mathbb{R}^n \,. \tag{A.0.1}$$

B

Zusammenfassung (Deutsch)

Photoakustik-Tomographie ist ein sich derzeit in Entwicklung befindliches, bildgebendes Verfahren, dessen potentielle Anwendungen klinische und pre-klinische Diagnose, sowie zerstörungsfreies Testen in Industrieprozessen umfassen. Eine durch Laserlicht induzierte Ultraschallwelle, in der Parameter von diagnostischem Wert kodiert sind, wird außerhalb des Objekts gemessen. Das Photoakustik-Problem besteht in der Rekonstruktion der Parameter aus den Messdaten. Die vorliegende Doktorarbeit beschäftigt sich mit der Photoakustik-Rekonstruktion der absorbierten elektromagnetischen Energie in Situationen, in denen die analytischen Standard-Methoden entweder gar nicht anwendbar sind, oder ihre Diskretisierung besondere Beachtung erfordert.

Im Fall von einem, oder sogar 2 variierenden akustischen Parametern ist das oftmals verwendete Standard-Rekonstruktionsverfahren das sogenannte *Time Reversal*. Hierbei wird ein Anfangsrandwertproblem der Wellengleichung rückwärts in der Zeit gelöst. Die Messdaten dienen hierbei als Dirichlet Randdaten, außerdem werden üblicherweise verschwindende Anfangsdaten gefordert (was zu einem Approximationsfehler führt).

Im Gegensatz dazu wird in dieser Arbeit das Photoakustik-Problem als Operatorgleichung formuliert. Das Landweber Iterationsverfahren erlaubt die stabile Rekonstruktion einer regularisierten Lösung. Anders als bei Time Reversal liefert solch ein Verfahren Konvergenz zu einer regularisierten Lösung auch im Falle von verrauschten Daten oder bei einer ungünstigen Ausbreitung der Singularitäten, verursacht durch sogenanntes *Trapping* der Schallgeschwindigkeit. Die Rückpropagation, in gewissem Sinne gemeinsames Merkmal aller hier verwendeten Rekonstruktionsmethoden, ist jetzt im adjungierten Operator enkodiert. Die Anwendung desselben erfordert die Lösung eines Transmissionsproblems für die Wellengleichung auf dem ganzen Raum. In diesem Sinne weist das Landweberverfahren hier bemerkenswerte ähnlichkeiten zu Time Reversal auf.

Ein zweites Ziel ist die Verbesserung der Bildqualität der Rekonstruktion durch nicht-äquidistante Detektoranordnung. Für in der Ebene angeordnete Detektoren und konstante Schallgeschwindigkeit existiert eine exakte Rekonstruktionsformel, die im Frequenzbereich formuliert ist. Der Schlüssel zu einer brauchbaren Umsetzung dieser Formel liegt in der effizienten Auswertung der verwendeten Fouriertransformationen an nicht-äquidstanten Punkten.

Die verwendete, nicht-uniforme schnelle Fouriertransformation ist für dieses Problem aus theoretischer Sicht bestens geeignet, da sie effizient mit nicht-äquidistanten Gitterpunkten sowohl im Definitions- als auch im Wertebereich verfährt. In praktischen Anwendungen (mit synthetischen sowie mit experimentellen Daten) wird dargelegt, dass diese besondere Interpolationsmethode die übliche Polynominterpolation in Bezug auf Genauigkeit und Komplexität übertrifft.

Ein abschließendes Beispiel behandelt photoakustische Bildgebung als zugrundeliegendes Verfahren für elastographische Bildgebung. Eine Folge von Photoakustik-Bildern zeigt die mechanische Deformation eines abgebildeten Objekts über die Zeit. In einem ersten Schritt besteht Elastographie darin, das der Deformation zugrundeliegende Vektorfeld

zu bestimmen. Photoakustik wird üblicherweise als nicht ideal geeignet für die elastographische Anwendung angesehen, weil ihre hochauflösenden, kontrastreichen Bilder über kein *Specklemuster* verfügen, wie sie zB. für Ultraschallbilder charakteristisch sind.

Im Gegensatz zum Standardansatz untersuchen wir die Verwendung von frequenzbandbeschränkten Daten zur Rekonstruktion, Wir zeigen, dass solche Daten zu zusätzlicher Textur im rekonstruierten Bild führen. Wir zeigen außerdem, dass die Band-Limitierung als Regularisierung im Rekonstruktionsprozess dient. Experimentell zeigen wir, dass durch solcherart erhaltene, specklebehaftete Bilder die Deformation verlässlicher rekonstruiert werden kann als mit den originalen oder konventionell geglätteten Daten.

C

Curriculum Vitae

Current Position

- 6.2011-12.2015 PhD student in Mathematics. Computational Science Center, University of Vienna.
  - Advisor: Otmar Scherzer.
  - 01.2015-12.2015 Freier Dienstnehmer at the Computational Science Center, University of Vienna.
  - 09.2014-12.2014 Projektmitarbeiter in the FWF NFN 107, Photoacoustic Imaging in Biology and Medicine.
  - 09.2013-08.2014 University assistant (pre-doc), at the Faculty for Mathematics, University of Vienna.
  - 06.2010-08.2013 Projektmitarbeiter in the FWF NFN 107, Photoacoustic Imaging in Biology and Medicine.

Education

- M.Sc. Mathematics, University of Vienna, 10.2000-10.2010.
  - Thesis: Charakterisierung Pfaffscher Graphen mittels verbotener Teilgraphen.
  - Advisor: Ilse Fischer, Faculty for Mathematics, University of Vienna.

Publications

Journal Papers

- T. Glatz, O. Scherzer, T. Widlak. **Texture Generation for Photoacoustic Elastography.** In *Journal of Mathematical Imaging and Vision* 52(3), 2015

Preprints

- Z. Belhachmi, T. Glatz, O. Scherzer. **Photoacoustic Tomography with Spatially Varying Compressibility and Density.** Submitted to *Journal of Inverse and Ill-posed Problems*. arXiv:1512.07411.
- Z. Belhachmi, T. Glatz, O. Scherzer. **A direct method for Photoacoustic Imaging with Inhomogeneous Sound Speed.** Accepted for publication in *Inverse Problems*. arXiv:1507.01741.
- J. Schmid, T. Glatz, B. Zabihian, M. Liu, W. Drexler, O. Scherzer. **Non-Equispaced Grid-Sampling in Photoacoustics with a Non-Uniform FFT.** Accepted for publication in *Journal of Biomedical Optics*. arXiv:1510.01078.

Conference Proceedings

- J. Schmid, T. Widlak, B. Zabihian, T. Glatz, M. Liu, W. Drexler, O. Scherzer. **Texture Generation in Compressional Photoacoustic Elastography.** In *Proc. SPIE 9323, Photons Plus Ultrasound: Imaging and Sensing*, 93232S, 2015.

Talks

- Z. Belhachmi, T. Glatz, O. Scherzer. **A Gradient Descent Method for Photoacoustic Imaging in Sound-Heterogeneous Media.** At *The 18th European Conference on Mathematics for Industry* , Taormina, Italy, 2014.
- Z. Belhachmi, T. Glatz, O. Scherzer. **A Gradient Descent Method for Photoacoustic Imaging in Sound-Heterogeneous Media.** At *16th International Conference on Inverse Problems in Engineering*, Krakow, Poland, 2014.
- T. Glatz, O. Scherzer. **The Acoustic Inverse Source Problem and Photoacoustic Imaging.** At *International Workshop Vienna 2012: Innovative techniques in Hybrid and Photoacoustic Imaging*, Vienna, Austria, 2012.

Languages

- German: Mother tongue.
- English: Business fluent.
- French: Intermediate.

Teaching Experience

- Exercises to "Einfuehrung in das Mathematische Arbeiten", Winter term 2013/2014, University of Vienna.
- Exercises to "Analysis 1", Summer term 2014, University of Vienna.

Other Skills

- Programming: MATLAB.
- Other scientific software: LaTeX, Mathematica.

Bibliography

[Abb+11] T. Abboud, P. Joly, J. Rodriguez, and I. Terrasse. "Coupling discontinuous Galerkin methods and retarded potentials for transient wave propagation on unbounded domains". *J. Comput. Phys.* 230.15 (2011), p. 58775907.

[ABK96] M. Agranovsky, C. Berenstein, and P. Kuchment. "Approximation by spherical waves in L^p-spaces". *J. Geom. Anal.* 6.3 (1996), pp. 365–383.

[Ada75] R. A. Adams. *Sobolev Spaces*. New York: Academic Press, 1975.

[AF03] R. A. Adams and Fournier J. J. F. *Sobolev Spaces*. 2nd ed. Pure and Applied Mathematics. Amsterdam: Elsevier, 2003.

[Aig+11] F. Aigner, L. Pallwein, M. Schocke, A. Lebovici, D. Junker, G. Schäfer, F. Pedross, W. Horninger, W. Jaschke, E. J. Hallpern, and F. Frauscher. "Comparison of real-time sonoelastography with T2-weighted endorectal magnetic resonance imaging for prostate cancer detection". *J. Ultrasound Med.* 30 (5 2011), pp. 643–649.

[AK07] M. Agranovsky and P. Kuchment. "Uniqueness of reconstruction and an inversion procedure for thermoacoustic and photoacoustic tomography with variable sound speed". *Inverse Probl.* 23.5 (2007), pp. 2089–2102.

[Ana+08] M. A. Anastasio, K. Wang, J. Zhang, G. A. Kruger, D. Reinecke, and R. A. Kruger. "Improving limited-view reconstruction in photoacoustic tomography by incorporating a priori boundary information". In: *Proc. SPIE*. Vol. 6856. 2008, 68561B–68561B–6.

[AS12] S. Arridge and O Scherzer. "Imaging from coupled physics". *Inverse Probl.* 28.8 (2012), p. 080201.

[Aub82] T. Aubin. *Nonlinear analysis on manifolds, Monge-Ampère equations*. Vol. 252. Grundlehren der mathematischen Wissenschaften. New York: Springer, 1982. xii+204.

[Bea05] P.C. Beard. "Two-dimensional ultrasound receive array using an angle-tuned Fabry-Perot polymer film sensor for transducer field characterization and transmission ultrasound imaging". *IEEE Trans. Ultrason., Ferroeletr., Freq. Control* 52.6 (June 2005), pp. 1002–1012.

[Bea11] P. Beard. "Biomedical photoacoustic imaging". *Interface Focus* 1 (2011), pp. 602–631.

[Bey95] G. Beylkin. "On the fast Fourier transform of functions with singularities". *Appl. Comput. Harmon. Anal.* 2.4 (1995).

[BGS15a] Z. Belhachmi, T. Glatz, and O. Scherzer. *A Direct Method for Photoacoustic Tomography with Inhomogeneous Sound Speed*. Preprint on ArXiv arXiv:1507.01741. University of Vienna, Austria, 2015.

[BGS15b] Z. Belhachmi, T. Glatz, and O. Scherzer. *Photoacoustic Tomography With Spatially Varying Compressibility and Density*. Preprint on ArXiv arXiv: 1512.07411. University of Vienna, Austria, 2015.

[Bis+10] R. Biswas, P. Patel, D. W. Park, T. J. Cichonski, M. S. Richards, J. M. Rubin, J. Hamilton, and W. F. Weitzel. "Venous elastography: validation of a novel high-resolution ultrasound method for measuring vein compliance using finite element analysis". *Sem. Dial.* 23.1 (2010), pp. 105–109.

[Boh+00] L. N. Bohs, B. J. Geiman, M. E. Anderson, S. C. Gebhart, and G. E. Trahey. "Speckle tracking for multi-dimensional flow estimation". *Ultrasons* 38 (2000), pp. 369–375.

[BPM99] P.C. Beard, F. Perennes, and T.N. Mills. "Transduction mechanisms of the Fabry-Perot polymer film sensing concept for wideband ultrasound detection". *IEEE Trans. Ultrason., Ferroeletr., Freq. Control* 46.6 (Nov. 1999), pp. 1575–1582.

[BS91] G. Bao and W. W. Symes. "A trace theorem for solutions of partial differential equations". *Math. Methods Appl. Sci.* 14.8 (1991), pp. 553–562.

[BS93] G. Bao and W. W. Symes. "Trace regularity for a second order hyperbolic equation with non-smooth coefficients". *J. Math. Anal. Appl.* 174 (1993), pp. 370–389.

[BSW05] A. Bruhn, C. Schnoerr, and J. Weickert. "Lucas/Canade Meets Horn/Schunck: Combining Local and Global Optic Flow Methods". *Int. J. Comput. Vision* 61.3 (2005), pp. 211–231.

[Bur+05] P. Burgholzer, C. Hofer, G. Paltauf, M. Haltmeier, and O. Scherzer. "Thermoacoustic tomography with integrating area and line detectors". *IEEE Trans. Ultrason., Ferroeletr., Freq. Control* 52.9 (Sept. 2005), pp. 1577–1583.

[CAB07] B. T. Cox, S. R. Arridge, and P. C. Beard. "Photoacoustic tomography with a limited-aperture planar sensor and a reverberant cavity". *Inverse Probl.* 23.6 (2007), S95–S112.

[CB07] B.T. Cox and P.C. Beard. "The frequency-dependent directivity of a planar fabry-perot polymer film ultrasound sensor". *IEEE Trans. Ultrason., Ferroeletr., Freq. Control* 54.2 (2007), pp. 394–404.

[CK92] D. Colton and R. Kress. *Inverse acoustic and electromagnetic scattering theory*. Vol. 93. Applied Mathematical Sciences. Berlin: Springer-Verlag, 1992. x+305.

[Coc03] B. Cockburn. "Discontinuous Galerkin methods". *ZAMM Z. Angew. Math. Mech.* 83.11 (2003), pp. 731–754.

[Coh+01] G. Cohen, P. Joly, J. E. Roberts, and N. Tordjman. "Higher order triangular finite elements with mass lumping for the wave equation". *SIAM J. Numer. Anal.* 38.6 (2001), pp. 2047–2078.

[Dan+12] W. Dan, C. Tao, X.-J. Liu, and X.-D. Wang. "Influence of limited-view scanning on depth imaging of photoacoustic tomography". *Chinese Physics B* 21.1 (2012), p. 014301.

[DGK14] Y. Dong, T. Görner, and S. Kunis. "An algorithm for total variation regularized photoacoustic imaging". *Adv. Comput. Math.* 41.2 (2014), pp. 423–438.

[Doy12] M. M. Doyley. "Model-based elastography: a survey of approaches to the inverse elasticity problem". *Phys. Med. Biol.* 57 (2012), R35–R73.

[DR93] A. Dutt and V. Rokhlin. "Fast Fourier transforms for nonequispaced data". *SIAM J. Sci. Comput.* 14.6 (1993), pp. 1368–1393.

[Dul+98] P. Dular, C. Geuzaine, F. Henrotte, and W. Legros. "A general environment for the treatment of discrete problems and its application to the finite element method". *IEEE Trans. Magn.* 34.5 (1998), pp. 3395–3398.

[EHN96] H. W. Engl, M. Hanke, and A. Neubauer. *Regularization of inverse problems*. Mathematics and its Applications 375. Dordrecht: Kluwer Academic Publishers Group, 1996. viii+321.

[Eme+04] S. Y. Emelianov, S. R. Aglyamov, J. Shah, S Sethuraman, W. G. Scott, R. Schmitt, M. Motamedi, A. Karpiouk, and A. Oraevsky. "Combined ultrasound, optoacoustic and elasticity imaging". *Proc. SPIE* 5320 (2004), pp. 101–12.

[ESS12] P. Elbau, O. Scherzer, and R. Schulze. "Reconstruction formulas for photoacoustic sectional imaging". *Inverse Probl.* 28.4 (2012). Funded by the Austrian Science Fund (FWF) within the FSP S105 - "Photoacoustic Imaging", p. 045004.

[Eva10] L. C. Evans. *Partial Differential Equations*. Second. Vol. 19. Graduate Studies in Mathematics. Providence, RI: American Mathematical Society, 2010.

[Eva98] L. C. Evans. *Partial Differential Equations*. Vol. 19. Graduate Studies in Mathematics. Providence, RI: American Mathematical Society, 1998.

[Faw85] J. A. Fawcett. "Inversion of n-dimensional spherical averages". *SIAM J. Appl. Math.* 45.2 (1985), pp. 336–341.

[FHR07] D. Finch, M. Haltmeier, and Rakesh. "Inversion of spherical means and the wave equation in even dimensions". *SIAM J. Appl. Math.* 68.2 (2007), pp. 392–412.

[Fin92] M. Fink. "Time reversal of ultrasonic fields. I. Basic principles". *IEEE Trans. Ultrason., Ferroeletr., Freq. Control* 39.5 (1992), pp. 555–566.

[FM14] S. Falletta and G. Monegato. “An exact non reflecting boundary condition for 2D time-dependent wave equation problems”. *Wave Motion* 51 (2014), pp. 168–192.

[FMS12] S. Falletta, G. Monegato, and L. Scuderi. “A space-time BIE method for nonhomogeneous exterior wave equation problems. The Dirichlet case”. *IMA J. Numer. Anal.* 32.1 (Jan. 2012).

[Fou03] K. Fourmont. “Non-equispaced fast Fourier transforms with applications to tomography”. *J. Fourier Anal. Appl.* 9.5 (2003), pp. 431–450.

[FPR04] D. Finch, S. Patch, and Rakesh. “Determining a function from its mean values over a family of spheres”. *SIAM J. Math. Anal.* 35.5 (2004), pp. 1213–1240.

[FQ15] J Frikel and E. T. Quinto. “Artifacts in Incomplete Data Tomography with Applications to Photoacoustic Tomography and Sonar”. *SIAM J. Appl. Math.* 75.2 (2015), pp. 703–725.

[FR05] D. Finch and Rakesh. “Trace identities for solutions of the wave equation with initial data supported in a ball”. *Math. Methods Appl. Sci.* 28 (2005), pp. 1897–1917.

[Fri75] F. G. Friedlander. *The wave equation on a curved space-time*. Cambridge, UK: Cambridge University Press, 1975.

[Fu+11] Y. B. Fu, C. K. Chui, C. L. Teo, and E. Kobayashi. “Motion tracking and strain map computation from quasi-static magnetic resonance elastography”. In: *Medical Image Computing and Computer-Assisted Intervention MICCAI 2011*. Ed. by B. Fichtinger, A. Martel, and T. Peters. Vol. 6891. Lecture Notes in Computer Science. Springer, 2011, pp. 428–435.

[GR09] C. Geuzaine and J.-F. Remacle. “Gmsh: a three-dimensional finite element mesh generator with built-in pre- and post-processing facilities”. *Numer. Meth. in Engineering* 79.11 (2009), pp. 1309–1331.

[Gr07] H. Grün, C. Hofer, M. Haltmeier, G. Paltauf, and P. Burgholzer. “Thermoacoustic imaging using time reversal”. In: *Proceedings of the International Congress on Ultrasonics*. paper ID 1542. Vienna, Austria, 2007, pp. 1–4.

[Gro84] C. W. Groetsch. *The Theory of Tikhonov Regularization for Fredholm Equations of the First Kind*. Boston: Pitman, 1984.

[Grü+07] H. Grün, G. Paltauf, M. Haltmeier, and P. Burgholzer. “Photoacoustic tomography using a fiber based Fabry-Perot interferometer as an integrating line detector and image reconstruction by model-based time reversal method”. In: *Novel Optical Instrumentation for Biomedical Applications III*. Ed. by C. D. Depeursinge. Vol. 6631. Proceedings of SPIE. Munich, Germany: SPIE, 2007, p. 663107.

[GSW14] T. Glatz, O. Scherzer, and T. Widlak. *Texture Generation for Photoacoustic Elastography*. Preprint on ArXiv arXiv:1407.6982. Funded by the Austrian Science Fund (FWF) within the FSP S105 - "Photoacoustic Imaging". University of Vienna, Austria, 2014.

[GSW15] T. Glatz, O. Scherzer, and T. Widlak. "Texture Generation for Photoacoustic Elastography". *J. Math. Imaging Vision* 52.3 (2015). Funded by the Austrian Science Fund (FWF) within the FSP S105 - "Photoacoustic Imaging". Funded by the Austrian Science Fund (FWF) within the FSP P26687 - "Interdisciplinary Coupled Physic Imaging", pp. 369–384.

[GYL85] F. C. A. Groen, I. T. Young, and G. Ligthart. "A comparison of different focus functions for use in autofocus algorithms". *Cytometry* 6.2 (1985), pp. 81–91.

[HÖ3] L. Hörmander. *The Analysis of Linear Partial Differential Operators I*. 2nd ed. New York: Springer Verlag, 2003.

[HÖ2] L. Hörmander. "A uniqueness theorem for second order hyperbolic differential equations". *Comm. Partial Differential Equations* 17 (1992), pp. 699–714.

[Hal11] M. Haltmeier. "A mollification approach for inverting the spherical mean Radon transform". *SIAM J. Appl. Math.* 71.5 (2011), pp. 1637–1652.

[Han95] M. Hanke. *Conjugate Gradient Type Methods for Ill-Posed Problems*. Vol. 327. Pitman Research Notes in Mathematics Series. Harlow: Longman Scientific & Technical, 1995.

[HBH04] C. R. Hill, J. C. Bamber, and G.R. Haar. *Phyiscal Principles of Medical Ultrasonics*. 2nd. Wiley, 2004. 528 pp.

[HD03] T. Ha-Duong. "On retarded potential boundary integral equations and their discretisation". In: *Topics in computational wave propagation: Direct and Inverse Problems*. Lecture notes in computational science and engineering. Berlin-Heidelberg: Springer, 2003, pp. 301–336.

[Hel11] S. Helgason. *Integral Geometry and Radon Transform*. New York, NY: Springer, 2011. xiii+301.

[HH92] V. Hamburger and H. L. Hamilton. "A series of normal stages in the development of the chick embryo". *Dev. Dynam.* 195.4 (1992), pp. 231–272.

[HKN08] Y. Hristova, P. Kuchment, and L. Nguyen. "Reconstruction and time reversal in thermoacoustic tomography in acoustically homogeneous and inhomogeneous media". *Inverse Probl.* 24.5 (2008), p. 055006.

[HLR09] M. Haltmeier, A. Leitão, and E. Resmerita. "On regularization methods of EM-Kaczmarz type". *Inverse Probl.* 25.7 (2009), pp. 075008, 17.

[Hri09] Y. Hristova. "Time reversal in thermoacoustic tomography—an error estimate". *Inverse Probl.* 25.5 (2009), 055008 (14pp).

[HS81] B. K. P. Horn and B. G. Schunck. "Determining optical flow". *Artificial Intelligence* 17 (1981), pp. 185–203.

[HSZ09a] M. Haltmeier, O. Scherzer, and G. Zangerl. "A Reconstruction Algorithm for Photoacoustic Imaging Based on the Nonuniform FFT". *IEEE Trans. Med. Imag.* 28.11 (Nov. 2009), pp. 1727–1735.

[HSZ09b] M. Haltmeier, O. Scherzer, and G. Zangerl. "Influence of detector bandwidth and detector size to the resolution of photoacoustic tomography". In: *Argesim Report no. 35: Proceedings Mathmod 09 Vienna*. Ed. by F. Breitenecker and I. Troch. 2009, pp. 1736–1744.

[Hua+12] C. Huang, L. Nie, R. W. Schoonover, L.V. Wang, and M. A. Anastasio. "Photoacoustic computed tomography correcting for heterogeneity and attenuation". *J. Biomed. Opt.* 17 (2012), p. 061211.

[HZ10] M. Haltmeier and G. Zangerl. "Spatial resolution in photoacoustic tomography: effects of detector size and detector bandwidth". *Inverse Probl.* 26.12 (2010), p. 125002.

[J.+05] Ledesma-Carbayo M. J., J. Kybic, M. Desco, A. Santos, M. Sühling, P. Hunziker, and M. Unser. "Spatio-temporal nonrigid registration for ultrasound cardiac motion estimation". *IEEE Trans. Med. Imag.* 24.9 (2005), pp. 1113–1126.

[Jae+07] M. Jaeger, S. Schüpbach, A. Gertsch, M. Kitz, and M. Frenz. "Fourier reconstruction in optoacoustic imaging using truncated regularized inverse k-space interpolation". *Inverse Probl.* 23 (2007), S51–S63.

[Jat+15] A.P. Jathoul, J. Laufer, O. Ogunlade, B. Treeby, B. Cox, E. Zhang, P. Johnson, A.R. Pizzey, B. Philip, T. Marafioti, M.F. Lythgoe, R.B. Pedley, M.A. Pule, and P. Beard. "Deep in vivo photoacoustic imaging of mammalian tissues using a tyrosinase-based genetic reporter". *Nature Phot.* 9 (2015), pp. 239–246.

[KK08] P. Kuchment and L. Kunyansky. "Mathematics of thermoacoustic tomography". *European J. Appl. Math.* 19 (2008), pp. 191–224.

[KK11] P. Kuchment and L. Kunyansky. "Mathematics of photoacoustic and thermoacoustic tomography". In: *Handbook of Mathematical Methods in Imaging*. Ed. by O. Scherzer. New York: Springer, 2011, pp. 817–867.

[KSB11] R. Kowar, O. Scherzer, and X. Bonnefond. "Causality analysis of frequency-dependent wave attenuation". *Math. Methods Appl. Sci.* 34 (1 2011). Funded by the Austrian Science Fund (FWF) within the FSP S105 - "Photoacoustic Imaging", pp. 108–124.

[Kuc14] P. Kuchment. *The Radon Transform and Medical Imaging*. Philadelphia: Society for Industrial and Applied Mathematics, 2014.

[Kun07] L. A. Kunyansky. "Explicit inversion formulae for the spherical mean Radon transform". *Inverse Probl.* 23.1 (2007), pp. 373–383.

[Kös+01] K.P. Köstli, M. Frenz, H. Bebie, and H.P. Weber. "Temporal backward projection of optoacoustic pressure transients using Fourier transform methods". *Phys. Med. Biol.* 46 (2001), pp. 1863–1872.

[Lec+06] D. Lecompte, A. Smits, S. Bussuyt, H. Sol, H. Vantomme, D. Van Hemelrijck, and A. M. Habraken. "Quality assessment of speckle patterns for digital image correlation". *Opt. Laser Eng.* 44.11 (2006), pp. 1132–1145.

[Ler+88] R. M. Lerner, K. J. Parker, J. Holen, R. Gramiak, and R. C. Waag. "Sono-elasticity: medical elasticity images derived from ultrasound signals in mechanically vibrated targets". *Acoust. Imaging* 16 (1988), pp. 317–327.

[Liu+14] M. Liu, B. Maurer, B. Hermann, B. Zabihian, M. G. Sandrian, A. Unterhuber, B. Baumann, E. Z. Zhang, P. C. Beard, W. J. Weninger, and W. Drexler. "Dual modality optical coherence and whole-body photoacoustic tomography imaging of chick embryos in multiple development stages". *Biomedical Optics Express* 5.9 (2014), pp. 3150–3159.

[LQ00] A. K. Louis and E. T. Quinto. "Local tomographic methods in sonar". In: *Surveys on solution methods for inverse problems*. Vienna: Springer, 2000, pp. 147–154.

[Lub88] C. Lubich. "Convolution quadrature and discretized operational calculus. I." *Numer. Math.* 52 (1988), pp. 129–145.

[LW06] L. Li and L. V. Wang. "Speckle in photoacoustic tomography". *Proc. SPIE* 6095 (2006), 60860Y.

[LW09] C. Li and L. V. Wang. "Photoacoustic tomography and sensing in biomedicine". *Phys. Med. Biol.* 54 (2009), R59–R97.

[Man+01] A. Manduca, T. E. Oliphant, M. A. Dresner, J. L. Mahowald, S. A. Kruse, E. Amromin, J. P. Felmlee, J. F. Greenleaf, and R. L. Ehman. "Magnetic resonance elastography: Non-invasive mapping of tissue elasticity". *Med. Image Anal.* 5 (2001), pp. 237–354.

[MAR10] D. Modgil, M. A. Anastasio, and P. J. Rivière. "Image reconstruction in photoacoustic tomography with variable speed of sound using a higher-order geometrical acoustics approximation". *J. Biomed. Opt.* 15.2 (2010), p. 021308.

[Mod03] J. Modersitzki. *Numerical Methods for Image Registration*. New York: Oxford University Press, 2003.

[Mor84] V. A. Morozov. *Methods for Solving Incorrectly Posed Problems*. New York, Berlin, Heidelberg: Springer, 1984.

[Mut+95] R. Muthupillai, D. J. Lomas, P. J. Rossman, J. F. Greenleaf, A. Manduca, and R. L. Ehman. "Magnetic resonance elastography by direct visualization of propagating acoustic strain waves". *Science* 269 (1995), pp. 1854–1857.

[Nah+13] A. Nahas, M. Bauer, S. Roux, and A. C. Boccara. "3D static elastography at the micrometer scale using Full Field OCT". *Biomed. Opt. Express* 4.10 (2013), pp. 2138–2149.

[Nas76] M.Z. Nashed, ed. *Generalized inverses and applications*. New York: Academic Press [Harcourt Brace Jovanovich Publishers], 1976, pp. xiv+1054.

[Nat86] F. Natterer. *The mathematics of computerized tomography*. Stuttgart: B. G. Teubner, 1986. x+222.

[NL81] S. J. Norton and M. Linzer. "Ultrasonic reflectivity imaging in three dimensions: Exact inverse scattering solutions for plane, cylindrical and spherical apertures". *IEEE Trans. Biomed. Eng.* 28.2 (1981), pp. 202–220.

[Nor80] S. J. Norton. "Reconstruction of a two-dimensional reflecting medium over a circular domain: Exact solution". *J. Acoust. Soc. Amer.* 67.4 (1980), pp. 1266–1273.

[NSP14] R. Nuster, P. Slezak, and G. Paltauf. "Imaging of blood vessels with CCD-camera based three-dimensional photoacoustic tomography". *Proc. SPIE* 8943 (2014), p. 894357.

[Oph+91] J. Ophir, I. Cespedes, H. Ponnekanti, Y. Yazdi, and X. Li. "Elastography: a quantitative method for imaging the elasticity of biological tissues". *Ultrason. Imaging* 13 (1991), pp. 111–134.

[Pal+09] G. Paltauf, R. Nuster, M. Haltmeier, and P. Burgholzer. "Photoacoustic Tomography with Integrating Area and Line Detectors". In: *Photoacoustic Imaging and Spectroscopy*. Ed. by L. V. Wang. Optical Science and Engineering. Boca Raton, FL: CRC Press, 2009, pp. 251–263.

[Pal04] V. P. Palamodov. *Reconstructive Integral Geometry*. Vol. 98. Monographs in Mathematics. Basel: Birkhäuser Verlag, 2004.

[Pan+14] X. Pan, J. Gao, S. Tao, K. Liu, J. Bai, and J. Luo. "A two-step optical flow method for strain estimation in elastography: simulation and phantom study". *Ultrasons* 54 (2014), pp. 990–996.

[PB14] P. R. Prasad and S. Bhattacharya. "Improvements in speckle tracking algorithms for vibrational analysis using optical coherence tomography". *J. Biomed. Opt.* 18.4 (2014), p. 18.

[PDR11] K. J. Parker, M. M. Doyley, and D. J. Rubens. "Imaging the elastic properties of tissue: the 20 year perspective". *Phys. Med. Biol.* 56 (2011), R1–R29.

[PM92] J. L. Prince and E. R. McVeigh. "Motion estimation from tagged MR image sequences". *IEEE Trans. Med. Imag.* 11.2 (1992), pp. 238–249.

[Qia+11] J. Qia, P. Stefanov, G. Uhlmann, and H. Zhao. "An efficient Neumann series-based algorithm for thermoacoustic and photoacoustic tomography with variable sound speed". *SIAM J. Imaging Sciences* 4.3 (2011), pp. 850–883.

[Ram85] A.G. Ramm. "Inversion of the backscattering data and a problem of integral geometry". *Phys. Lett. A* 113 (1985), pp. 172–176.

[RMM05] J. Revell, M. Mirmehdi, and D. McNally. "Computer vision elastography: speckle adaptive motion estimation for elastography using ultrasound sequences". *IEEE Trans. Med. Imag.* 24.6 (2005), pp. 755–766.

[Rob91] L. Robbiano. "Théorème d'unicité adapté au contrôle des solutions des problèmes hyperboliques". *Comm. Partial Differential Equations* 16.4–5 (1991), pp. 789–800.

[SCC07] S. B. Doty S. C. Cowin. *Tissue Mechanics*. Springer-Verlag New York, 2007. xvi+682.

[Sch+09] O. Scherzer, M. Grasmair, H. Grossauer, M. Haltmeier, and F. Lenzen. *Variational methods in imaging*. Applied Mathematical Sciences 167. New York: Springer, 2009.

[Sch+11] R. Schulze, G. Zangerl, M. Holotta, D. Meyer, F. Handle, R. Nuster, G. Paltauf, and O. Scherzer. "On the use of frequency-domain reconstruction algorithms for photoacoustic imaging". *J. Biomed. Opt.* 16.8 (2011). Funded by the Austrian Science Fund (FWF) within the FSP S105 - "Photoacoustic Imaging", p. 086002.

[Sch+15] J. Schmid, T. Glatz, B. Zabihian, M. Liu, W. Drexler, and O. Scherzer. *Non-Equispaced Grid Sampling in Photoacoustics with a Non-Uniform FFT*. Preprint on ArXiv arXiv:1510.01078. University of Vienna, Austria, 2015.

[Sch11] O. Scherzer, ed. *Handbook of Mathematical Methods in Imaging*. New York: Springer, 2011.

[Sch98] J. M. Schmitt. "OCT elastography: imaging microscopic deformation and strain of tissue". *Opt. Express* 3.6 (1998), pp. 199–211.

[Seg77] L. A. Segal. *Mathematics Applied to Continuum Mechanics*. London: MacMillan Publishing, 1977.

[SM15] O. Scherzer and L. Mindrinos. "Inverse Problems". Lecture notes summer term 2015. 2015.

[Sol87] D. C. Solmon. "Asymptotic Formulas for the Dual Radon Transform and Applications". *Math. Z.* 195.3 (1987), pp. 321–343.

[SSY11] C. Sun, B. Standish, and V. X. D. Yang. "Optical coherence elastography, current status and future applications". *J. Biomed. Opt.* 16.4 (2011), p. 043001.

[Ste98] G. Steidl. “A note on fast Fourier transforms for nonequispaced grids”. *Adv. Comput. Math.* 9.3-4 (1998), pp. 337–352.

[SU09] P. Stefanov and G. Uhlmann. “Thermoacoustic tomography with variable sound speed”. *Inverse Probl.* 25.7 (2009), pp. 075011, 16.

[SU11] P. Stefanov and G. Uhlmann. “Thermoacoustic tomography arising in brain imaging”. *Inverse Probl.* 27.4 (2011), pp. 045004, 26.

[Tat95] D. Tataru. “Unique continuation for solutions to pde’s; between Hörmander’s theorem and Holmgren’s theorem”. *Comm. Partial Differential Equations* 20.5-6 (1995), pp. 855–884.

[Tat98] D. Tataru. “On the regularity of boundary traces for the wave equation”. *Ann. Sc. Norm. Super. Pisa Cl. Sci. (4)* 26.1 (1998), pp. 185–206.

[TC10] B. E. Treeby and B. T. Cox. “K-Wave: MATLAB toolbox for the simulation and reconstruction of photoacoustic wace fields”. *J. Biomed. Opt.* 15 (2 2010), p. 021314.

[Tit12] J. Tittelfitz. “Thermoacoustic tomography in elastic media”. *Inverse Probl.* 28.5 (2012), p. 055004.

[TL10] C. Tao and X. Liu. “Reconstruction of high quality photoacoustic tomography with a limited-view scanning”. *Opt. Express* 18.3 (2010), pp. 2760–2766.

[Tre+11] B. E. Treeby, T. K. Varslot, E. Z. Zhang, J. G. Laufer, and P. C. Beard. “Automatic sound speed selection in photoacoustic image reconstruction using an autofocus approach”. *Biomed. Opt. Express* 16.9 (2011), pp. 090501–3.

[Vai75] B. R. Vainberg. “On the short wave asymptotic behaviour of solutions of stationary problems and the asymptotic behaviour as $t \to \infty$ of solutions of non-stationary problems”. *Russ. Math. Surv.* 30.2 (1975), pp. 1–58.

[WA11] K. Wang and M. A. Anastasio. “Photoacoustic and thermoacoustic tomography: image formation principles”. In: *[Sch11]*. Ed. by O. Scherzer. Springer, 2011, pp. 781–817.

[Wan+09] H. J. Wang, C. S. Changchien, C. H. Hung, E. L. Eng, W. C. Tung, K. M. Kee, C. H. Chen, T. H. Hu, C. M. Lee, and S. N. Lu. “FibroScan and ultrasonography in the prediction of hepatic fibrosis in patients with chronic viral hepatitis”. *J. Gastroenterol.* 44 (2009), pp. 439–436.

[Wan+11] K. Wang, E. Y. Sidky, M. A. Anastasio, A. A. Oraevsky, and X. Pan. “Limited data image reconstruction in optoacoustic tomography by constrained total variation minimization”. In: *Photons Plus Ultrasound: Imaging and Sensing 2011*. Ed. by Alexander A. Oraevsky and Lihong V. Wang. SPIE, 2011.

[Wan08] L. V. Wang. “Prospects of photoacoustic tomography”. *Med. Phys.* 35.12 (2008), pp. 5758–5767.

[Wan09] L. V. Wang, ed. *Photoacoustic Imaging and Spectroscopy*. Optical Science and Engineering. Boca Raton: CRC Press, 2009. xii+499.

[Wej+10] S. Wejcinski, A. Farrokh, S. Weber, A. Thomas, T. Fischer, T. Slowinski, W. Schmidt, and F. Degenhardt. "Multicenter study of ultrasound real-time tissue elastography in 779 cases for the assessment of breast lesions: improved diagnostic performance by combining the BI-RADS®-US classification system with sonoelastography". *Ultraschall Med.* 31 (2010), pp. 484–491.

[WM04] C. W. Washington and M. I. Miga. "Modality independent elastography (MIE): a new approach to elasticity imaging". *IEEE Trans. Med. Imag.* 23.9 (2004), pp. 1117–1128.

[Woo+06] D. A. Woodrum, A. J. Romano, A. Lerman, U. H. Pandya, D. Brosh, P. J. Rossman, L. O. Lerman, and R. L. Ehman. "Vascular wall elasticity measurement by magnetic resonance imaging". *Magn. Reson. Med.* 56 (2006), pp. 593–600.

[XFW02] Y. Xu, D. Feng, and L. V. Wang. "Exact Frequency-Domain Reconstrcution for Thermoacoustic Tomography — I: Planar Geometry". *IEEE Trans. Med. Imag.* 21.7 (2002), pp. 823–828.

[Xia+13] L. Xiang, B. Wang, L. Ji, and H. Jiang. "4-D Photoacoustic Tomography". *Sci. Rep.* 3 (2013).

[Xu+04] Y. Xu, L. V. Wang, G. Ambartsoumian, and P. Kuchment. "Reconstructions in limited-view thermoacoustic tomography". *Med. Phys.* 31.4 (2004), pp. 724–733.

[XW02] M. Xu and L. V. Wang. "Time-Domain Reconstruction for Thermoacoustic Tomography in a Spherical Geometry". *IEEE Trans. Med. Imag.* 21.7 (2002), pp. 814–822.

[XW03] M. Xu and L. V. Wang. "Analytic explanation of spatial resolution related to bandwidth and detector aperture size in thermoacoustic or photoacoustic reconstruction". *Phys. Rev. E* 67.5 (2003), pp. 0566051–05660515.

[XW05] M. Xu and L. V. Wang. "Universal back-projection algorithm for photoacoustic computed tomography". *Phys. Rev. E* 71.1, 016706 (2005).

[XW06] M. Xu and L. V. Wang. "Photoacoustic imaging in biomedicine". *Rev. Sci. Instruments* 77.4, 041101 (2006).

[XXW02] Y. Xu, M. Xu, and L. V. Wang. "Exact Frequency-Domain Reconstruction for Thermoacoustic Tomography — II: Cylindrical Geometry". *IEEE Trans. Med. Imag.* 21 (2002), pp. 829–833.

[XXW03] M. Xu, Y. Xu, and L. V. Wang. "Time-domain reconstruction algorithms and numerical simulations for thermoacoustic tomography in various geometries". *IEEE Trans. Biomed. Eng.* 50.9 (2003), pp. 1086–1099.

[ZG01] P. Zhou and K. E. Goodson. “Subpixel displacement and deformation gradient measurement using digital image/speckle correlation (DISC)”. *Opt. Eng.* 40.8 (2001), pp. 1613–1620.

[ZLB08] E. Zhang, J. Laufer, and P. Beard. “Backward-mode multiwavelength photoacoustic scanner using a planar Fabry-Perot polymer film ultrasound sensor for high-resolution three-dimensional imaging of biological tissues”. *App. Opt.* 47 (2008), pp. 561–577.

[ZQM10] T. Zakaria, Z. Qin, and R. L. Maurice. “Optical flow-based B-mode elastography: application in the hypertensitive rat carotid”. *IEEE Trans. Med. Imag.* 29.2 (2010), pp. 570–578.

[ZWZ12] Y. Zhang, Y. Wang, and C. Zhang. “Total variation based gradient descent algorithm for sparse-view photoacoustic image reconstruction”. *Ultrasons* 52 (2012), pp. 1046–1055.

[Rad17] J. Radon. “Über die Bestimmung von Funktionen durch ihre Integralwerte längs gewisser Mannigfaltigkeiten”. *Ber. Verh. Kön. Sächs. Ges. Wiss. Leipzig Math. Phys. Kl.* 69 (1917), pp. 262–277.